Joint CT-MRI Image Reconstruction

Xuelin Cui

Dissertation submitted to the Faculty of the
Virginia Polytechnic Institute and State University
in partial fulfillment of the requirements for the degree of

Doctor of Philosophy
in
Electrical Engineering

Lamine Mili, Chair
Amos Abbott
A. A. (Louis) Beex
Guohua Cao
Hengyong Yu

October 12, 2018
Falls Church, Virginia

Keywords: Medical Imaging, Image Reconstruction, Compressed Sensing

Joint CT-MRI Image Reconstruction

Xuelin Cui

(ABSTRACT)

Modern clinical diagnoses and treatments have been increasingly reliant on medical imaging techniques. In return, medical images are required to provide more accurate and detailed information than ever. Aside from the evolution of hardware and software, multimodal imaging techniques offer a promising solution to produce higher quality images by fusing medical images from different modalities. This strategy utilizes more structural and/or functional image information, thereby allowing clinical results to be more comprehensive and better interpreted. Since their inception, multimodal imaging techniques have received a great deal of attention for achieving enhanced imaging performance. In this work, a novel joint reconstruction framework using sparse computed tomography (CT) and magnetic resonance imaging (MRI) data is developed and evaluated. The method proposed in this study is part of the planned joint CT-MRI system which assembles CT and MRI subsystems into a single entity. The CT and MRI images are synchronously acquired and registered from the hybrid CT-MRI platform. However, since their image data are highly undersampled, analytical methods, such as filtered backprojection, are unable to generate images of sufficient quality. To overcome this drawback, we resort to compressed sensing techniques, which employ sparse

priors that result from an application of L_1-norm minimization. To utilize multimodal information, a projection distance is introduced and is tuned to tailor the texture and pattern of final images. Specifically, CT and MRI images are alternately reconstructed using the updated multimodal results that are calculated at the latest step of the iterative optimization algorithm. This method exploits the structural similarities shared by the CT and MRI images to achieve better reconstruction quality. The improved performance of the proposed approach is demonstrated using a pair of undersampled CT-MRI body images and a pair of undersampled CT-MRI head images. These images are tested using joint reconstruction, analytical reconstruction, and independent reconstruction without using multimodal imaging information. Results show that the proposed method improves about 5dB in signal-to-noise ratio (SNR) and nearly 10% in structural similarity measurements compared to independent reconstruction methods. It offers a similar quality as fully sampled analytical reconstruction, yet requires as few as 25 projections for CT and a 30% sampling rate for MRI. It is concluded that structural similarities and correlations residing in images from different modalities are useful to mutually promote the quality of image reconstruction.

Joint CT-MRI Image Reconstruction

Xuelin Cui

(GENERAL AUDIENCE ABSTRACT)

Medical imaging techniques play a central role in modern clinical diagnoses and treatments. Consequently, there is a constant demand to increase the overall quality of medical images. Since their inception, multimodal imaging techniques have received a great deal of attention for achieving enhanced imaging performance. Multimodal imaging techniques can provide more detailed diagnostic information by fusing medical images from different imaging modalities, thereby allowing clinical results to be more comprehensive to improve clinical interpretation.

A new form of multimodal imaging technique, which combines the imaging procedures of computed tomography (CT) and magnetic resonance imaging (MRI), is known as the "omni-tomography." Both computed tomography and magnetic resonance imaging are the most commonly used medical imaging techniques today and their intrinsic properties are complementary. For example, computed tomography performs well for bones whereas the magnetic resonance imaging excels at contrasting soft tissues. Therefore, a multimodal imaging system built upon the fusion of these two modalities can potentially bring much more information to improve clinical diagnoses. However, the planned omni-tomography systems face enormous

challenges, such as the limited ability to perform image reconstruction due to mechanical and hardware restrictions that result in significant undersampling of the raw data.

Image reconstruction is a procedure required by both computed tomography and magnetic resonance imaging to convert raw data into final images. A general condition required to produce a decent quality of an image is that the number of samples of raw data must be sufficient and abundant. Therefore, undersampling on the omni-tomography system can cause significant degradation of the image quality or artifacts after image reconstruction. To overcome this drawback, we resort to compressed sensing techniques, which exploit the sparsity of the medical images, to perform iterative based image reconstruction for both computed tomography and magnetic resonance imaging. The sparsity of the images is found by applying sparse transform such as discrete gradient transform or wavelet transform in the image domain. With the sparsity and undersampled raw data, an iterative algorithm can largely compensate for the data inadequacy problem and it can reconstruct the final images from the undersampled raw data with minimal loss of quality.

In addition, a novel "projection distance" is created to perform a joint reconstruction which further promotes the quality of the reconstructed images. Specifically, the projection distance exploits the structural similarities shared between the image of computed tomography and magnetic resonance imaging such that the insufficiency of raw data caused by undersampling is further accounted for. The improved performance of the proposed approach is demonstrated using a pair of undersampled body images and a pair of undersampled head images, each of which consists of an image of computed tomography and its magnetic resonance imaging counterpart. These images are tested using the proposed joint reconstruction method in this work, the conventional reconstructions such as filtered backprojection and Fourier transform, and reconstruction strategy without using multimodal imaging information (independent reconstruction). The results from this work show that the proposed

method addressed these challenges by significantly improving the image quality from highly undersampled raw data. In particular, it improves about 5dB in signal-to-noise ratio and nearly 10% in structural similarity measurements compared to other methods. It achieves similar image quality by using less than 5% of the X-ray dose for computed tomography and 30% sampling rate for magnetic resonance imaging. It is concluded that, by using compressed sensing techniques and exploiting structural similarities, the planned joint computed tomography and magnetic resonance imaging system can perform imaging outstanding tasks with highly undersampled raw data.

Dedication

This dissertation is dedicated to my mother, Ms. Xiaoyu Huang, who I truly love.

Acknowledgments

My work could not have been achieved without the support from a number of people at Virginia Polytechnic Institute and State University, University of Massachusetts at Lowell, and Rensselaer Polytechnic Institute.

Foremost, I would like to express my gratitude to my academic advisor Dr. Lamine Mili for his advice, supervision and guidance. His truly scientific attitude has made him precise and passionate in his research and has inspired and enriched my growth during my entire Ph.D. program. This work would not have been completed without his guidance and support.

I gratefully thank Dr. Hengyong Yu from the Department of Electrical and Computer Engineering at the University of Massachusetts at Lowell for sharing his valuable thoughts with me. I also thank him for always providing me with unwavering support and encouragement in various ways. I am deeply indebted to him.

I also give many thanks to Dr. Lynn A. Abbott, Dr. Louis Beex, Dr. Guohua Cao from the Department of Electrical and Computer Engineering at Virginia Tech, and Dr. Ge Wang from the Department of Biomedical Engineering at Rensselaer Polytechnic Institute for offering me insightful comments.

Finally, and most importantly, I would like to thank my wife Dr. Yiling Zhang. Her support, encouragement, quiet patience, and unwavering love were undeniably the bedrock upon which

my life has been built upon. I thank my parents, Houyin Cui and Xiaoyu Huang, for their faith in me and allowing me to be as free as I want. I thank my children Richard Yiran Cui and Erik Shuran Cui whose births motivate me to continuously perfect myself in my life. It was under their watchful eyes that I have gained so much drive and an ability to tackle challenges head on.

Contents

List of Figures

List of Tables

Chapter 1

INTRODUCTION

1.1 Background

One of the greatest challenges remaining in the field of modern medical imaging is that the connection between molecular assays and diagnostic imaging is still rather limited. Although revolutionary progress has been witnessed during the past 50 years, modern medical imaging scanners still cannot individually provide a sufficiently broad spectrum of clinical information. For instance, gray-scale images offered by a typical modern X-ray CT scanner can only produce information of linear attenuation coefficients of various tissues.

To bridge the gap between the high demands for more clinical information from the imaging side and the limited capabilities of single modality imaging, multimodal imaging techniques have been developed. The concept of "omni-tomography" was very recently proposed [1, 2], and one of its goals is to design and implement an unprecedented fusion of CT and MRI in a single scanning machine. The hybrid CT-MRI platform will contain hardware and software for both systems as Figure 1.1 shows. Under this setup, the data from CT

and MRI scanners are acquired and registered synchronously ("all in one"), and images are reconstructed simultaneously ("all at once"). The planned omni-tomography also has the potential to further develop into an even more powerful imaging system when PET is integrated [1].

Such a complex system as an omni-tomography scanner faces numerous scientific and technical challenges. One of the core hurdles is its image reconstruction due to the fact that both CT and MRI data are tremendously undersampled on the planned CT-MRI system. Undersampling is known for generating aliasing according to signal processing theory [15], and thus results in a significant degradation of reconstructed imaging data.

This research, as part of the planned omni-tomography project, focuses primarily in the area of image reconstruction. The purpose of this work is to create an effective reconstruction framework for the joint CT-MRI system such that substantial information from the undersampled data can be recovered and the improved image reconstruction can best facilitate clinical decisions.

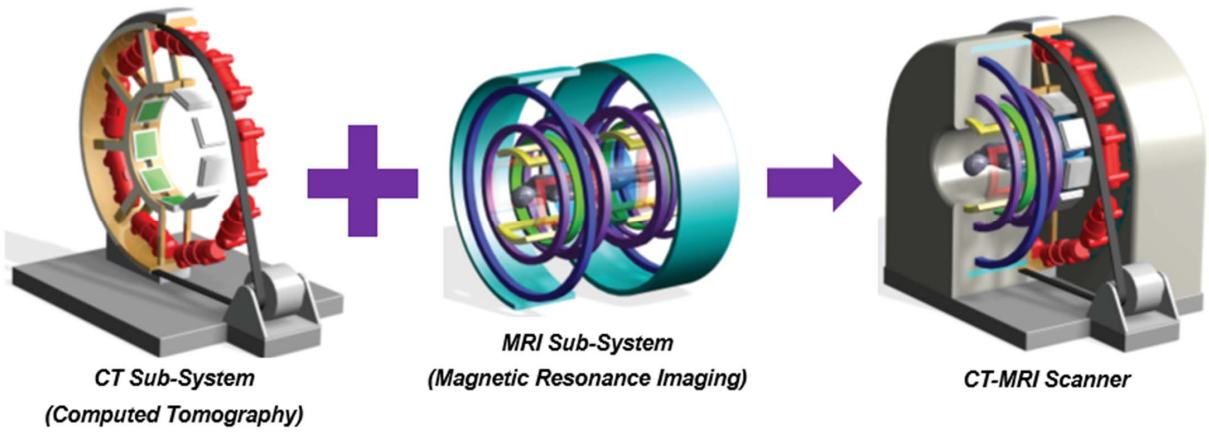

Figure 1.1: The planned omni-tomography scanner combines hardware and software of both CT and MRI systems, which allows it to perform simultaneous CT-MRI imaging [1, 2].

1.2 Multimodal Imaging and Omni-tomography

Multimodal imaging techniques have received a great deal of attention since their inception for achieving enhanced imaging performance. They have been widely hailed as powerful tools to assist the modern clinical decision-making process. It has been shown that multimodal imaging techniques can provide more structural and/or functional information than those performing only a single modality [16, 17]. Since its inception in 1960s [18], a variety of multimodal imaging commercial products have been developed, such as PET-MRI (positron emission tomography and magnetic resonance imaging), SPECT-CT (single positron emission computed tomography and computed tomography), and PET-CT (positron emission tomography and computed tomography). By combining multiple imaging modalities into one single approach, more clinically relevant information can be obtained. Figure 1.2 shows

an example of detection of metastatic prostate cancer using combined PET-CT imaging technique [3]. By using radiotracer, such as ^{18}F-fluorodeoxyglucose (^{18}F-FDG), PET can detect highly metabolic region, such as tumorous tissues, based on the Warburg effect [19]. The left panel shows a PET image where the dark area is highly metabolically active. However, the resolution of the PET image is typically very low. The central panel is the high resolution CT counterpart of the PET image shown in the left panel. Therefore, by merging the left and the central panels, the co-registered multimodal PET-CT image is formulated in the right panel. By offering both functional and structural information, the right panel conveys much more clinical data than either the left or the central panel individually.

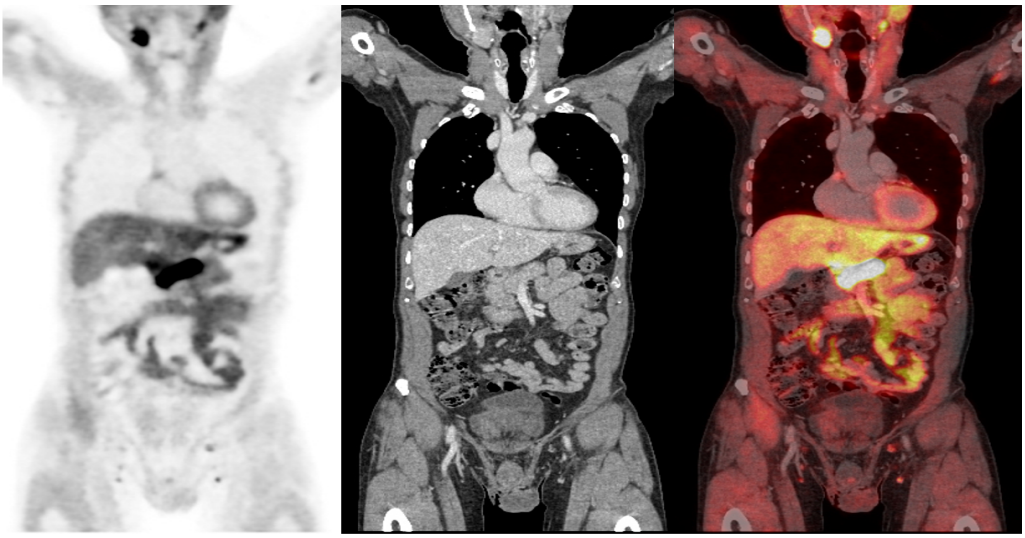

Figure 1.2: An example of PET-CT multiodal imaging. A PET image is displayed in the left panel with a probable tumorous region in darker pixel values. The corresponding CT image is displayed in the central panel. The right panel displays a fused PEI-CT image with the likely tumorous region showing high metabolic activity [3].

Similarly, PET-MRI has been applied in clinical fields including oncology, cardiology, and neurology [20]. Because it is a relatively new technology, active research studies are still ongoing to fully investigate how PET-MRI can potentially be more beneficial. Currently, there are approximately 30 PET-MRI scanners in the United States, compared with over 1600

PET-CT systems [20]. Unlike PET-CT systems, PET-MRI systems generate less ionizing radiation and are much better at generating soft tissue contrast images. Figure 1.3 shows the combined PET-MRI image [21] for initial staging of pancreatic adenocarcinoma. Currently, one of the popular applications of PET-MRI is to evaluate pancreatic lesions due to the superior dynamic range on soft tissue provided by MRI. In addition, PET-MRI can assess for structural abnormalities in the pancreatic region other than diagnosing necrosis, cystic changes, and fibrosis [22]. In fact, PET-MRI demonstrated significantly higher accuracy in the diagnosis of pancreatic cancer than PET-CT [4].

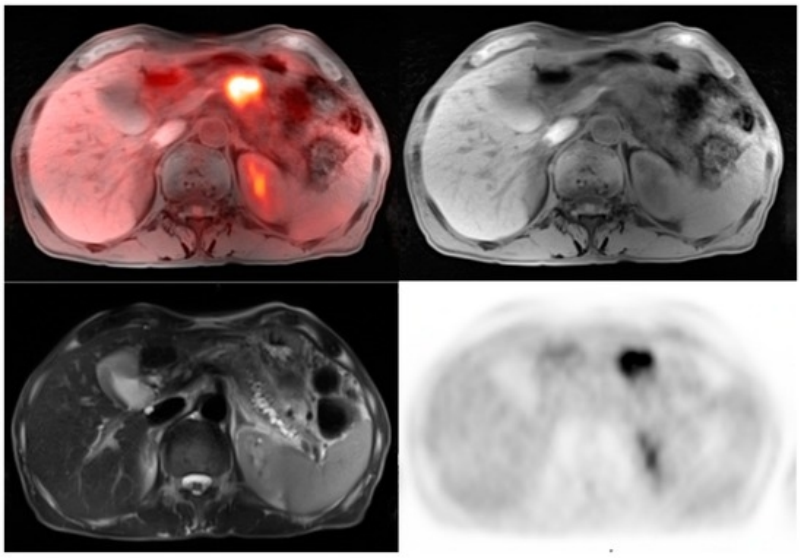

Figure 1.3: The top left panel shows an example of PET-MRI image fusion which indicates a likely tumorous region in the pancreas. The top right panel and bottom left are T_1 and T_2 weighted MRI images showing the structural abnormality in the pancreas region. The bottom right panel shows the original PET image which labels the likely tumorous region with dark pixels [4].

On the other hand, the fusion of CT and MRI has not yet been thoroughly investigated and commercialized. The idea of combining CT and MRI techniques seems natural since both of these systems are the most commonly used imaging modalities today and they are intrinsically complementary to each other in many ways. For example, CT has high contrast

for bones, whereas MRI has excellent dynamic range for soft tissues. Should these two most powerful imaging modalities be combined, clinical decision making processes will be significantly improved.

1.3 Undersampled Image Reconstruction

On the the targeted hybrid CT-MRI platform, both CT and MRI data sets are highly undersampled due to mechanical and electrical limitations. These undersampled data are collected through synchronous acquisition such that online data registration can be achieved [1, 2]. From the image reconstruction perspective, the enabling technology of the joint CT-MRI system is the compressed sensing-based image reconstruction [23, 24]. Conventionally, medical imaging systems employ analytical methods such as filtered backprojection [25] for CT and inverse Fourier transform [26] for MRI to perform image reconstruction. However, to have decent image quality, fully sampled data sets are required. For example, a typical commercial 64-slice CT scanner normally has about 1000×64 detector channels, and it collects approximately 1000 projections per rotation. Therefore, the sampling density is extremely high such that the Nyquist sampling rate is guaranteed. Initiated about a decade ago, compressed sensing techniques have undergone rapid growth in recent years. For instance, Lustig *et al.* [27, 28] showed that compressed sensing can be utilized to reconstruct sparse medical images from undersampled measurements. Their work makes use of the compressed sensing theory developed by Candes, Tao, and Donoho, who proved that by utilizing the prior knowledge of sparse representation of the original signal, the signal itself may be recovered with much fewer samples than what is required by the canonical Nyquist-Shannon sampling theorem [15, 29, 30, 31]. Figure 1.4 shows reconstruction of undersampled CT simulation data using a compressed sensing-based interior tomography technique [5]. The figure shows

the fully sampled image on the top left corner. Its interior reconstruction using the conventional filtered backprojection algorithm, which clearly shows strong artifacts, is displayed in the top center panel. Conversely, the compressed sensing-based reconstruction is shown in the bottom middle panel, and it shows almost identical image quality compared to the fully sampled reconstruction.

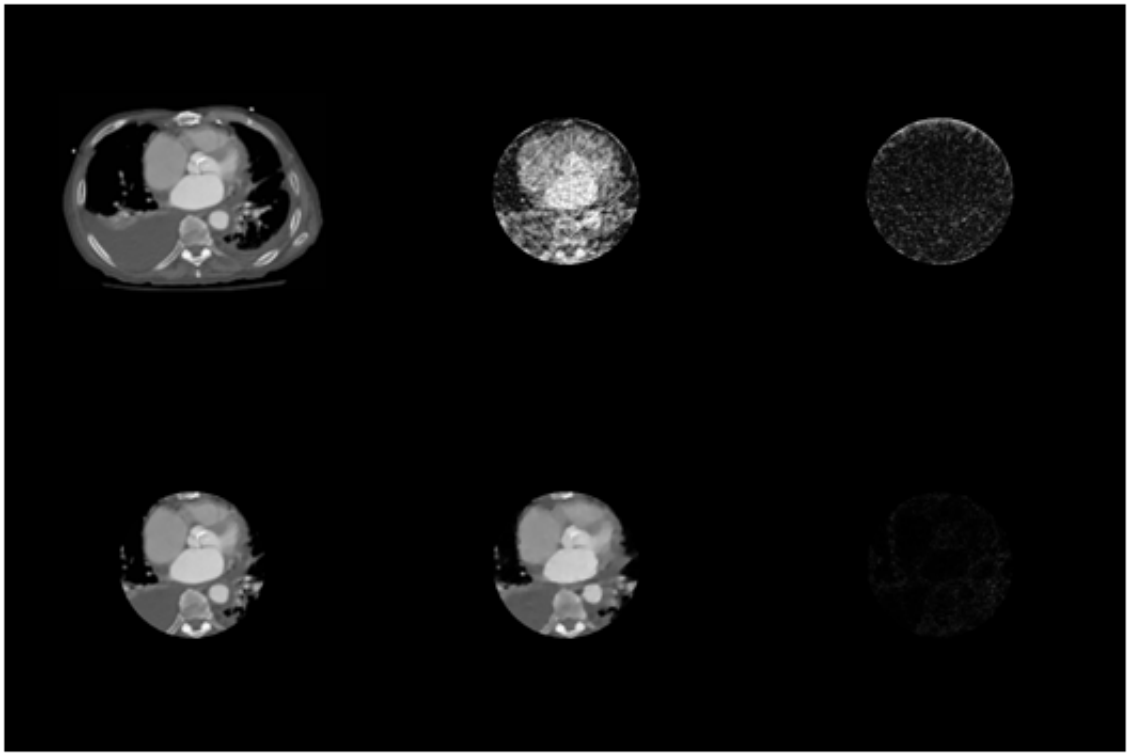

Figure 1.4: CT image of interior tomography shows decent reconstruction quality with a limited number of projections. The top left panel is the original image phantom, the top middle is the reconstruction performed by filtered backprojection, the bottom middle is the image reconstructed using compressed sensing, the bottom left panel is the original ROI as ground truth, the top right is the image difference between filtered backprojection and the ground truth, and the bottom right is the image difference between the compressed sensing and the ground truth [5].

1.4 State of The Art and Contributions

The main contribution of this work is to propose a novel framework which jointly performs image reconstruction on highly undersampled CT and MRI data. In addition, the framework incorporates multimodal information by coupling CT and MRI features, and it provides a feasible numerical method to achieve superior image quality. "Simultaneously" here means that at each iteration, both CT and MRI images are updated, which leads to the fact that at the end of reconstruction, both CT and MRI images are ready for review.

1.4.1 State Of The Art

The idea of performing the joint reconstruction by coupling underlying models that have a common structure emerged in the 1990's. Haber and Oldenbourg found that the joint inversion approach promotes the uniqueness of the solution, and may improve the quality of interpretation [32] . However, the application concentrates on geophysical applications. Rigie [33] employed a "total nuclear variation" to perform joint reconstruction on CT data acquired under different energy levels. However, his work only focuses on CT imaging, and thereby does not utilize any cross-modal information. Ehrhardt [34] investigated the PET-MRI joint reconstruction using a parallel level set. However, PET imaging is remarkably different form CT imaging in terms of its physical realization and mathematical approach. In particular, the spatial resolution of PET images is significantly lower than that of CT or MRI images [35]. Other research on multimodal reconstruction can also be found in [36, 37, 38], but ultimately the CT-MRI joint reconstruction remains a challenging research topic and is highly under-investigated. On the other hand, multimodal coupling has also been explored with many geometric-based [39, 40, 41] and theoretical information based methods [42, 43]. However, all these methods use offline information from other modalities than the CT-MRI

system. Therefore, none of these existing methods can actually fit into the context of the planned omni-tomography system, which requires undersampled CT and MRI images to be reconstructed simultaneously according to the design [1, 2].

In fact, reconstruction strategy using the joint CT-MRI system is far from thoroughly investigated. This is largely due to the fact that the joint CT-MRI system is purely conceptual at this time, and therefore actual CT-MRI data are not yet available. One of the joint CT-MRI reconstruction approaches is proposed by Xi et al. in 2016 in which the joint CT-MRI information is coupled by taking difference in"local image patches" [44]. However, in theory Xi's method should only reply on an impartial data base that builds upon vast number of CT-MRI image pairs, yet his strategy lacks practicality. Another recent joint CT-MRI reconstruction research is proposed by Wang et al. [45], who uses dual dictionary learning techniques to accomplish simultaneous reconstruction. However, it has been pointed out by Li et al. that Wang's methods give poor results [46]. Li's method, on the other hand, does not perform joint reconstruction on CT-MRI data. Instead, it utilizes pre-reconstructed CT image to enhance the MRI reconstruction. In addition, the CT reconstruction is based upon a fully sampled sinogram using a canonical analytical method, which essentially means at least half of the entire data sets are already fully sampled. Therefore, all these methods do not solve the undersampled CT reconstruction problem in Omni-tomography.

1.4.2 Contributions

The challenge of performing joint CT-MRI reconstruction primarily lies in the following three aspects:

1. The lack of actual CT-MRI data requires coupling strategies which intrinsically find the structural and geometrical relation between the CT and the MRI images, such that

the reconstruction quality is enhanced.

2. The undersampled CT and MRI data can easily create strong artifacts in reconstructed images, which must be accounted for.

3. A mathematical model needs to properly describe the joint CT-MRI multimodal imaging system, and it should be feasible to fit into an optimization framework.

4. A robust numerical solution must exist to solve for such a joint CT-MRI system that CT and MRI images are simultaneously obtained with computational accuracy and efficiency.

As discussed in previous sections, the omni-tomography still remains purely theoretical and conceptual for the moment. Therefore, the reconstruction strategy needs to be data driven instead of relying on large number of image samples like [44]. Similarly, the reconstruction strategy should not use offline reconstruction from fully sampled data set for either CT or MRI like [46] since the planned Omni-tomography system does not collect sufficient raw data by design [1, 2].

The modeling of multimodal imaging system in this work is generalized as a multichannel imaging system with each channel being independent of each other [47, 48]. The coupling of joint CT-MRI information is measured by projection distance that enforces the similarity between the CT and MRI images [47, 48]. The multichannel imaging model is then converted to an optimization problem, and solved by a nonlinear conjugate gradient-based algorithm which updates the multimodal imaging information that alternates at each iteration. Ultimately, the major breakthrough of this work comparing existing methods [42, 43, 33, 34, 37, 38, 44, 45, 46] can be listed as follows:

1. This project creates a novel multichannel imaging-based optimization framework to

model joint CT-MRI multimodal imaging problem.

2. This project resorts to compressed sensing techniques with wavelet and total variation prior to handling the highly undersampled CT and MRI data successfully.

3. This project creates a brand new coupling strategy to promote the image quality by utilizing multimodal information between CT and MRI images.

4. This project performs the reconstruction of CT and MRI online and simultaneously with a robust numerical solution with computational accuracy and efficiency.

The methodology proposed in this work is very general. In principle, it can be applied to any problem where images share structural correlations, such as the dual-energy CT imaging systems. For comparison purposes, analytical reconstruction and individually compressed sensing-based reconstructions are also implemented. The latter method does not process any information from the other modality and thereby ignores the similarity and correlated information. Since omni-tomography is currently an active research topic and has not been yet realized, our data are generated by performing simulation on clinical CT and MRI images. Numerical simulations reveal that our joint reconstruction provides a significant improvement in image quality, especially when the structure of the anatomy is more complicated than the piecewise constant phantom.

1.5 Organization of The Dissertation

Chapter 2 offers an overview of how medical imaging systems work, and how image reconstruction is performed. CT and MRI obey fundamentally different physical principles, so their image formation, data acquisition, and image reconstruction share almost no overlap.

Simply stated, CT scan relies on the penetration of X-ray beams through the object being imaged and the signals of these attenuated beams are received by X-ray detectors. The values of attenuation coefficients are converted from photon counts to voltage signals that are related to the density of the tissue. In contrast, the ultimate source of MRI signal is the massive amount of hydrogen atoms in human body. An external magnetic field is imposed along the longitudinal orientation such that all protons are aligned in parallel to the external magnetic field. Radio frequency pulses are then applied to excite the protons off their equilibrium by depositing energy. After these protons are sent into transverse plane, they tend to realign back to their equilibrium when the radio frequency pulses end. During the process when the protons return to their equilibrium, they emit voltage signals that reflect the proton density which is dependent upon the type of the tissue. With regard to reconstruction strategies, CT employs a filtered backprojection type algorithm as its mainstream reconstruction strategy, whereas MRI uses the Fourier transform.

Chapter 3 provides the theory of sampling and compressed sensing-based signal recovery. Conventional theories require sufficient sampling rate to reconstruct an unknown signal so that no aliasing occurs. Aliasing is a phenomenon which leads to different signals being inseparable, thereby generating significant artifacts in medical images. Chapter 3 explains from a physics perspective the conditions under which aliasing occurs in medical imaging. It also demonstrates how compressed sensing-based methods recover signals that are significantly undersampled. The chapter also covers sparsity and L_1-norm minimization, which are the most important concepts in compressed sensing theory.

Chapter 4 describes the proposed joint reconstruction from a theoretical perspective. We employ sparse prior in the optimization framework by applying discrete gradient transform (DGT) to the images. In addition, the concept of projection distance is also introduced to penalize the large divergence between images from different modalities. During the opti-

mization process, CT and MRI images are alternately updated using the latest information from current iteration. The method exploits the structural similarities between the CT and MRI images to achieve better reconstruction quality. The entire framework is accelerated via the parallel processing techniques implemented on a nVidia M5000M graphics processing unit (GPU). This results in a significant decrease of the computational time (from hours to minutes).

Chapter 5 shows the results and analysis of tested clinical image data. The idea is implemented and evaluated on a pair of undersampled abdomen and a pair of undersampled head CT-MRI images. For comparison, the CT and MRI images are also reconstructed by an analytical method, and iterative methods with no exploration of structural similarity, known as independent reconstruction. Results show that the proposed joint reconstruction provides better image quality than either analytical methods or independent reconstruction by revealing more features of the true images.

Finally, Chapter 6 draws conclusions for this work. It also points out the direction of future work which focuses on further improvement for the image reconstruction quality from a joint CT-MRI framework.

Chapter 2

MEDICAL IMAGE RECONSTRUCTION

Medical image reconstruction covers a wide range of topics from basic material science to modern digital signal processing. Medical image reconstruction is the process of forming intelligible images by deciphering the raw data recorded by an imaging system [49]. Medical image reconstruction is a classic example of an inverse problem that seeks to determine the input to a system given the system output.

Modern medical images are generally indirectly measured, which means that raw data are not images. In particular, the CT imaging samples are projection data and the MRI measures k-space data. To reconstruct the images from acquired data, the physical principles have to be thoroughly understood, and mathematical models have to be as precise. The inversion procedure from the raw data to the image requires flawless mathematical derivation based on the accurate model of the imaging physics, which are later processed using digital signal processing.

On the other hand, there have been two major methods up to this point (early 21st century) for image reconstruction: analytical and iterative. Analytical methods for image reconstruction use idealized mathematical models for the imaging system. Canonical examples are the filtered backprojection method [25] for CT imaging and the inverse Fourier transform used in MRI [50]. These methods generally only concentrate on the geometry and sampling properties of the imaging system, but ignore the details of the system physics and measurement noise [49]. Currently, analytical methods are used predominantly in clinical since the physics and noise properties of the imaging system are corrected by calibration procedures which take place prior to reconstruction. Iterative methods, as an alternative, emerged over last two decades. These methods are often statistical and model-based and they solve for solutions with an iterative procedure. Analytical methods and iterative methods coexist in modern medical image reconstruction, and often times they are complimentary depending on the application.

2.1 Medical Imaging Systems

2.1.1 Computed Tomography Imaging

Computed tomography (CT), as a noninvasive imaging modality, uses specially designed X-ray systems to generate cross-sectional or tomographic images of an object. Due to its fast, painless, noninvasive, and accurate imaging process, CT imaging systems are almost universally used for many diagnostic and therapeutic purposes. The fact that CT imaging is X-ray-based makes CT scans eligible for nearly every region of the body for numerous imaging protocols such as diagnostic, treatment planning, interventional, or screening [51].

2.1.2 Physics of Computed Tomography Imaging

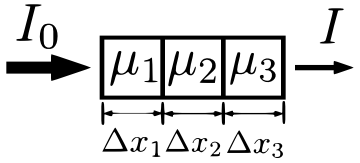

Figure 2.1: Absorption of photon energy according to the Beer-Lambert's law through multiple voxels with different attenuation coefficients.

The data collected by a CT scanner are a number of projections, or sinogram, formed by passing a set of X-ray beams through a 2-D object from different angles. When a X-ray beam travels through an object, its energy becomes attenuated as depicted in Figure 2.1. The absorption of photon energy results in an exponential decay with the distance, which can be formulated with Beer-Lambert's law [52] described in Equation 2.1.

$$ln\Big(\frac{I}{I_0}\Big) = \sum_{n=1}^{N} \mu_n \Delta x_n, \tag{2.1}$$

where I_0 and I are the energy of incident and exiting X-ray beam, μ_n is the linear attenuation coefficients of the nth voxel, and Δx_n is the distance the X-ray beam travels within the nth voxel. The right hand side of Equation 2.1 is sometimes referred to as "ray sum."

A complete sinogram consists of approximately 1000 views collected on an angle set evenly distributed from 0 to 2π. The value of sinogram $p(t, \beta)$ is a function of view angle β and detector position t. The formation of a sinogram follows a Radon transform [53], which can be illustrated by Figure 2.2,

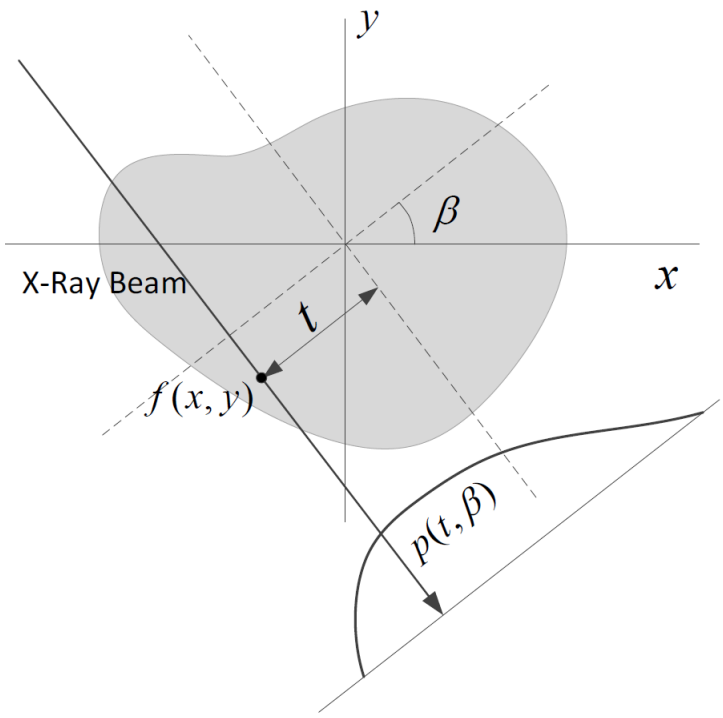

Figure 2.2: Illustration of Radon transform as an X-ray penetrates an object to form a projection signal.

and can be mathematically defined as

$$p(t,\beta) = \int_{-\infty}^{\infty}\int_{-\infty}^{\infty} f(x,y)\delta(xcos\beta + y\sin\beta - t)dxdy, \tag{2.2}$$

where,

$$t = xcos\beta + y\sin\beta. \tag{2.3}$$

In Equation 2.2, $\delta(xcos\beta+y\sin\beta-t)$ is a "2-D line impulse" function that is zero everywhere except on the line defined by $t = xcos\beta + y\sin\beta$. As Equation 2.2 suggests, sinogram is a 2-D function of t and β with its value being $p(t,\beta)$.

2.1.3 Magnetic Resonance Imaging

Magnetic resonance imaging (MRI) is another imaging modality also widely used in clinical fields to image human anatomy as well as physiological processes. Since the formation of MRI signals relies on magnetization generated by excited protons, it is not known to be radioactively hazardous to human subjects. MRI is widely considered one of the most innovative imaging techniques available today, and it serves as a major medical imaging system alongside other modern imaging modalities such as CT, ultrasound, PET, and SPECT.

2.1.4 Physics of Magnetic Resonance Imaging

MRI is based on the physics phenomenon that an external magnetic field and an excitation radio frequency (RF) pulse can trigger the protons in the object to emit a signal. Major components of a MRI system include an external static magnetic field in which the object is placed; a RF transmit coil that excites net magnetization into the transverse plane; magnetic gradients encoding spatial information along different directions; and RF coils that receive MRI signal.

When an external static magnetic field B_0 is applied, protons within the object start precessing around the direction of the magnetic field at a constant frequency. This frequency, f_0, is called the Larmor frequency, and is proportional to the intensity B_0 of external magnetic field. This is described as

$$f_0 = \gamma B_0, \tag{2.4}$$

where γ is a constant named gyromagnetic ratio, and is strictly related to nuclei species. This leads to the fact that protons in different nuclei species, such as H^1, C^13, N^15 or P^31,

precess at different rates even when experiencing the same magnetic field strength. The precessing protons will then be deviated by a RF pulse from its equilibrium state. The net magnetization will be mutated by the RF pulse into the transverse plane perpendicular to the direction of the external static magnetic field. This process is similar to resonance where the amplitude of oscillation is amplified when the driving frequency is approaching the intrinsic frequency of the system itself.

After the net magnetization lies in the transverse plane, another magnetic field, the magnetic gradient, is applied to differentiate spatial information at one location from another. The typical spatial gradients include slice selective, phase, and frequency encoding (readout) to cover spatial information of the object on a 2-D plane. A 3-D acquisition utilizes a slab selective gradient and a second phase encoding gradient. In particular, the space where the MRI signals are recorded is termed "k-space," which is essentially the spatial Fourier transform of the MRI image. For a given data point at (k_x, k_y) in k-space, the signal $S(k_x, k_y)$ is the integral of all the small signals from every location in $f(x, y)$ in image domain at the time when the gradient field is applied, which is described by Equation (2.5).

$$S(k_x, k_y) = \int_{-\infty}^{\infty} \int_{-\infty}^{\infty} f(x, y) e^{-i2\pi(k_x x + k_x y)} \, dx \, dy \tag{2.5}$$

In reality, MRI systems often perform suboptimally from their theoretical operation. Artifacts, caused by various reasons including magnetic and RF field inhomogeneity, non-ideal gradient performance, or other physical/physiological limitations, are commonly found in MRI images. An artifact can be defined as any feature in an image which misrepresents the object in the field of view (FOV). This could be an erroneous bright signal outside the object, or the false absence of a signal. It could also be a reconstructed image with streaks that do not exist in the real object or with a misplaced object signal appearing at a differ-

ent location in the reconstructed than where it actually is. A large group of MRI artifacts appear as "ghost" images, where a faint copy of the object appears in the image, displaced in one direction or another. In general, artifacts are a critical consideration in MRI image reconstruction.

2.2 Medical Image Reconstruction As A Linear Inverse Ill-posed Problem

According to the physics governing image formation of CT imaging and MRI, both their data mappings approximately follow linear transformation. Therefore, by taking into account the existence of some background noise, both CT imaging and MRI can be modeled as

$$\mathbf{y} = \mathbf{A}\mathbf{x} + \sigma. \tag{2.6}$$

In (2.6), $\mathbf{y}$ is the measured data, $\mathbf{A}$ is system matrix, $\mathbf{x}$ is the unknown image, and σ is the system noise. Further explanation about $\mathbf{y}$, $\mathbf{A}$, $\mathbf{x}$, and σ will be addressed in the following sections. The image reconstruction, which is based on the solution of Equation (2.6), can be achieved by regularization-based methods.

2.2.1 Ill-posedness in Medical Imaging

In many cases the process of medical image reconstruction can be formulated as an ill-posed linear inverse problem. The well-posed problem, on the contrary, is defined by the following criteria given by Jacques Hadamard [54]:

1. a solution exists,

2. the solution is unique,

3. the solution's behavior changes continuously with the initial conditions.

Any problem that does not satisfy all of the above criteria at the same time is considered an ill-posed problem. Medical image reconstruction, in particular, often violates the third criterion.

A well known fact is that a major challenge in handling ill-posed problems is that the solution lacks continuous dependence on the data. Since the pioneering work of Jacques Hadamard [54, 55], there has not been much work done in researching ill-posed problems. On the other hand, well-posed problems, such as the heat transfer with boundary conditions, have been investigated for a long period. This is because these problems are regarded as "natural" problems due to their physical processes. The breakthrough for solving ill-posed problems occurred around the 1950s when it is shown that in the case of partial differential equations, it is possible to restore continuous dependence by restricting attention to approximate solutions satisfying a prescribed bound [56, 57]. Apart from that, ill-posed problems have gained attention because they showed that these problems could be potentially interesting in several areas such as medical imaging, geographic sensing, and remote sensing.

As previously mentioned in Equation 2.6, with simplification, the CT forward projection can be modeled as a linear operation. Here $\mathbf{A}$ is the forward projector that maps CT image to sinogram. The mathematics that describe how $\mathbf{A}$ works is a Radon transform [53]. Evaluation of $\mathbf{A}$ is a simple matrix vector multiplication by re-organizing an digital image into a 1-D vector. Thus $\mathbf{x}$ can be reconstructed by multiplication of $\mathbf{y}$ with inverted $\mathbf{A}$. This is a direct inverse method. The linear mapping of an image to its sinogram *via* matrix multiplication is illustrated in Figure 2.3, where the $\mathbf{A}$ is a largely sparse matrix with only

a small portion of its entries being non-zero.

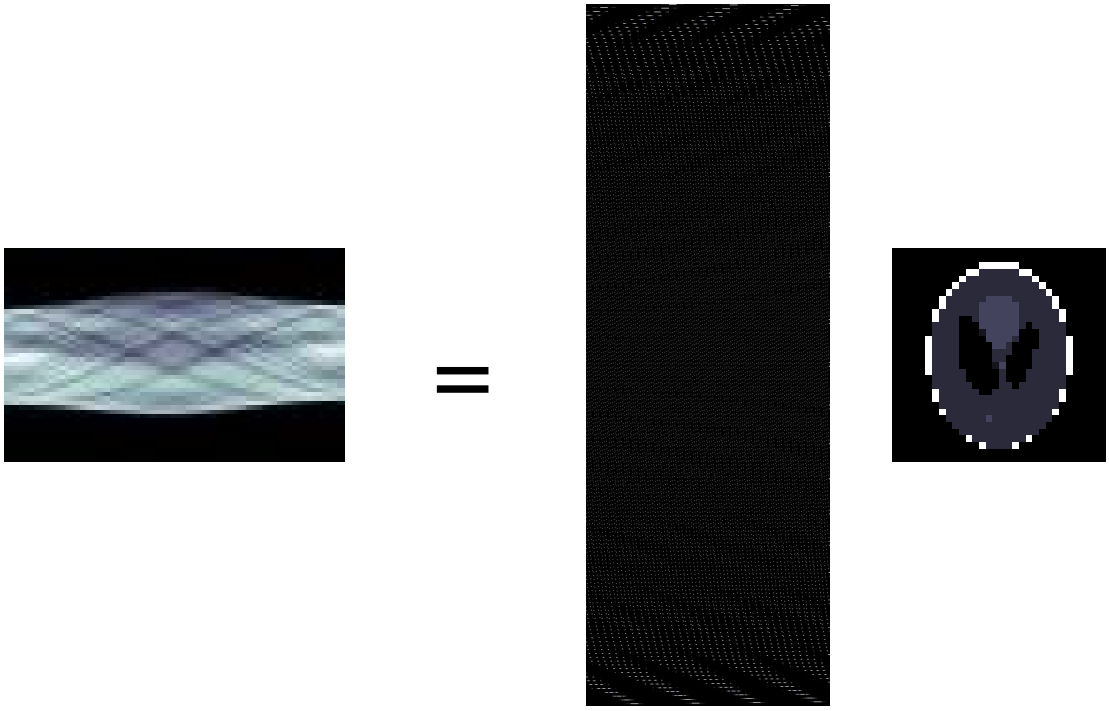

Figure 2.3: The linear mapping of an 32×32 phantom image $\mathbf{x}$ to its sinogram *via* matrix multiplication; The size of the sinogram $\mathbf{y}$ is 8820×1, and the size of of $\mathbf{A}$ is 8820×1024; The actual size of the image is vectorized to 1024×1 during computation. Note that the size of the matrices in the figure is not entirely proportional to the actual size of the $\mathbf{y}$, $\mathbf{A}$ and $\mathbf{x}$.

To demonstrate that medical image reconstruction violates the third criteria of the definition of well-posed problem, a small amount of disturbance is added to sinogram $\mathbf{y}$, and direct inverse is performed to see how well the behavior of the solution changes continuously as the initial conditions change. As is shown in Figure 2.4, when an image (top left panel) is applied with a forward projector *via* matrix multiplication, its sinogram (top right panel) is obtained. This operation is simply $\mathbf{y} = \mathbf{A}\mathbf{x}$. Then a Gaussian noise, whose maximum amplitude is 1% of the maximum amplitude of the signal, is added to the sinogram. This operation essentially generates a noisy signal $\mathbf{y} = \mathbf{A}\mathbf{x} + \sigma$, which is shown in the bottom

right panel of the figure. Note here the magnitude of the noise is very small compared to that of the original signal. Presumably, if reconstructing $\mathbf{x}$ from $\mathbf{y}$ by direct inverse is a well-posed problem, then an additive noise of 1% magnitude on $\mathbf{y}$ should not result in a significant change in $\mathbf{x}$. However, the reconstruction by multiplication of $\mathbf{A^{-1}}$ shown in the bottom left panel loses almost all the information of the original image.

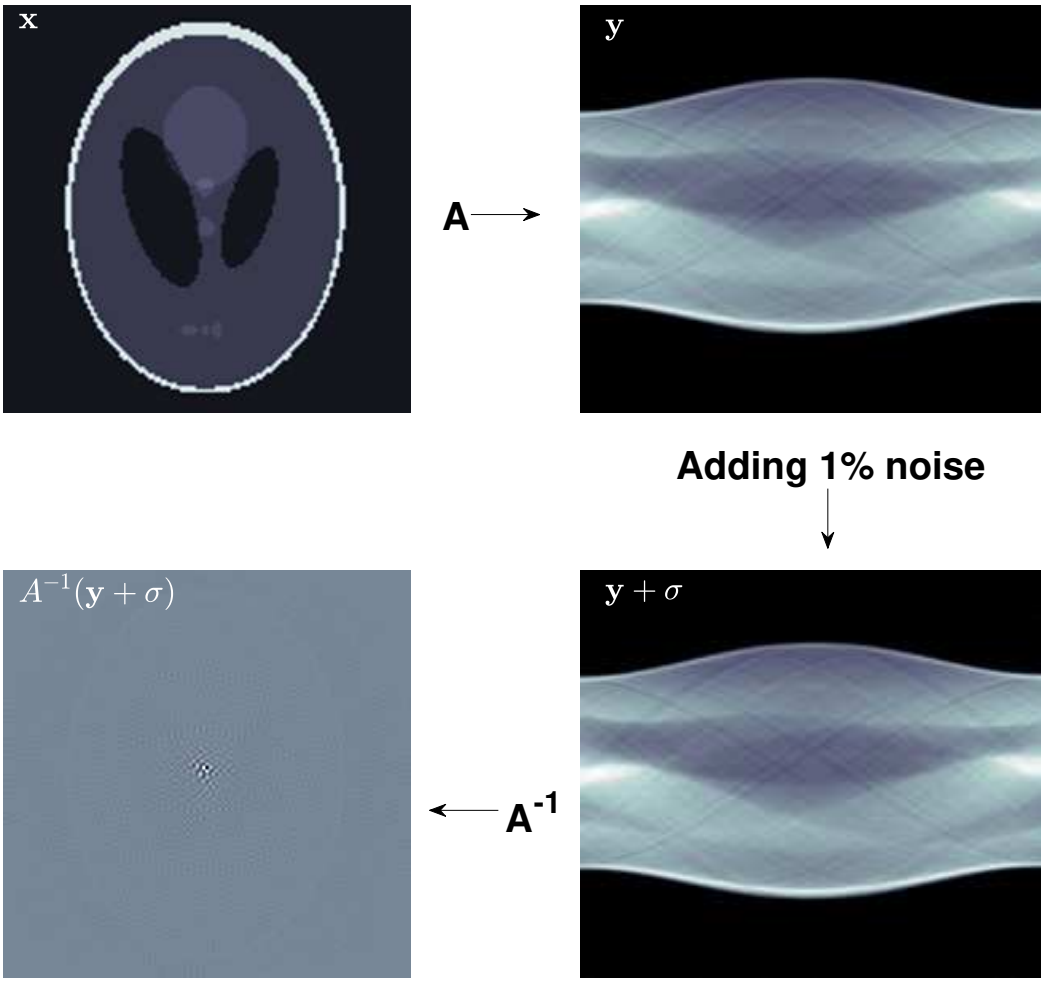

Figure 2.4: Medical image reconstruction as ill-posed problem.

As Figure 2.3 shows, $\mathbf{A}$ is a large matrix with the majority of it entries being values close to 0. Therefore, even though the inverse of $\mathbf{A}$, $\mathbf{A^{-1}}$, does exist, its determinant $|\mathbf{A}|$ is large. Generally, in linear ill-posed problems, $\mathbf{x}$-to-$\mathbf{y}$ mapping through $\mathbf{A}$ is bounded in Hilbert space [58, 59]; $\mathbf{A}$ is injective, but $\mathbf{A^{-1}}$ is not continuous; The measurements $\mathbf{y}$ are not noise-free, and they become $\mathbf{y} + \sigma$ in actuality. In the example of Figure 2.4, dependence between the data and the solution is also illustrated in Figure 2.5. The normalized error in measurement, $\delta\mathbf{y}$, is 10^{-3}, but the normalized error in reconstruction, $\delta\mathbf{x}$, is 90, and the amplification of error is approximately $90,000$. Therefore, as pointed out previously, in linear ill-posed inverse problems, even the smallest amount of noise will corrupt reconstructions.

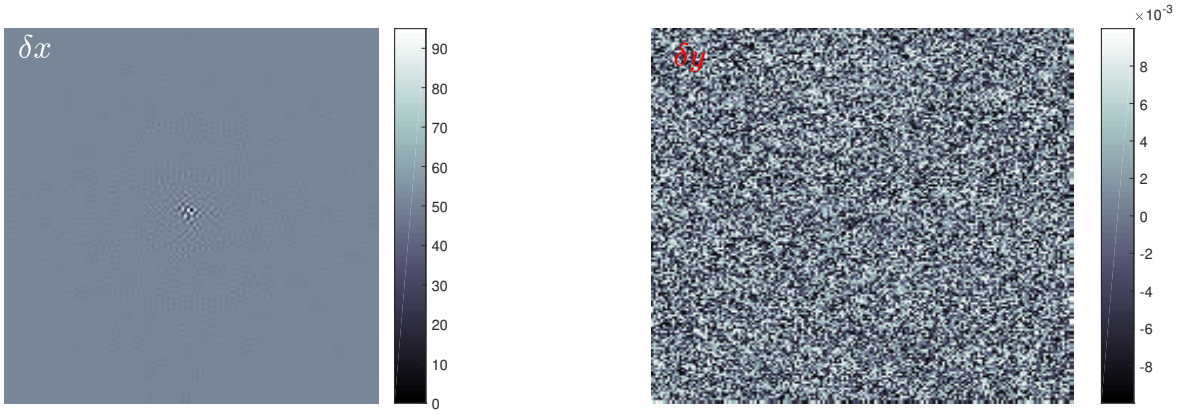

Figure 2.5: Illustration of dependence between the data and the solution in ill-posed linear inverse problem. The amplification of error is approximately $90,000$.

2.2.2 Regularization

In order to control the reconstruction, additional information, known as regularization, is required during the process of solving an ill-posed problem. Simply, regularization is a technique that applies to objective functions in ill-posed optimization problems such that the dependence between the data and the solution is strengthened.

A classical regularization is the Tikhonov regularization [60, 61] developed by the Russian mathematician Andrey Nikolayevich Tikhonov. The basic idea of the Tikhonov regularization is to lower the condition number of a system matrix $\mathbf{A}$ by inserting the second norm of the unknown, and therefore stabilize the system. Note: solving for $\mathbf{y} = \mathbf{A}\mathbf{x}$ is also equivalent to solving

$$\hat{\mathbf{x}} = \arg\min_{\mathbf{x}} \|\mathbf{y} - \mathbf{A}\mathbf{x}\|_2^2. \tag{2.7}$$

Therefore, by adding an additional term $\|\mathbf{\Gamma}\mathbf{x}\|_2^2$, Equation 2.7 becomes

$$\hat{\mathbf{x}} = \arg\min_{\mathbf{x}} \Big(\|\mathbf{y} - \mathbf{A}\mathbf{x}\|_2^2 + \|\mathbf{\Gamma}\mathbf{x}\|_2^2 \Big), \tag{2.8}$$

where $\mathbf{\Gamma}$ is the Tikhonov matrix. In numerous circumstances, the Tikhonov matrix is simply in the form of an identity matrix multiplying a constant $\mathbf{\Gamma} = \alpha\mathbf{I}$. This formulation leads to the fact that $\mathbf{x}$ with larger norm becomes more penalized, therefore the solution with lower energy is more favored. This is also known as L-2 regularization [36]. By adding regularization term, the condition number of the linear system is decreased, hence a direct numerical solution becomes available. Following this idea, a more stable version of $\mathbf{A}^{-1}$ is given by

$$\mathbf{R} = \Big(\mathbf{A}^*\mathbf{A} + \mathbf{\Gamma}^*\mathbf{\Gamma} \Big)^{-\mathbf{1}} \mathbf{A}^*, \tag{2.9}$$

where $*$ is the adjoint, or Hermitian, operator [62].

With $\mathbf{\Gamma} = \sqrt{\alpha}\mathbf{I}$, where $\mathbf{I}$ is an identity matrix, Equation 2.9 becomes

$$\mathbf{R}_\alpha = \Big(\mathbf{A}^*\mathbf{A} + \alpha\mathbf{I} \Big)^{-1} \mathbf{A}^*. \tag{2.10}$$

Therefore, an direct solution $\hat{\mathbf{x}}$, can be obtained by:

$$\begin{aligned}\hat{\mathbf{x}} &= \Big(\mathbf{A}^*\mathbf{A} + \mathbf{\Gamma}^*\mathbf{\Gamma}\Big)^{-1}\mathbf{A}^*\mathbf{y} \\ &= \Big(\mathbf{A}^*\mathbf{A} + (\sqrt{\alpha})^2\mathbf{I}^*\mathbf{I}\Big)^{-1}\mathbf{A}^*\mathbf{y} \\ &= \Big(\mathbf{A}^*\mathbf{A} + \alpha\mathbf{I}\Big)^{-1}\mathbf{A}^*\mathbf{y}.\end{aligned} \tag{2.11}$$

Note that in Equation 2.11, α is a scalar as a tuning parameter, and $\mathbf{I}^*\mathbf{I} = \mathbf{I}$. An example of choosing α is to let $\alpha = \sigma$. Then, if $\sigma \to 0$ (small noise), we have

$$\mathbf{R}_\sigma\Big(\mathbf{y} + \sigma\Big) \xrightarrow{\sigma \to 0} \mathbf{A^{-1}y} \tag{2.12}$$

Theorem 2.12 can be proved by following Minkowski inequality [63]

$$\Big\|\mathbf{R}_\sigma\Big(\mathbf{y} + \sigma\Big) - \mathbf{A^{-1}y}\Big\| \leqslant \Big\|\mathbf{R}_\sigma\Big(\mathbf{y} + \sigma - \mathbf{y}\Big)\Big\| + \left\|\mathbf{R}_\sigma\mathbf{y} - \mathbf{A}^{-1}\mathbf{y}\right\|. \tag{2.13}$$

Note in Inequality 2.13, both $\|\mathbf{R}_\sigma(\mathbf{y} + \sigma - \mathbf{y})\|$ and $\|\mathbf{R}_\sigma\mathbf{y} - \mathbf{A}^{-1}\mathbf{y}\|$ go towards 0 as σ goes towards 0.

A demonstration of applying Tikhonov regularization in an ill-posed reconstruction is shown in Figure 2.6. In this example, Tikhonov regularization is applied to the ill-posed inverse problem shown in Figure 2.4, where the reconstruction resulted in a significant loss of image information. It can be observed that with Tikhonov regularization the reconstruction quality is largely improved. The Tikhonov regularization offers an inexact but continuous reconstruction. It also provides additional information on noise measurement depending on the choice of parameter rules. These features guarantee the convergence of solution in reconstruction processes.

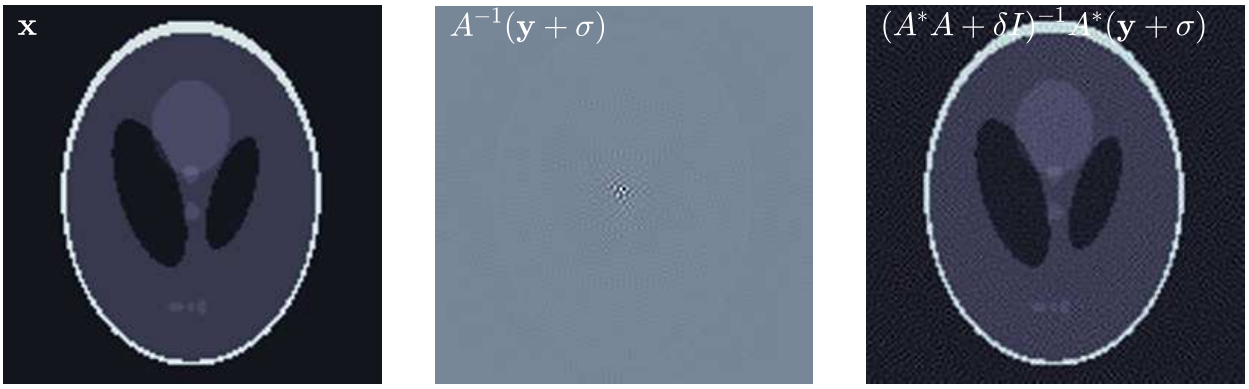

Figure 2.6: The quality of reconstruction of the ill-posed inverse problem shown in Figure 2.4 can be significantly improved by insertion of regularization shown from Equation 2.8 to Equation 2.11. From left panel to right panel: original image; reconstruction by multiplication of $\mathbf{A}^{-1}$; and reconstruction with Tikhonov regularization.

2.3 Analytical Reconstruction

Modern medical image reconstruction can be categorized into two major groups: analytical and iterative. The analytical reconstruction relies on a mathematically close-formed solution to give fast and accurate results. The iterative methods, on the other hand, reconstructs images by iteratively minimizing an objective function which normally is made up of data fidelity and regularization [36]. We will focus on the analytical methods in this section, and the iterative methods will be introduced in Section 2.4.

2.3.1 Fourier-slice Theorem

Fourier-slice theorem is of central importance for medical image reconstruction. It establishes the relation between the 2-D Cartesian-based image domain and sampling in 2-D radial-based Fourier domain. It eventually leads to the filtered backprojection algorithm, which is the

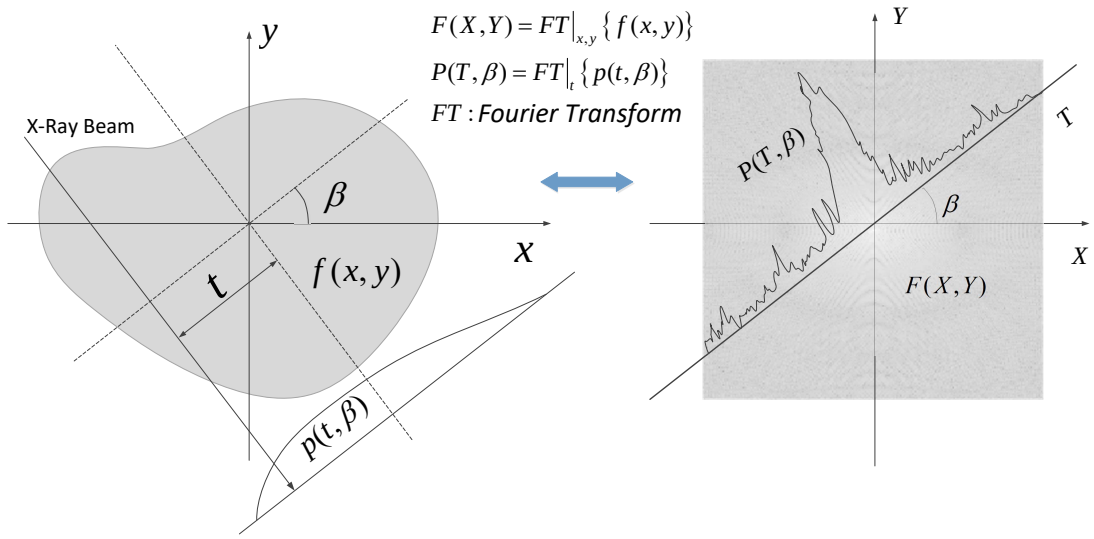

Figure 2.7: Fourier-slice theorem in CT imaging: the 1-D Fourier transform of a projection $p(t,\beta)$ is the 2-D Fourier transform of $f(x,y)$ evaluated at angle β.

core concept in CT image reconstruction as well as MRI image reconstruction [64].

The Fourier-slice theorem is illustrated in Figure 2.7. It states that the 1-D Fourier transform of a projection $p(t,\beta)$ at angle β is the 2-D Fourier transform of $f(x,y)$ evaluated at same angle β. The proof of Fourier Slice theorem is in Equation 2.14.

$$
\begin{aligned}
P(T,\beta) &= FT\Big|_t\Big\{p(t,\beta)\Big\} \\
&= \int_{-\infty}^{\infty}\int_{-\infty}^{\infty}\int_{-\infty}^{\infty} f(x,y)\delta(xcos\beta + y\sin\beta - t)e^{-j2\pi tT}dxdydt \\
&= \int_{-\infty}^{\infty}\delta(xcos\beta + y\sin\beta - t)dt\int_{-\infty}^{\infty}\int_{-\infty}^{\infty} f(x,y)e^{-j2\pi T(xcos\beta + y\sin\beta)}dxdy \\
&= \int_{-\infty}^{\infty}\int_{-\infty}^{\infty} f(x,y)e^{-j2\pi T(xcos\beta + y\sin\beta)}dxdy \\
&= F(X,Y)\Big|_{(X=Tcos\beta, Y=Tsin\beta)} \\
&= F(T,\beta)
\end{aligned}
\tag{2.14}
$$

2.3.2 Filtered backprojection

The reconstruction task of CT imaging is to restore images from the sinogram. This problem can be analytically solved by applying filtered backprojection (FBP)-typed algorithms [25] formulated as

$$f(t,\beta) = \int_0^{\pi} \int_{-\infty}^{\infty} P(T,\beta) \Big| T \Big| e^{j2\pi Tt} dT d\beta, \tag{2.15}$$

where

$$P(T,\beta) = \int_{-\infty}^{\infty} \left(\int_{-\infty}^{\infty} \int_{-\infty}^{\infty} f(t,\beta)\delta(xcos\beta + y\sin\beta - t) \right) e^{-j2\pi tT} dT. \tag{2.16}$$

In Equation 2.15, $\Big|T\Big|$ is the known as the "Ram-Lak filter" [25] with T being spatial frequency usually in the unit of line-pair-per-centimeter (lp/cm). The Ram-Lak filtering is the result of switching coordinate system from Cartesian to polar, and it weighs down the DC (direct current) portion of the sinogram where the signal is significantly over-sampled. Note that the right hand side of the Equation 2.16 is the 1-D Fourier transform of a projection on t at angle β. Equation 2.16 is known as "Fourier-slice theorem" described in section 2.3.1.

An illustration of a CT sinogram, and its reconstructed image is depicted in Figure 2.8

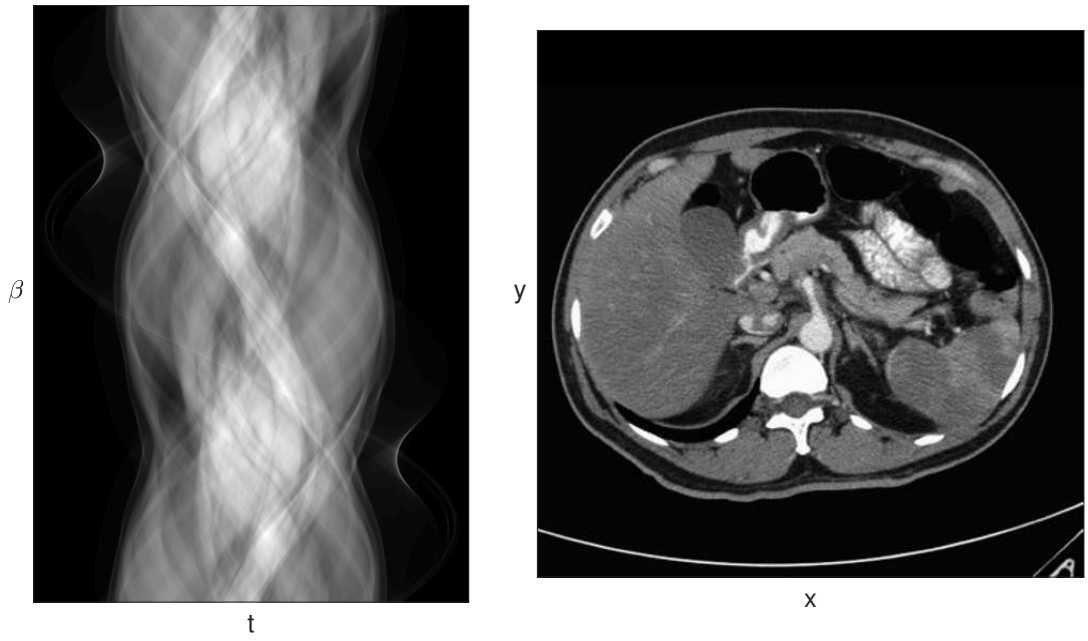

Figure 2.8: The sinogram-reconstruction pair: left) An CT sinogram is a collection of projections from different view angles from 0 (bottom) to 2π (top); right) a reconstructed CT image from the sinogram on the left panel.

2.3.3 Image Reconstruction of Magnetic Resonance Imaging

Similarly, reconstruction MRI consists of analytical methods and iterative methods. We will still focus on analytical methods in this section, and the iterative methods will be further discussed in Section 2.4.

As explained in previous section, the k-space signal is essentially the Fourier transform of the original MRI image. However, there are numerous ways to sample the k-space, which leads to additional operation on k-space data prior to Fourier transform. For instance, sampling with non-Cartesian trajectory on k-space, such as radial or spiral sampling, would require regridding and interpolation to convert the non-Cartesian k-space data to Cartesian format. This is illustrated in Figure 2.9.

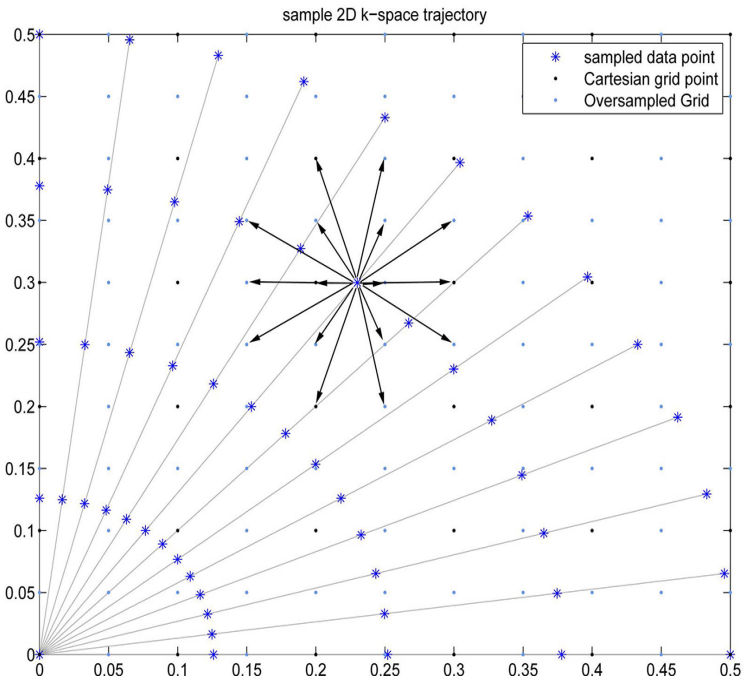

Figure 2.9: Regridding of K-space signal with radial sampling trajectory: non-Cartesian sampling points are converted to Cartesian sampling points using interpolations.

After k-space signal is re-formatted onto a Cartesian grid, inverse 2-D Fourier transform, represented in (2.17), is applied to get the reconstructed images.

$$f(x,y) = \int_{-\infty}^{\infty}\int_{-\infty}^{\infty} S(k_x,k_y)e^{i2\pi(k_x x + k_x y)}\,dk_x\,dk_y \tag{2.17}$$

An illustration of a CT sinogram, and its reconstructed image is depicted in Figure 2.10

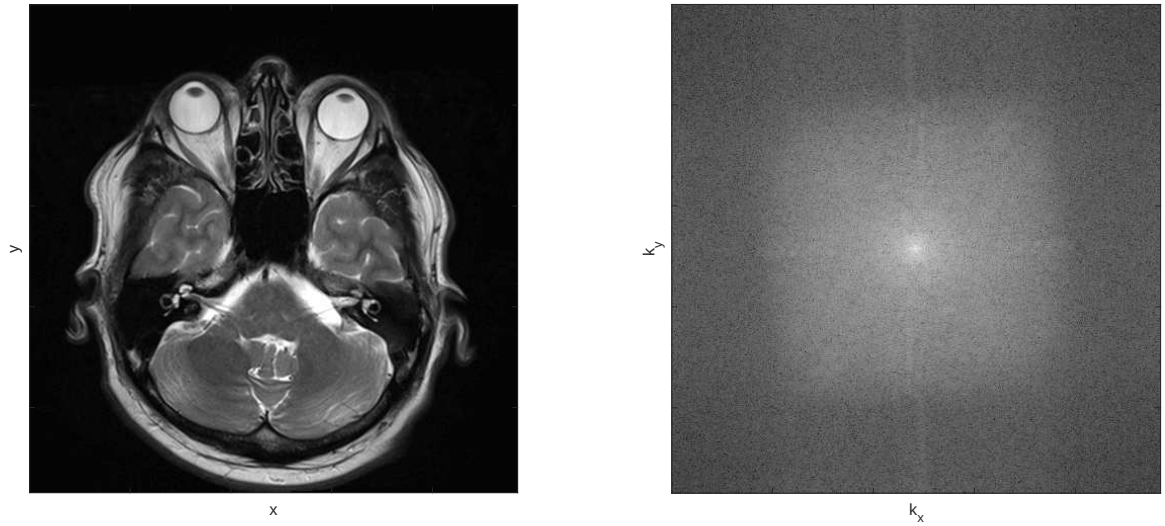

Figure 2.10: The k-space-reconstruction pair: left) An MRI k-space is a collection of MR samples in Fourier domain from different phase and frequency encoding positions; right panels shows a reconstructed MRI image from the k-space on the left panel.

2.4 Iterative Image Reconstruction

Iterative reconstruction is not new, and its application to medical image reconstruction can be traced back to the 1970s [65]. They showed encouraging results in early tomographic reconstruction when the amount of raw data per scan was much less and when the reconstructed image size was relatively small. As fast high-resolution CT was introduced as mainstream in clinical CT scanning, iterative methods were no longer practical as the major reconstruction strategy due to its lengthy computational time.

In recent years, with the tremendous progress of massively-scaled computational capacities and the ongoing efforts towards dose minimization, iterative reconstruction methods have re-emerged as a popular topic. As discussed previously, analytical methods normally require

large amount of the dose to achieve superior image quality. Hence, in many scenarios where dose minimization is of utmost consideration or where instant image reconstruction is not required, iterative reconstruction can show great potential in artifact reduction.

2.4.1 Iterative Methods for Solving Linear Systems

From numerical analysis perspective, for many problems such as large linear equations, it is simply not practical to use direct inverse methods with computational complexity of $O(n^3)$. A typical CT image has 512×512 pixels. Its sinogram depends on the setup of the scanning system, but usually has approximately 1000 channels per row, and approximately 1000 views per revolution. For a 64-slice scanning system, the total size of image pixel is $512 \times 512 \times 64 = 16,777,216$, and the total size of sinogram is $1000 \times 1000 \times 64 = 64,000,000$. Therefore, the size of matrix $\mathbf{A}$ should be $64,000,000 \times 16,777,216 = 1.073741824e + 15$. During the computation, all these numbers are represented either by a 32-bit or 64-bit floating-point numbers, thus the space required to store the matrix $\mathbf{A}$ in the RAM is $64,000,000 \times 16,777,216 \times 32 \times 1.25 \times 10^{-10} \approx 4.3 \times 10^6$ Gigabyte for 32-bit floating-point number computation. This is simply far beyond the computational capacities of most modern computer systems. In addition, even sparse direct methods are also too computationally expensive.

The numerical solution to recover unknown images from such a massive linear system is to apply iterative methods. Iterative methods formulate the problem of solving for unknown images as an optimization problem. This is usually achieved by constructing an cost function which incorporates data fidelity and regularization. The data fidelity restricts the estimated image at each iteration to be as close to the collected data as possible. The regularization can govern other known features of the unknown images such as piecewise constancy. Itera-

tive reconstructions handles the solving process with more flexibility compared to analytical methods which always assumes the solution is unique and only gives "one shot" for reconstruction. Conversely, iterative reconstruction can seek the optimal solution by incorporating details of physics and noise of the system, which in return offers reconstructed images with different details.

More importantly, although analytical methods offer high quality reconstruction, such algorithms require a huge amount of data collection. For example, typical clinical CT scanning systems normally acquire about 1000 views per revolution such that FPB-type algorithms can use sufficient data to perform image reconstruction. In reality, the data are sometimes undersampled, for instance, the omni-tomography as discussed in Chapter 1.2, due to hardware or software restrictions. In this case, iterative methods are the only option.

The principle of iterative methods are described in following steps:

1. Starting with an initial guess such as an empty image (or FBP)

$$\hat{\mathbf{x}}^0 := 0$$

2. Mapping the image to its raw data domain $\hat{\mathbf{y}}^k$ by applying the system matrix $\mathbf{A}$:

$$\hat{\mathbf{y}}^k := \mathbf{A}\hat{\mathbf{x}}^k$$

3. Compare with measured data $\mathbf{y}$, to compute the "error" given by $\hat{\mathbf{x}}^k$ is

$$\mathbf{e}^k := \mathbf{y} - \hat{\mathbf{y}}^k = \mathbf{y} - \mathbf{A}\mathbf{x}^k\,, \quad k \geq 0.$$

4. Update of solution at kth iteration:

$$\hat{\mathbf{x}}^{k+1} := \Psi(\hat{\mathbf{x}}^k), \quad k \geq 0$$

where the function $\Psi(\hat{\mathbf{x}}^k)$ is often gradient-based.

5. Terminate the iteration if the update is within a predefined tolerance ϵ

$$\left\| \mathbf{e}^k - \hat{\mathbf{y}}^k \right\|_2 < \epsilon,$$

6. Otherwise go to step 2, calculate $\hat{\mathbf{y}}^{k+1}$ to continue iteration

$$\hat{\mathbf{y}}^{k+1} := \mathbf{A}\hat{\mathbf{x}}^{k+1}.$$

In general, iterative reconstruction starts with an initial estimation of an image which is usually 0 or the result of FBP. Then, the forward projection is applied to the image to create a simulated sinogram. The simulated sinogram is compared with the actual raw data measured on the scanner in order to calculate the quantity of projection difference. The projection difference is an indicator of whether the iteration should stop or not. For instance, if the projection difference is less than a predefined tolerance, then the iteration stops and the current image is saved as the final result. Otherwise, the image itself becomes updated based on the projection difference. Next, the simulated sinogram will be generated based on the newly updated image, and followed by the calculation of the new projection difference. A maximum iteration number can act as a stop criterion, if the projection difference does not end within the predefined tolerance. Note that the iterative methods for MRI share similar principles, except that the projected data is k-space data instead of a sinogram and the projection and backprojection correspond to Fourier transform and inverse Fourier

transform. The illustration of iterative reconstruction of CT imaging is shown in Figure 2.11 [12].

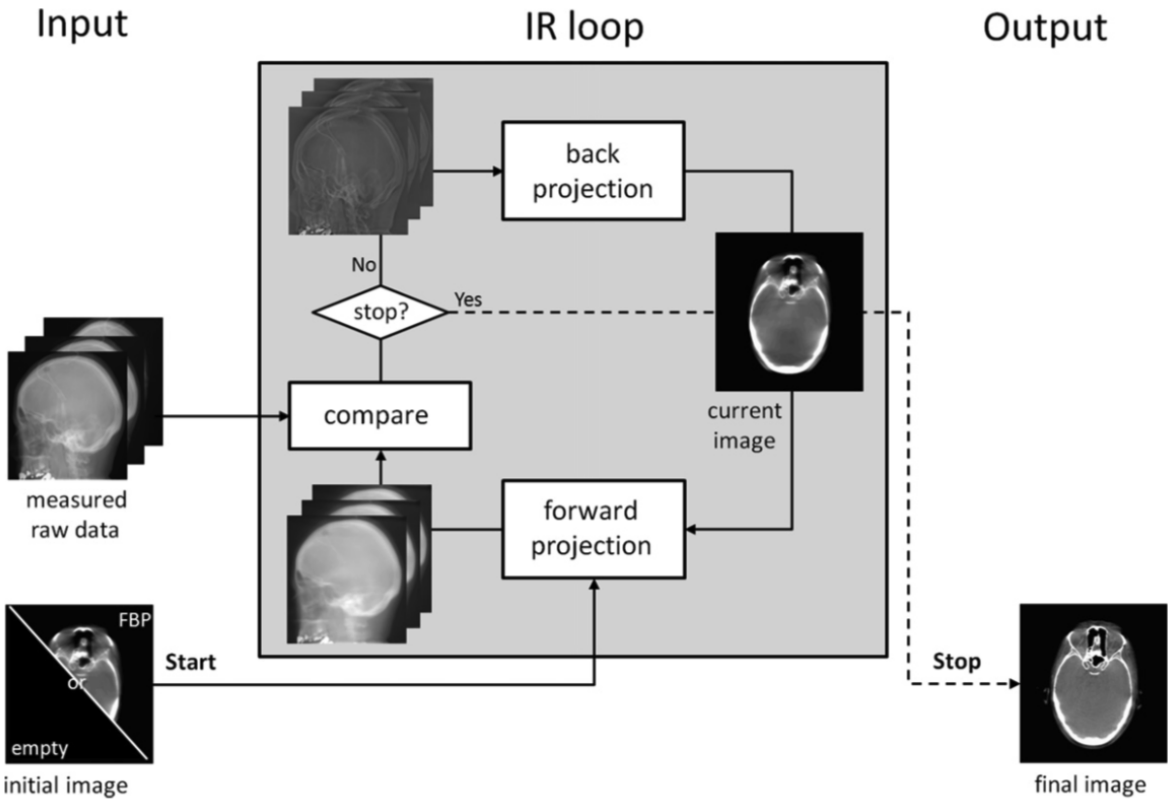

Figure 2.11: Illustration of major steps of how CT iterative image reconstruction proceeds. Initial image usually starts with 0 or FBP. The image is then forward projected following Radon transform to generate simulated sinogram. The simulated sinograom is then compared with the measured raw data to see if the estimate of the image is sufficiently accurate. If yes, then the iteration stops and current image is output as the final result. Otherwise, the image itself becomes updated and the simulated sinogram will be generated based on the newly updated image, and the iteration will continue on.

2.4.2 Algebraic Reconstruction Technique

Algebraic reconstruction technique (ART) is one simple form of an iterative method, and has been used for the tomographic image reconstruction since the 1970s. ART is also known

as Kaczmarz method or Kaczmarz's algorithm in numerical linear algebra [66, 67]. The Kaczmarz algorithm is a general solution method to cope with any linear system, which makes it appropriate for a broad range of applications related to signal processing and image processing. The Kaczmarz algorithm is one of the projections-onto-convex-sets (POCS) algorithms [66, 67, 68] as each linear equation in the system can be viewed as a convex hyperplane.

The Kaczmarz method works by projecting the current estimate onto next convex set (hyperplane) to obtain update at each iteration until the solution eventually converges. Suppose $\mathbf{A}$ is a $M \times N$ matrix, $i = (k+1 \mod M)$ is the index to i-th row, and k is index of iteration. The $(k+1)$th estimate of $\mathbf{x}$ is therefore

$$\mathbf{x}^{k+1} = \mathbf{x}^k + \alpha \frac{\mathbf{a}_i^*}{\|\mathbf{a}_i\|_2^2}, \tag{2.18}$$

Since the $\mathbf{x}^{k+1}$ is in next hyperplace, we have

$$\mathbf{y}_{i+1} = \langle \mathbf{a}_{i+1}, \mathbf{x}^{k+1} \rangle, \tag{2.19}$$

where $<,>$ depicts dot product. By inserting Equation 2.18 into Equation 2.19, α can be solved as

$$\alpha = \frac{\mathbf{y}_i - \langle \mathbf{a}_i, \mathbf{x}^k \rangle}{\langle \mathbf{a}_i, \mathbf{a}_i^* \rangle} \tag{2.20}$$

Equation 2.18 to Equation 2.20 leads to the update of $\mathbf{x}$ as

$$\mathbf{x}^{k+1} = \mathbf{x}^k + \frac{\mathbf{y}_i - \langle \mathbf{a}_i, \mathbf{x}^k \rangle}{\|\mathbf{a}_i\|_2^2} \mathbf{a}_i^*. \tag{2.21}$$

If the linear system has a unique solution, $\mathbf{x}^k$ converges to the minimum-norm solution. ART is essentially a more generalized Kaczmarz method by adding a relaxation parameter λ_k as shown in Equation 2.22. This modification makes the algorithm suited for sparse data and irregular sampling patterns.

$$\mathbf{x}^{k+1} = \mathbf{x}^k + \lambda_k \frac{\mathbf{y}_i - \langle \mathbf{a}_i, \mathbf{x}^k \rangle}{\|\mathbf{a}_i\|_2^2} \mathbf{a}_i^* \tag{2.22}$$

There are other ART-type algorithms that can improve the original method. Simultaneous algebraic reconstruction techniques (SART) for example, update the entire data set instead of processing data in a row-wise fashion as is accomplished by the original ART [12]. SART generates reconstructions with much fewer number of iterations due to its much faster convergence. The simultaneous iterative reconstruction technique (SIRT) updates the complete projection difference simultaneously and weighs shorter light paths with larger weight [12]. SIRT also leads to the least square solution with relatively fast convergence. On top of these methods, ordered subsets are created to bring about OS-SART and OS-SIRT. The idea of ordered subsets is to further accelerate the time of convergence. It groups data into subsets such that the iteration occurs within each subset instead of globally [12]. As the number of subsets increases, the speed of convergence increases as well. However, ordered subsets-based methods are known to be sensitive to noise when excessive numbers of subsets are constructed [12]. Other methods such as multiplicative algebraic reconstruction technique (MART) are essentially different variants of ART. It is important to note that ART-type methods do not incorporate statistical details in the framework of reconstruction.

2.4.3 Statistical Methods

Statistical methods, on the other hand, are another group of algorithms that handle iterative reconstructions. The major difference between statistic methods and ART is that statistic methods incorporate statistical details of the imaging system into the reconstruction process. In reality, there are primarily two types of noise for an X-ray CT imaging system: photonic noise and electronic noise. The former arises from the process of X-ray detectors receiving X-ray photons, and it basically follows a Poisson distribution [69]. The latter is due to electronics in the detector hardware, and it can be approximated by a Gaussian distribution [69]. This assumption is usually accurate except when the electronic noise is much higher than the photonic noise. Compared to ART-type methods, these system-related details can be better described by statistical methods.

Unlike ART-type methods, statistical reconstruction methods can work in either image domains or raw data domains. Therefore, they have the flexibility of working with different image reconstruction algorithms [12]. Typically, a statistical method should have following five components in its mathematical model: [70]

1. An object model that is parameterized as the function of an unknown.
2. A system model that normally is $\mathbf{Ax} + \sigma$.
3. A statistical model that primarily describes Gaussian or Poisson noise.
4. A object function usually consisting of data fidelity and regularization.
5. An algorithm to solve the optimization problem.

Although there are still many open problems in statistical methods such as physical modeling and algorithmic selection, all major vendors have developed statistical-based methods on

their commercial CT scanners. Table 2.1 lists all iterative reconstruction products developed by major vendors. The majority of products in Table 2.1 are statistical-based and have shown potential of dose minimization.

Table 2.1: Commercial Iterative Reconstruction Products From Major Vendors [12]

Acronym	Full Name	Vendor
ASIR	Adaptive statistical iterative reconstruction	GE Healthcare
MBIR	Statistical model based iterative reconstruction	GE Healthcare
iDose		Philips Healthcare
AIDR	Adaptive iterative dose reduction	Canon Medical
IRIS	Image reconstruction in image space	Siemens Healthcare
SAFIRE	Sinogram affirmed iterative reconstruction	Siemens Healthcare

2.5 Comparison Between Analytical Methods and Iterative Methods

The major advantages of the iterative approaches over analytical methods lie into two aspects: 1. it provides tremendously improved robustness when reconstructing data recorded with low dose; 2. it offers the possibility of recovering an (highly) undersampled image with an optimal solution. Until this time, iterative methods have been developed for almost all major imaging modalities such as CT, MRI, PET, and others. Examples of applications of iterative methods to CT imaging include interior CT [23, 24], cardiac CT [71], or metal artifacts reduction[7, 72]. Similarly, iterative methods can also be used in an MRI to skip k-space samples. For example, the iterative algorithm-based compressed sensing techniques can reconstruct MRI images with only a small portion of k-space samples [27, 10, 47, 48].

Figure 2.12 shows a comparison between an analytical method and an iterative method. The effective radiation dose of regular CT abdomen and pelvis protocols is appproximately 15

mSv. The GE dual energy CT which utilizes an ASIR [73] algorithm can perform follow-up CT KUB exams at approximately 1-2 mSv, or 3-5 mSv for larger patients [6].

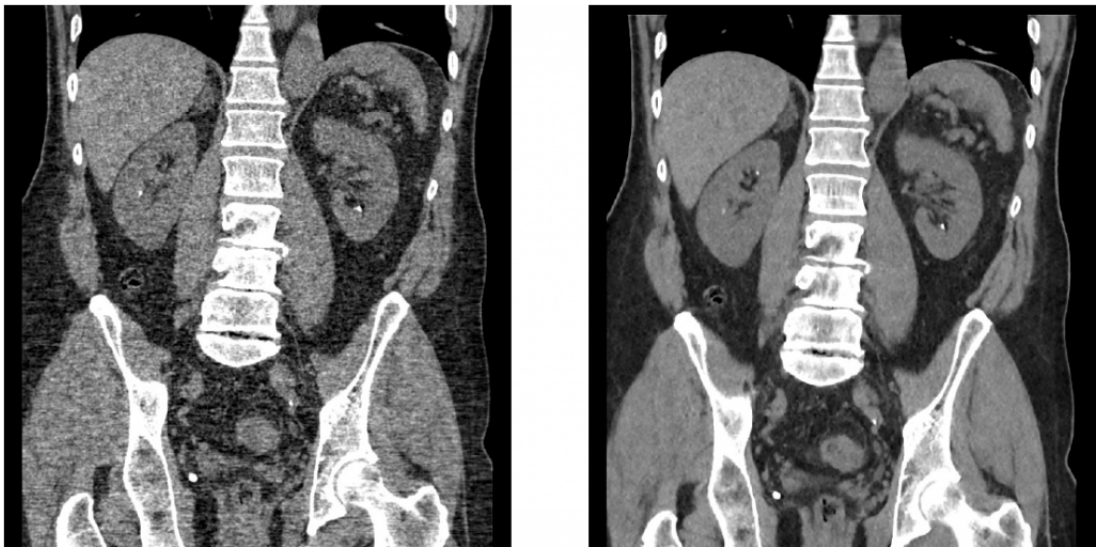

Figure 2.12: FBP compared to ASIR. Left: low dose reconstruction with FBP; Right: low dose reconstruction using ASIR technique. Both images are reconstructed under the same dose [6].

Figure 2.13 shows images reconstructed using the Philips MX16^{EVO} CT with an iterative-based O-MAR (metal artifact reduction for orthopedic implants) algorithm [7]. The enhancement of visualization of the surrounding anatomy is significant compared to the uncorrected image on the left panel.

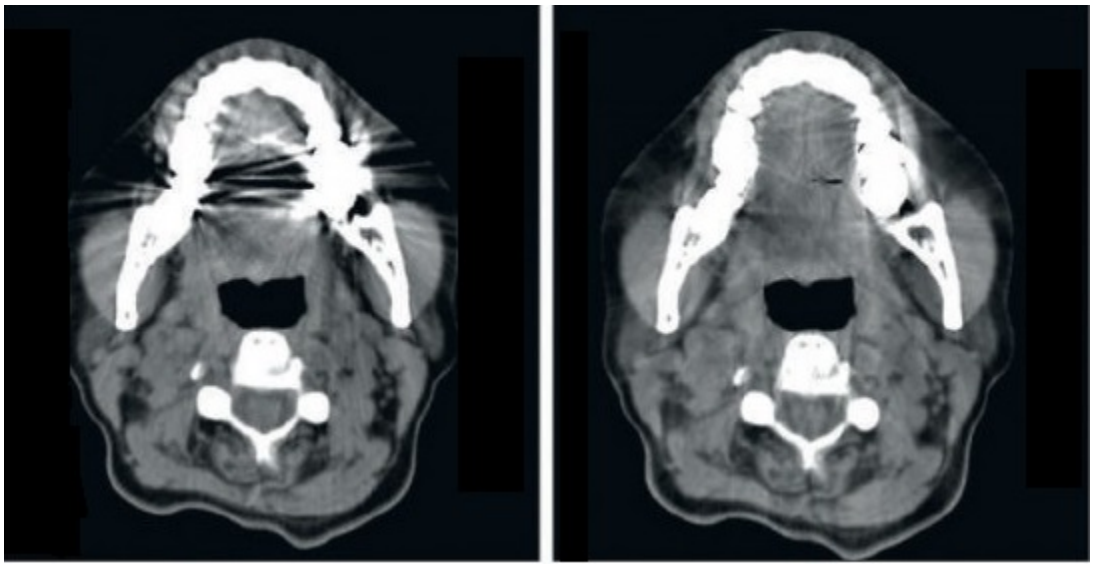

Figure 2.13: Metal artifacts caused by dental implants. Left: uncorrected image; Right: corrected image using an iterative-based O-MAR algorithm [7].

Figure 2.14 displays an example of low dose pediatric CT imaging that employs an iterative reconstruction. In this case, SAFIRE [8] (Siemens Medical Solution) decreases the image noise by $\sim$ 35 % and improves both signal-to-noise-ration and contrast-to-noise-ratio by $\sim$ 50% each while maintaining comprable Hounsfield units compared to full dose scanning [8].

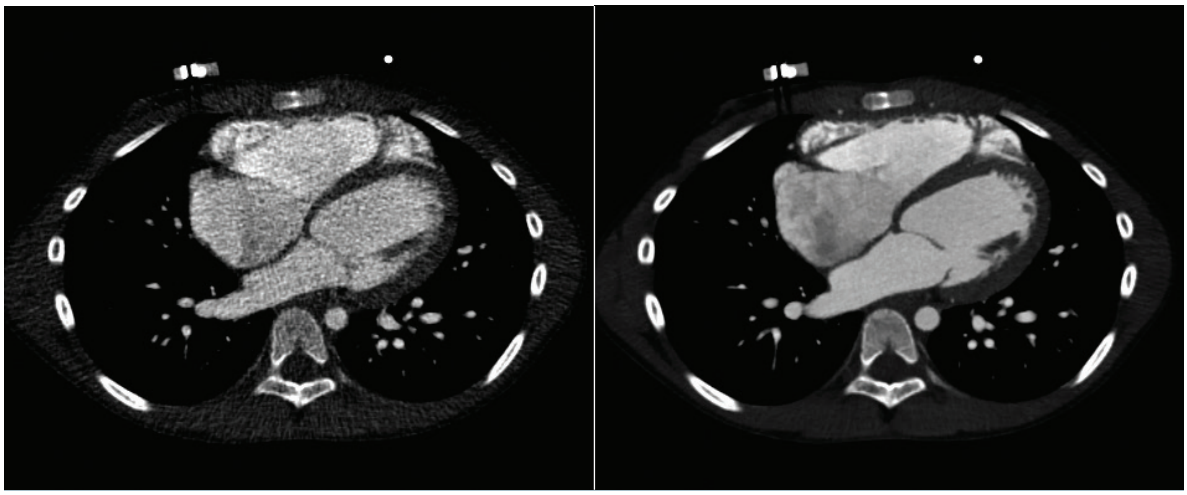

Figure 2.14: Low dose pediatric heart CT imaging ; Left: standard weighted FBP reconstruction; Right: iterative-based SAFIRE reconstruction [8].

2.6 Summary

The X-ray CT imaging systems collect data by spraying X-rays through the object of interest. The amount of radiation absorbed by the object is directly related to the intrinsic property of the object itself. Therefore, CT reconstruction provides an image of X-ray attenuation distribution of the unknown object.

MRI, from another standpoint, measures the proton density within each tissue being scanned. Firstly, by creating a homogeneous external magnetic field, then a MRI system uses a RF pulse to knock the proton spin off its equilibrium such that the signal of the spinning proton can be recorded. The image reconstruction of MRI is essentially a Fourier transform with either a Cartesian or non-Cartesian trajectory.

Although analytical solutions such as filtered backprojection and Fourier transform have been widely used, they sometimes cannot provide acceptable image qualities. Iterative methods, as an alternative, can compensate for many kinds of artifacts such as streaks and blurs in many cases where analytical methods fail. In contrast to analytical methods, statistical models can be incorporated into the reconstruction framework such that the physics of the imaging systems is accounted for. In particular, iterative methods have shown outstanding performance in dealing with signal recovery problems from extremely undersampled data sets, and this will be further described in Chapter 3.

Chapter 3

UNDERSAMPLED IMAGE DATA AND COMPRESSED SENSING

Modern clinical applications require image data to be sufficiently sampled such that the quality of reconstructed images is guaranteed. The definition of sufficiency can be traced to the Shannon-Nyquist sampling theorem. However, in reality the image data are almost always oversampled such that an adequate margin of sampling is kept and the imaging procedure captures all the necessary information.

The concept of "over sampling" is feasible for many applications except that X-ray CT imaging risks patients by exposing them to ionizing radiation. A patient cannot repeatedly receive X-ray CT scanning due to its known hazardous effects. Therefore, dose minimization in X-ray imaging is constantly pursued. Similarly, undersampling in MRI is also an interesting topic because the scanning time of MRI is lengthy. Therefore, technologies that can shorten the MRI scanning time is of high interest in the field.

The major challenge in reconstructing images from undersampled data is the maintenance

of the same or quasi-optimal image quality as fully sampled data. Analytical methods such as FBP, which requires a large amount of samplings, can no longer provide image quality if data are undersampled. Compressed sensing, on the other hand, provides a solution to handle significantly undersampled data in signal recovery. In addition, sparse representation and sampling patterns are essential in compressed sensing theory to reconstruct unknown signals.

3.1 Undersampling in Medical Image Data

3.1.1 X-ray CT Dose

Modern CT applications are generally X-ray-based. X-rays are a form of energy, and therefore are also a form of radiation. Compared to light waves, X-rays have a much stronger intensity allowing it to penetrate objects such as the human body. As the radiation travels through patients' bodies, the radiation dose can be recorded based on the amount of X-ray dose deposited in the entire body. The measurement of the whole body X-ray dose is called the "effective dose," and the scientific unit for the effective dose is the Sievert [74] which is defined in Formula 3.1.

$$1Sievert = \frac{1Joule}{1Kilogram}. \tag{3.1}$$

The Sievert physically means the equivalent biological effect for a kilogram of human tissue to receive a Joule of X-ray energy. Note that a Sievert is a fairly large unit and therefore millisievert (mSv) is often used in practice.

It should be pointed out that radiation from natural sources are ubiquitous at all times.

Table 3.1: Typical X-ray CT Radiation Dose [13]

Procedure	Effective Dose	Equivalent Length of Background Radiation
Lung Cancer Screening	1.5 mSv	6 months
Chest	7 mSv	2 years
Head	2 mSv	8 months
Head, repeated	4 mSv	16 months
Coronary Angiography	12 mSv	4 years
Spine	6 mSv	2 years
Abdomen and Pelvis	10 mSv	3 years
Abdomen and Pelvis, repeated	20 mSv	7 years
Colonography	6 mSv	2 years
PET/CT	25 mSv	8 years

According to United States Nuclear Regulotory Commission (NRC), the average amount of effective dose received by a person in the United States is approximately 3.1 mSv per year [75]. These doses are referred to as "background radiation," and they are from natural sources such as cosmic radiation from outer space. Table 3.1 lists the equivalent time of receiving background radiation for an effective X-ray dose for some most commonly used CT scan protocols [13].

The estimated effective doses of commonly practiced CT scan protocols are typically from 1 to 10 mSv. These amounts are not very far from that what was received by some of the survivors of the nuclear bomb attack on Hiroshima and Nagasaki in Japan during World War II, who had doses ranging from 5 to 20 mSv. X-ray CT radiation is known to be potentially hazardous. This is due to the fact that X-rays carry sufficiently high energy to ionize atoms. Ionizing radiation is widely considered to cause damage to human cells, and potentially to increase the chances of developing cancer [76]. Specifically, a X-ray CT scan with an effective dose of 10 mSv may increase the possibility of fatal cancer by approximately 1 chance in 2000 [76]. Therefore, X-ray dose minimization is of utmost importance in CT imaging research.

3.1.2 MRI Acceleration

Similarly, MRI Acceleration is one of the most active topics being researched today, as MRI scan times are a serious consideration for patients, clinicians, and technologists performing the exam. Modern MRI scans usually take between 10 minutes to over an hour to complete, and is dependent on the part of the body being imaged and what type of MRI is required to show a specific type of information. When a patient remains still inside a MRI gantry for nearly an hour, it is nearly impossible to avoid motion effects that negatively impact image quality. Hence, imaging times and image quality are inversely related. Table 3.2 provides several typical scanning times of some of the most common MRI protocols.

On the other hand, MRI scanning time is also related to image resolution. However, to improve the image resolution often leads to having more sampling in k-sapce, which leads to longer scanning times. This, in return, raises the cost of an MRI unit as well as MRI scanning. Therefore, reduction of scan times is preferably achieved by applying advanced algorithms to compensate for speed and/or undersampling. These techniques include SENSitivity Encoding (SENSE) and compressed sensing. The former can cope with aliasing artifacts by utilizing the sensitivity profiles of different receiving coils positioned by the patient. The latter can recover an undersampled signal with high quality by finding its sparse representation [77].

3.1.3 Shannon-Nyquist Sampling Theorem and Aliasing

The Shannon-Nyquist sampling theorem is the canonical principle in signal processing to govern the sampling strategy such that aliasing can be avoided in signal recovery. This theory bridges the gap between analog and digital signals by giving a sufficient condition for a sampling rate which ensures the information of the original continuous signal to be fully

Table 3.2: Typical MRI Scanning Time [14]

Protocol	Time
Brain	20-45 minutes
Chest	25-45 minutes
Magnetic Resonance Cholangiopancreatography	50-60 minutes
Abdomen	25-45 minutes
Lumbar Spine	20-35 minutes
Soft Tissue Neck	25-35 minutes
Thoracic Spine	25-45 minutes
Pelvis	20-35 minutes
Arthrogram	30-60 minutes
Temporomandibular Joint	45-60 minutes

captured by the discrete samples.

In Shannon's work [78] states that "If a function $x(t)$ contains no frequencies higher than B hertz, it is completely determined by giving its ordinates at a series of points spaced $1/(2B)$ seconds apart." A sufficient sampling rate must therefore be beyond $2B$ samples per second. Likewise, for a given sampling rate f_s, proper reconstruction is guaranteed only when the bandlimit $B < f_s/2$.

Let us consider a continuous-time signal $x(t)$ and its sampled version $x_s(t)$ which is defined as

$$x_s(t) = x(t) \sum_{n=-\infty}^{\infty} \delta(t - nT), \tag{3.2}$$

where T is the sampling period. Then the sampling frequency f_s measured in Hertz, and ω_s measured in radians/second are defined as

$$f_s = \frac{1}{T} \tag{3.3}$$

and

$$\omega_s = \frac{2\pi}{T}, \tag{3.4}$$

respectively. $\sum_{n=-\infty}^{\infty} \delta(t - nT)$ in Equation 3.2 is also referred to as impulse train, and it can be represented by its Fourier series as

$$\sum_{n=-\infty}^{\infty} \delta(t - nT) = \frac{1}{T} \sum_{k=-\infty}^{\infty} e^{j\omega_s k}, \tag{3.5}$$

where j is the imaginary unit defined as

$$j = \sqrt{-1}. \tag{3.6}$$

Therefore, by replacing the impulse train in Equation 3.2 with its Fourier series representation in Equation 3.5, results in

$$x_s(t) = x(t) \sum_{n=-\infty}^{\infty} \delta(t - nT) = x(t) \frac{1}{T} \sum_{k=-\infty}^{\infty} e^{j\omega_s k} = \frac{1}{T} \sum_{k=-\infty}^{\infty} x(t) e^{j\omega_s k}. \tag{3.7}$$

A Fourier transform on both sides of Equation 3.7, results in

$$X_s(\omega) = \frac{1}{T} \sum_{k=-\infty}^{\infty} X(\omega - k\omega_s). \tag{3.8}$$

The Fourier transform of a function $x(t)$ is defined as

$$X(\omega) \overset{\text{def}}{=} \int_{-\infty}^{\infty} x(t)\ e^{-j\omega t}\ \mathrm{d}t, \tag{3.9}$$

and the inverse Fourier transform is defined as

$$x(t) \stackrel{\text{def}}{=} \frac{1}{2\pi} \int_{-\infty}^{\infty} X(\omega)\, e^{j\omega t}\, \mathrm{d}\omega. \tag{3.10}$$

It can be observed from Equation 3.8 that sampling a continuous signal generates replicas in the Fourier domain. These replicas potentially causes different signals to become indistinguishable, known as aliasing. Aliasing is a phenomenon when the continuous signal is sampled. When the original signal is not sampled with sufficiently high frequency, the original continuous signal becomes irrecoverable. Figure 3.1 illustrates the root cause of aliasing, and why sampling twice as the Nyquist frequency can avoid aliasing.

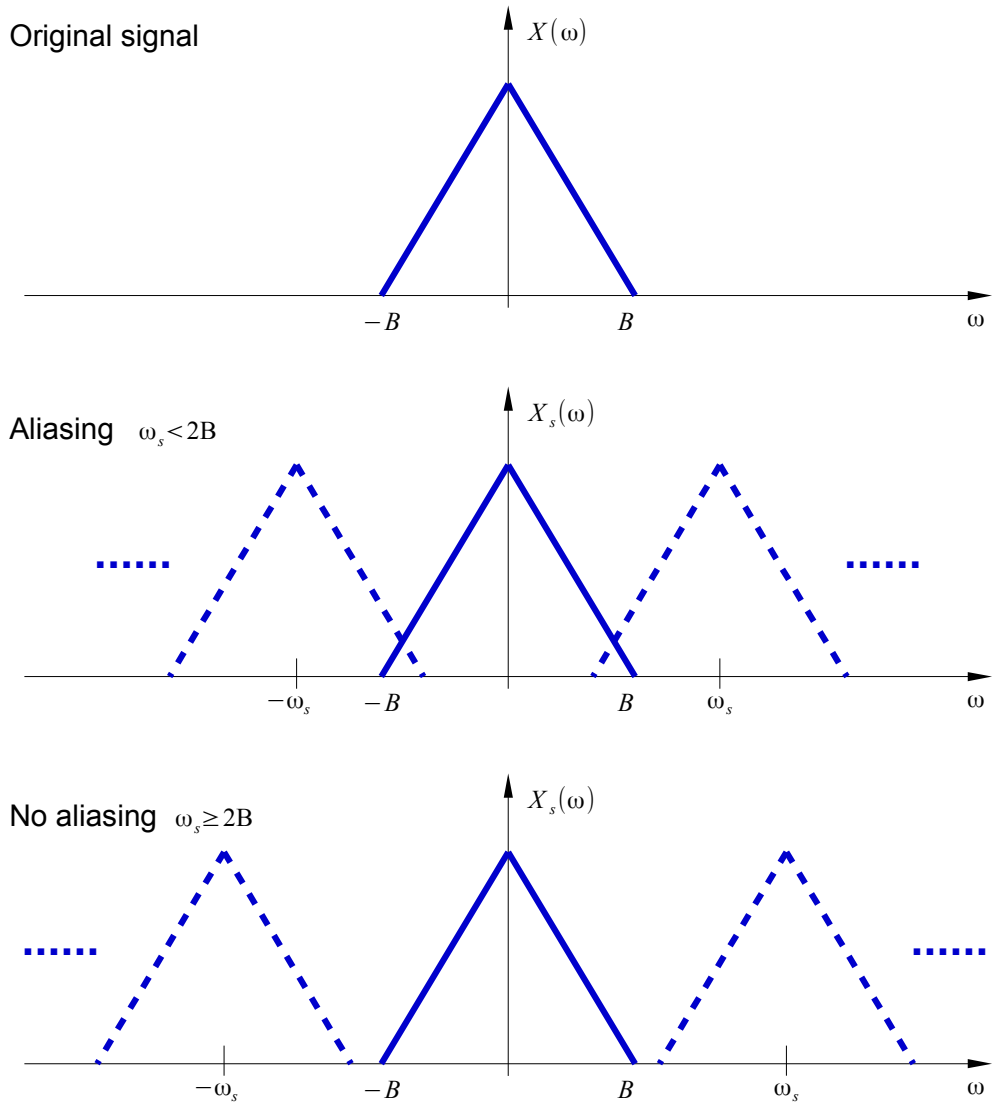

Figure 3.1: The top panel shows $X(\omega)$ the Fourier transform of original signal $x(t)$ which is not shown here. $X(\omega)$ is displayed in frequency domain with ω being in units of radians/second. $X(\omega)$ here is bandlimited with its Nyquist frequency being $\pm B$. Mid-panel shows $X_s(\omega)$ is the Fourier transform of $x_s(t)$ when the original signal $x(t)$ is sampled at rate of ω, where $\omega_s < 2B$. The replicas are depicted in dashed lines and they are centered at $\pm k\omega_s, k = 0, 1, 2, ...$ When the original signal (solid) is overlapped with its replicas (dashed), aliasing occurs. Bottom panel shows $X_s(\omega)$ which is the Fourier transform of $x_s(t)$ when the original signal $x(t)$ is sampled at rate of ω_s, where $\omega \geq 2B$. Since there is no overlap between the original signal (solid) and its replicas (dashed), no aliasing occurs.

3.1.4 Aliasing in CT and MRI

Similarly, when CT and MRI signals are undersampled, aliasing artifacts appear in reconstructed images. The most common aliasing in MRI is "phase wrap-around" which occurs when the predefined FOV (field of view) is not large enough to hold the entire object to reconstruct. The artifact of phase-wrap-around is generally easy to identify as the overlapping occurs in the image domain for signals outside of the FOV. Although these particular artifacts may occur occasionally in the frequency encoding direction (x direction), it is generally more often in the phase encoding direction (y direction).

The relation between (FOV_x, FOV_y) in image domain and sampling period ($\Delta k_x, \Delta k_y$) in the k-space domain is illustrated in Figure 3.2, and their mathematical relation is defined in Equation 3.11.

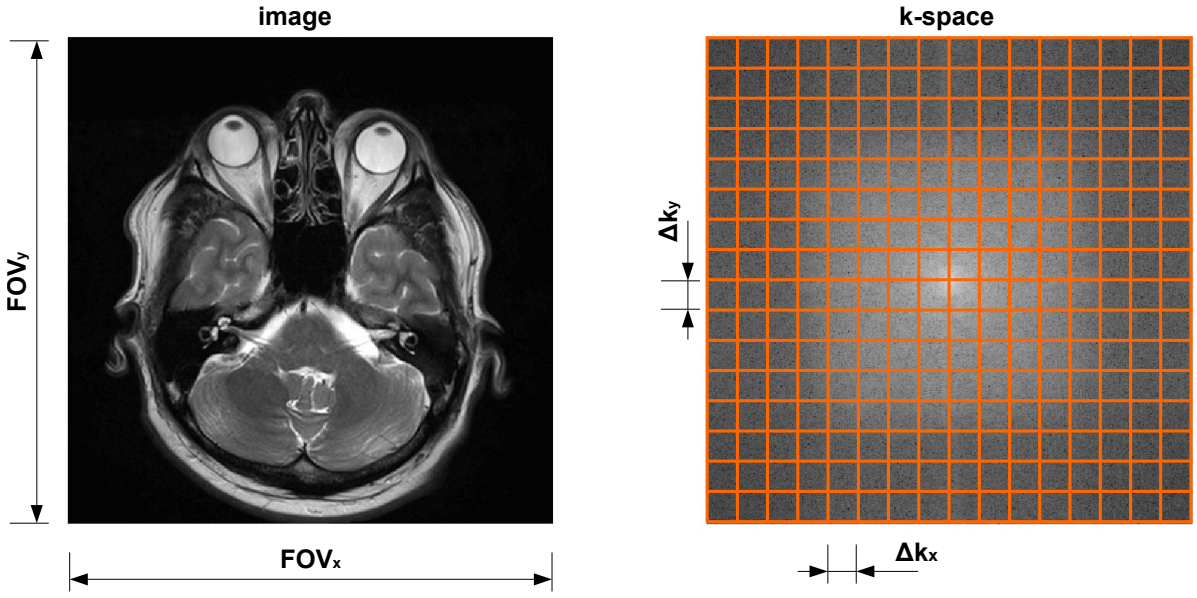

Figure 3.2: (FOV_x, FOV_y) in image domain and ($\Delta k_x, \Delta k_y$) in k-space domain.

$$FOV_x = \frac{1}{\Delta k_x},$$
$$FOV_y = \frac{1}{\Delta k_y} \tag{3.11}$$

The phase wrap-around artifact can be simulated by decimating sampling points in k-space. This is demonstrated in Figure 3.3, where every other row of samples are removed and replaced by zeros. Thus, according to Equation 3.11, it can only support the new FOV which is half of the original in both x and y direction, which leads to aliasing.

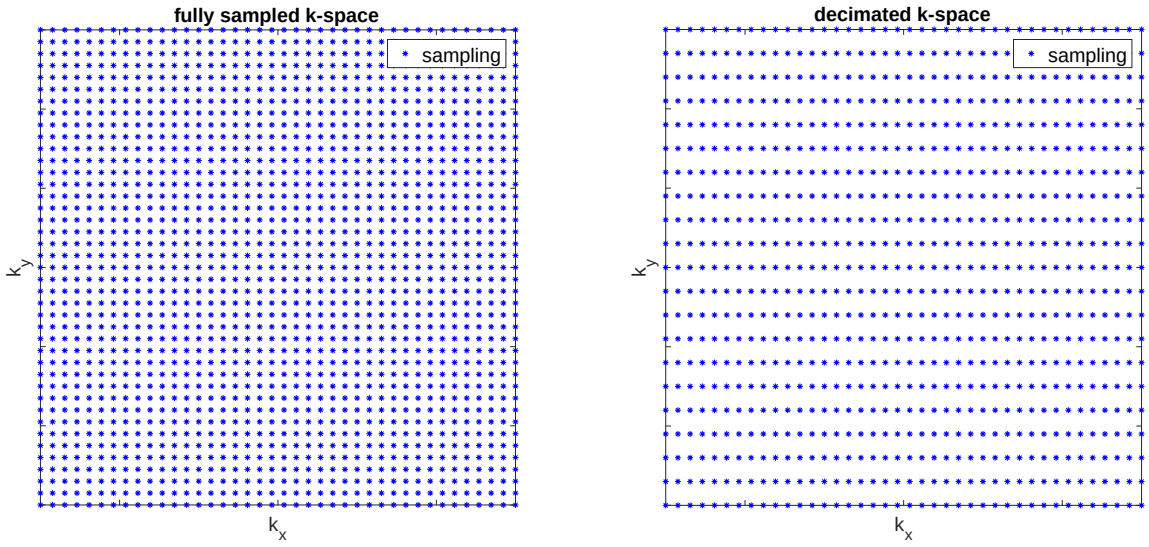

Figure 3.3: k-space decimation changes the FOV it supports. The left panel shows a fully sampled k-space, and the right panel shows the decimation created by removing every other row in the fully sampled in the right panel. The new FOV is consequently halved in y direction.

Figure 3.4 shows how undersampled k-space can cause a phase wrap-around artifact. As the k-space is half sampled in y (phase encoding) direction, the image also replicates itself in

y direction. As Equation 3.8 suggests, the replicas are centered at $\text{FOV}_y/2$. Note that the image is reconstructed through Fourier transform as the canonical analytical method.

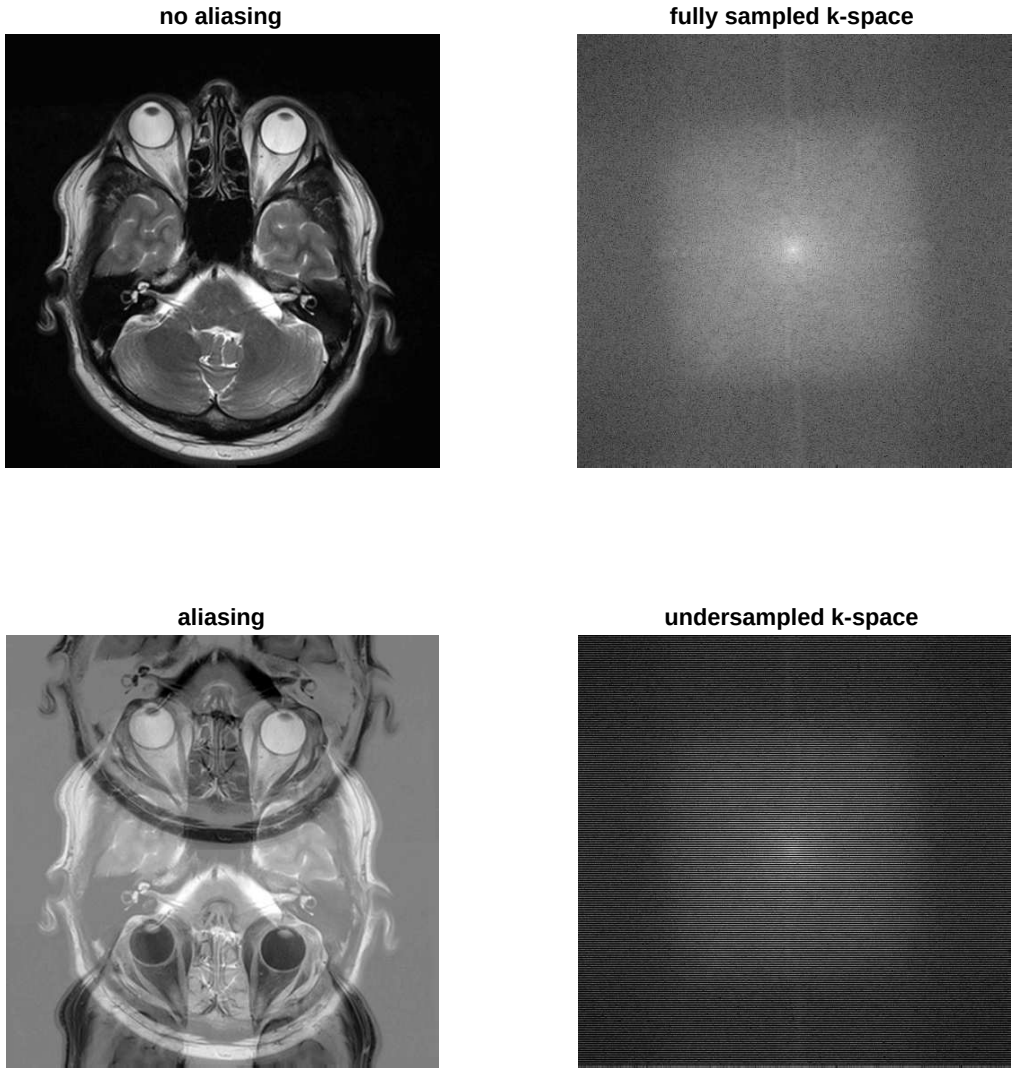

Figure 3.4: MRI reconstruction example showing undersampled k-space data can cause aliasing in final image reconstruction. Top left panel shows an image reconstructed from fully sampled k-space data with no aliasing; Top right panel shows fully sampled k-space data; Bottom right panel shows the undersampled k-space created by choosing every other row of the fully sampled k-space; Bottom left panel shows an image reconstructed from undersampled k-space displayed in bottom right panel.

Like MRI, CT aliasing also occurs if an image is reconstructed through analytical methods when the amount sampling is not sufficient. CT sampling basically consists of two parts: sampling density on each projection and sampling density on the number of views. This means that an object can be acceptably reconstructed with analytical methods if, and only if, it receives

- sufficient number of views of projection from different angles evenly spaced out across 360°,
- and sufficient number of samples on each projection.

Since sampling insufficiency on a projection is thoroughly investigated [25], this work will assume each projection has a sufficient number of samples, and will focus on aliasing that is only caused by an insufficient number of views. In addition, the iterative methods can handle aliasing artifacts without differentiating whether the undersampling is from the angular or the radial direction [25]. Therefore, if the number of views does not meet the Nyquist requirement, the CT image will show aliasing.

According to Fourier-slice theorem described in Section 2.3.1, the collection of projection data from different angles is essentially sampling in a Fourier domain along a radial directions. Therefore, skipping data every other view in a sinogram is equivalent to skipping every other radial in the 2-D Fourier domain. The undersampling strategy is depicted in Figure 3.5.

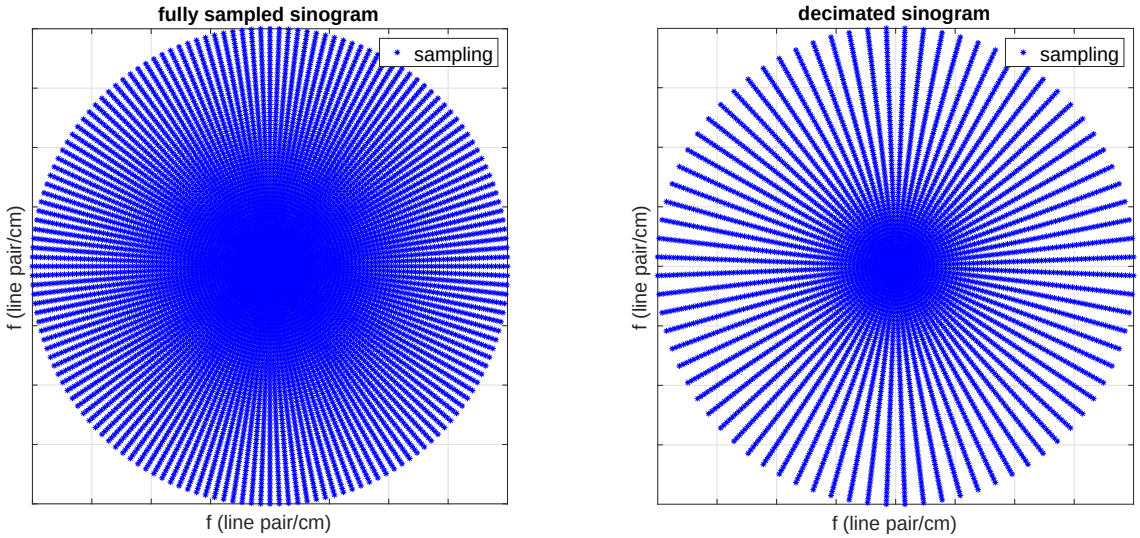

Figure 3.5: CT undersampling by decimating in view angles. The sampling in right panel skips every other view of the samples in left panel. According to Fourier slice theorem, skipping radial samples in Fourier domain is equivalent to skipping views in projection domain.

Figure 3.6 shows an image reconstructed from different number of views ranging from 720 per rotation to 8 per rotation. It clearly shows that as the number of views decreases, the quality of the reconstruction decrease as well. Artifacts caused by aliasing starts to appear when the number of the views down to 180, and become extremely strong at 90 views per rotation.

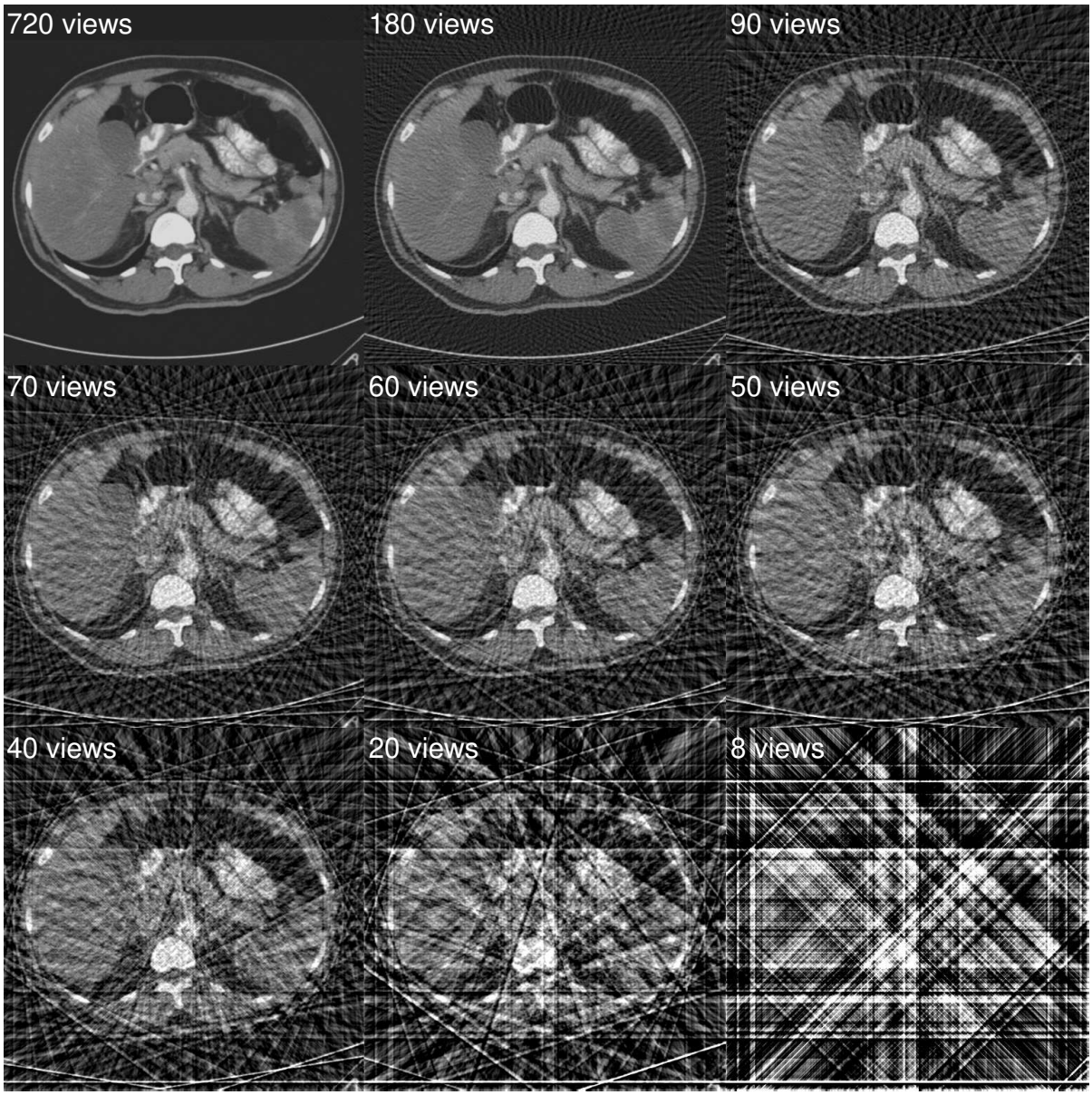

Figure 3.6: Undersampling in the number of views can cause significant aliasing in CT reconstruction. When 720 views per rotation is sampled, the reconstruction shows superior image quality with an FBP algorithm. As the sampling rate decreases to 8 views per rotation, strong aliasing artifacts completely diminish the image quality.

3.2 Compressed Sensing

Compressed sensing, or compressive sensing, is a signal processing technique to find an optimal solution for under-determined linear systems. Compressed sensing focuses on maximizing the efficiency of sampling and reconstructing procedures by strategically collecting the minimal amount of raw data. The main idea of compressed sensing is that a signal is recoverable if its sparsity information is exploited, even though it is sampled with a rate violating the minimum requirement of Shannon-Nyquist sampling theorem. The compressed sensing theory states that the recovery is possible under two conditions: 1) The signal must be sparse in some domain; 2) The signal should be sampled with some random (incoherent) pattern. Accordingly, compressed sensing reconstructs signals with much faster speed due to a significant reduction in the required sampling number.

3.2.1 Underdetermined Linear System

As discussed in Section 3.1, undersampling occurs in medical imaging due to various of reasons such as dose minimization or scanning time reduction. Mathematically, undersampling creates underdetermined systems. In particular, an underdetermined linear system has fewer equations than unknowns, and it generally does not have a unique solution. This is illustrated in Equation 3.12, where $M \ll N$.

$$\begin{bmatrix} y_1 \\ y_2 \\ \vdots \\ y_M \end{bmatrix} = \begin{bmatrix} a_{11} & a_{12} & \dots & a_{1N} \\ a_{21} & a_{22} & \dots & a_{2N} \\ \vdots & \vdots & \ddots & \vdots \\ a_{M1} & a_{M2} & \dots & a_{MN} \end{bmatrix} \begin{bmatrix} x_1 \\ x_2 \\ \vdots \\ x_N \end{bmatrix} \tag{3.12}$$

Undersampled medical imaging systems, such as few-view CT depicted in Figure 3.5 or sparse view MRI in Figure 3.3, cause underdetermined systems which fail the analytical reconstruction methods. In order to solve for such a system, additional constraints or conditions such as smoothness must be introduced. In the theory of compressed sensing, sparsity is added as the extra constraint such that only one solution, which maximizes the number of nonzero coefficients in the sparse domain, is obtained.

3.2.2 Signal Sparse Representation

The concept of sparsty is one of the key components of compressed sensing theory. A signal is considered sparse if the majority of its elements are zero or close to zero. The sparsity of a signal does not necessarily restrict a signal itself to be sparse, but it requires the signal to be recompressible in some sparse domain. Examples of compression techniques such as JPEG, MP3 or MPEG demonstrate that many signals and images can be coded with much less and sparse information than its original version. For instance, the wavelet-based JPEG coding can often achieve a compression ratio over 10:1 [79]. In general, the compressibility of a signal leads to its sparse representation.

In medical imaging science, there are two sparse representations that are commonly used in compressed sensing applications: gradient transform and wavelet transform. An image gradient is a measurement of how its intensity changes in different directions. The gradient of a two-variable function $f(x, y)$ (for example, the intensity function of an image) at each location (x, y) is a 2-D vector with the components given by the derivatives in the x and y directions. At each image location, the gradient vector points in the direction of the strongest possible change in magnitude, and the norm of the gradient vector indicates rate of change in that direction. The gradient of an image f is defined as

$$\nabla f(x,y) = \begin{bmatrix} \nabla f_x \\ \nabla f_y \end{bmatrix} = \begin{bmatrix} \frac{\partial f}{\partial x} \\ \frac{\partial f}{\partial y} \end{bmatrix} \tag{3.13}$$

where $\frac{\partial f}{\partial x}$ is the partial derivative with respect to x, $\frac{\partial f}{\partial y}$ is the partial derivative with respect to y. Also, the direction of gradient is calculated by

$$\theta = \tan^{-1}\left[\frac{\nabla f_y}{\nabla f_x}\right], \tag{3.14}$$

and its magnitude is given by

$$\sqrt{\left(\nabla f_y\right)^2 + \left(\nabla f_x\right)^2}. \tag{3.15}$$

Figure 3.7 shows an abdomen CT phantom image [9] and the magnitude of its gradient transform. Note that the phantom image itself is originally not sparse, but its gradient transform is. Hence, the gradient transform is one form of a sparse representation of an image.

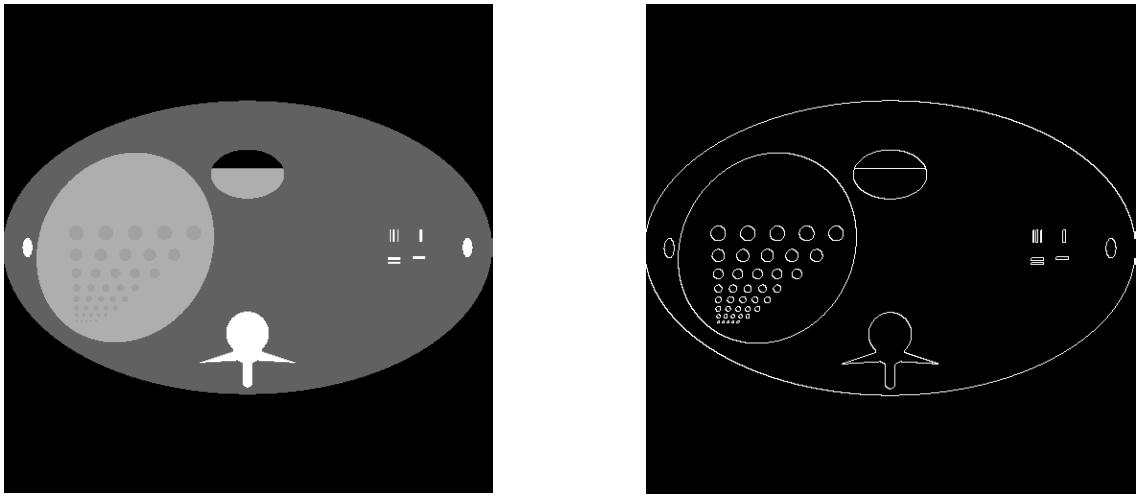

Figure 3.7: Undersampling in the number of views can cause significant aliasing in CT reconstruction. When 720 views per rotation is sampled, the reconstruction shows superior image quality with FBP algorithm. As the sampling rate decrease to 8 views per rotation, strong aliasing artifacts completely diminish the image quality.

One way to measure the sparsity of a gradient image is to compute its total variation (TV). In continuous case, the TV of an image is defined as

$$\|f\|_{TV} = \int_{\Omega} \|\nabla f(x)\|_1 \mathrm{d}x, \tag{3.16}$$

where $\nabla f(x)$, defined in Equation 3.13, denotes the gradient transform of the image $f(x)$, $\|\cdot\|_1$ denotes the L_1-norm operator, and Ω denotes the entire image space. In discrete cases of a $N \times N$ 2-D digital image with unity grid length, the TV is approximated by finite difference becomes

$$\|f\|_{TV} = \sum_{i,j}^{N,N} \|\nabla f_{i,j}\|_1, \tag{3.17}$$

where $\nabla f_{i,j}$ denotes the DGT defined at location (i, j). In particular, $\nabla f_{i,j}$ is formulated as

$$\nabla f_{i,j} = \begin{bmatrix} f^x_{i,j} \\ f^y_{i,j} \end{bmatrix} = \begin{bmatrix} f_{i+1,j} - f_{i,j} \\ f_{i,j+1} - f_{i,j} \end{bmatrix}. \tag{3.18}$$

The notation $\|\cdot\|_1$ in Equation 3.16 and Equation 3.17 is the L_1-norm defined as

$$\|x\|_1 = |x_1| + |x_2| + \cdots + |x_n|. \tag{3.19}$$

where $x_k, k = 1, ..., n$ are the components of vector x.

Apart from gradient transform, wavelet transform can also map a signal into its sparse representation. Wavelet transform decomposes a signal into a linear combination of orthonormal wavelet bases that are generated from a single mother wavelet ψ. For instance, the Hilbert basis is defined as [48]

$$\psi_{s,\tau}(t) = \frac{1}{\sqrt{s}}\psi\Big(\frac{t-\tau}{s}\Big), \tag{3.20}$$

where s and τ are parameters of dilation and translation. In practice, they are digitized as dyadic integers. The wavelet coefficient w is computed using wavelet transform defined as

$$w_{s,\tau} = \int_{-\infty}^{\infty} x(t)\psi^*_{s,\tau}(t)dt, \tag{3.21}$$

where $\psi^*_{s,\tau}(t)$ is the conjugate of $\psi_{s,\tau}(t)$. When the wavelet transform is orthogonal, $\psi^*_{s,\tau}(t)$ is the Hermitian adjoint of $\psi_{s,\tau}(t)$ [62]. To recover the original signal, the inverse wavelet transform is computed as

$$x(t) = \int_{-\infty}^{\infty}\int_{0}^{\infty} w_{s,\tau}\psi_{s,\tau}(t)dsd\tau. \tag{3.22}$$

The 2-D wavelet transform is capable of generating a sparse representation of an image by turning transient structures into only a few coefficients. Large wavelet coefficients are located in the neighborhood of edges and irregular textures [80]. As with the 1-D wavelet transform, the 2-D wavelet transform makes use of different wavelet bases such as Haar or Daubechies wavelet.

The typical processing of a one-level 2-D discrete wavelet transform is to first pass the image through a low-pass filter to generate approximation coefficients. At the same time, the image is also decomposed with a high-pass filter to generate detailed coefficients. It is critical that the two filters are quadrature mirror of each other [80]. Then, both approximations and detailed coefficients are downsampled by 2. By doing so, one can find the next level of wavelet coefficients. Multiresolution analysis is achieved by repeatedly computing convolution and downsampling. Figure 3.8 shows a three-level 2-D discrete wavelet transform of a CT head phantom [9] using Daubechies wavelet with four vanishing moments.

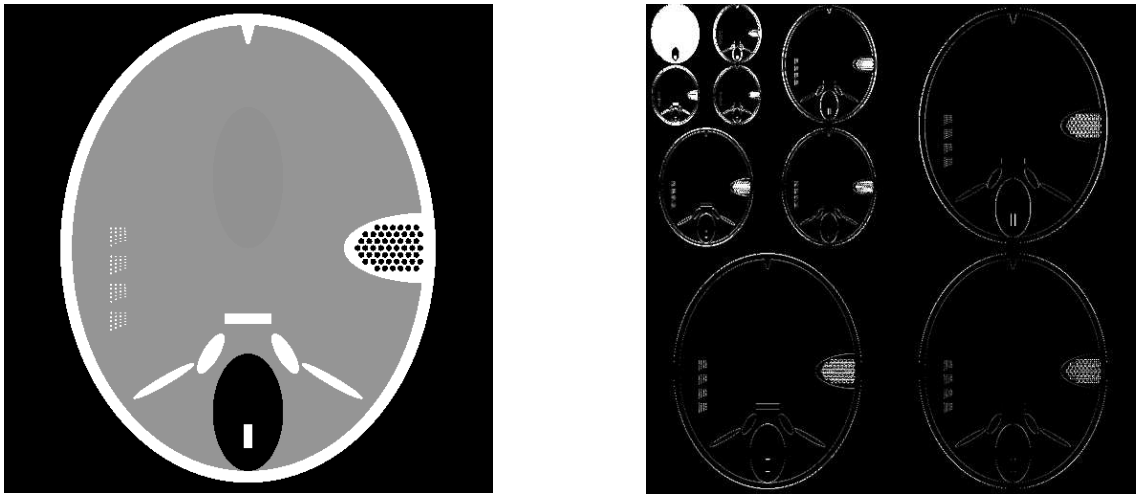

Figure 3.8: Three-level 2-D discrete wavelet transform of an CT head phantom [9] using Daubechies wavelet with four vanishing moments.

3.2.3 L_1-norm Minimization and Signal Reconstruction

In compressed sensing theory, sparsity plays a key role in restoring an undersampled signal. The signal is recovered by finding the solution that promotes the sparsity at its highest. In order to do so, the quantification of the level of sparsity becomes important. One obvious way to measure the sparsity is to simply sum all the non-zero coefficients together. This summation can actually be generalized as L_p-norm, which is defined as

$$\|\mathbf{x}\|_p = \left(\sum_{n=1}^{\infty} |x_n|^p \right)^{\frac{1}{p}}, \tag{3.23}$$

where $p \in \mathbb{R}^+$. It should be noted that L_1-norm regularization is also referred as LASSO regularization in some literature [48].

A canonical solution is the least-squares problem that minimizes the L_2-norm, which essentially favors the solution with the minimum amount of energy in the system. In general, to obtain L_2-norm solution is relatively mathematically simple, because it can be found using the singular value decomposition (SVD) and/or the Moore-Penrose pseudoinverse [81]. However, L_2-norm minimization produces poor results for many practical applications when the actual unknown has large energy. In the end, it is the energy, instead of the sparsity, that is penalized.

In theory, L_0-norm is the perfect candidate for the best performance of sparsity enhancement because it only counts the number of non-zero coefficients. Therefore, to promote the sparsity when solving for the underdetermined linear system, sparsity maximization can be achieved by minimizing the L_0-norm of the solution. However, solving problems related to L_0-norm minimization is known to be NP-hard as mentioned in the literature [82, 83, 48] .

In recent years, Cands, Donoho, Tao, and others proposed an alternative approach for L_0-norm minimization. They proved that for many practical senarios it is simply equivalent to perform L_1-norm minimization for L_0-norm minimization problems [29, 30, 31, 84]. This discovery is a breakthrough because it justifies that a solution for a compressed sensing problem can be found through L_1-norm minimization. Obtaining the solution for minimal L_1-norm can be considered relatively easy as an optimization problem, for which a number of efficient numerical solutions are available[29, 30].

Figure 3.9 shows a visual comparison among L_0-norm, L_1-norm, and L_2-norm. As the plot suggests, as the power of norm p (defined in Equation 3.23) grows, the penalty rises exponentially as the value of the non-zeros coefficients increases.

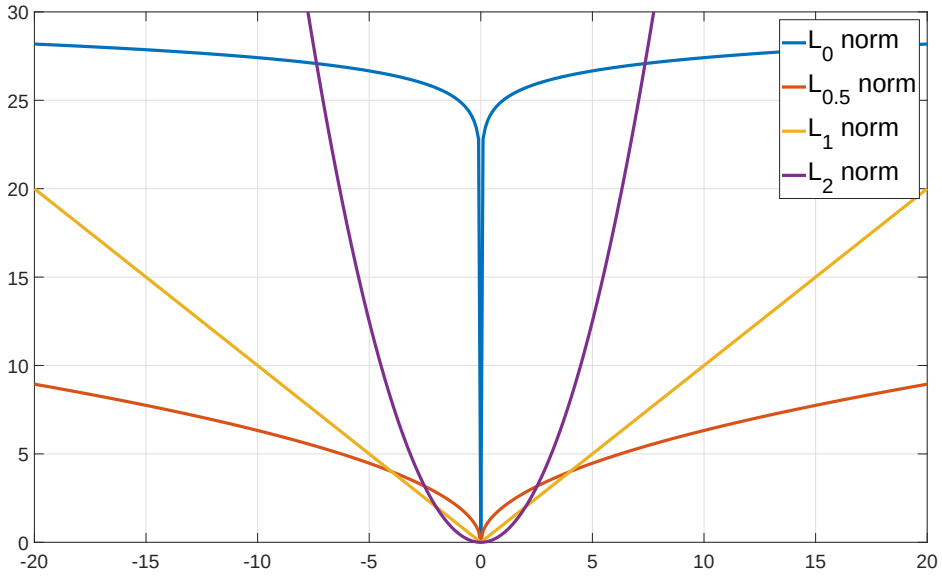

Figure 3.9: Undersampling in the number of views can cause significant aliasing in CT reconstruction. When 720 views per rotation is sampled, the reconstruction shows superior image quality with the filtered backprojection algorithm. As the sampling rate decreases to 8 views per rotation, strong aliasing artifacts completely damage the image quality.

Intuitively, the rationale behind favoring L_1-norm minimization over L_2-norm is that the penalty imposed upon the cost function should focus only on the number of the non-zeros coefficients instead of their values. For example, a large non-zero coefficient should have equal weight as a small coefficient as long as their sparse representations have identical numbers of non-zero coefficients. It is worth mentioning that in Figure 3.9, the L_1-norm, unlike the L_2-norm, is not differentiable at the origin. Therefore, it is originally not suited for a gradient-based optimization algorithm. To cope with this, an additional parameter is inserted into the iterative equation to avoid any abrupt transitions in the penalty function[47]. In general, minimization of L_1-norm offers the following two advantages:

- Minimizing the L_1-norm norm of a solution promotes sparsity.

- The L_1-norm can be minimized by computationally efficient algorithms.

Wavelet transform and gradient transform are two ideal sparse representations of a signal as they exhibit the aforementioned mathematical properties. The L_1-norm-based wavelet prior is defined as

$$\|f\|_{wave} = \int_{\Omega} \|w(x)\|_1 \, dx \tag{3.24}$$

where $w(x)$ is a wavelet coefficient as a function of location x, and Ω is the support of the entire image domain. This prior vector contains wavelet coefficients that result from an L_1-norm optimization. Similarly, the L_1-norm of gradient transform, or total variation, is defined in Equation 3.16 .

3.2.4 MRI Sampling Incoherence and Sparse View CT

When a signal is undersampled, the different sampling patterns lead to different reconstruction results, even for the same number of samplings. Designing a sampling pattern in some sense is equivalent to maximizing the sampling efficiency, which leads to an optimal reconstruction quality with minimal number of samples. In reality, due to system and hardware restriction, sampling strategies are usually based on a regular and even pattern. For example, an analog signal is sampled with a fixed sampling period T, and a uniform Fourier transform can later be applied for further analysis. However, such sampling schemes normally require a sufficient number of samples so that the Shannon-Nyquist sampling criterion is guaranteed. In compressed sensing, on the other hand, the sampling rate is far below the Nyquist rate. Therefore, the motivation behind random sampling becomes spontaneous, since a regular sampling scheme can no longer give sufficient information for signal recovery when canonical

methods are applied. The intuition behind random sampling is demonstrated using an 1-D example depicted in Figure 3.10.

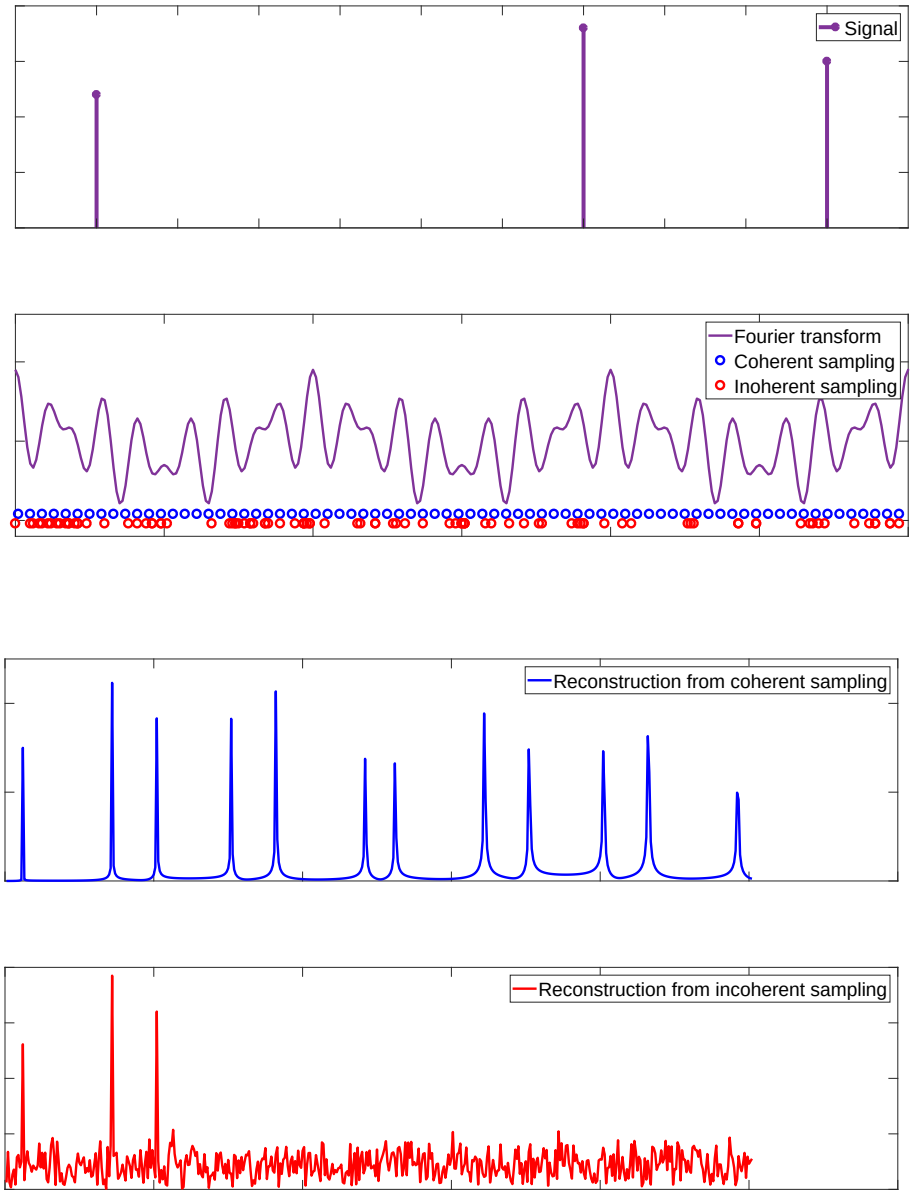

Figure 3.10: Signal recovery with incoherent sampling against coherent sampling. Top panel: original signal; Second panel: the Fourier spectrum of top panel being sampled with coherent sampling (blue circles) and incoherent sampling (red circles) with same number of samples; Third panel: inverse Fourier transform of coherent sampling leads to aliasing; Bottom panel: incoherent sampling leads to noise but aliasing is avoided.

The top panel in Figure 3.10 shows the original 1-D signal that consists of only three peaks. The Fourier transform of these peaks gives a waveform, displayed in the second panel, resulting from the summation of three sinusoidal functions. These three sinusoidal functions are the Fourier transform of the original three peaks. The waveform then is sampled with a regular pattern and a random pattern, respectively. Note that the number of samples are the same for both regular sampling and random sampling. Finally by applying inverse Fourier transform, the original signal is recovered. The third panel in Figure 3.10 clearly shows aliasing when a regular patterned sampling strategy is adopted. In contrast, the signal can definitively be distinguished in the fourth panel although noise is present in the background, as displayed in bottom panel. It should be pointed out that the background noise in fourth panel will eventually be minimized using denoising techniques in later stages, which will be explained in Section 3.2.5.

Although the idea of random sampling is natural and straightforward, a completely random sampling pattern is generally not realistic. Any practical sampling trajectory must comply with constraints set by the hardware and software. Therefore sampling trajectories usually avoid abrupt transients and follow relatively smooth curves. In addition, a good sampling pattern should always maximize the sampling efficiency, which means it should offer the best image quality with minimal amount of sampling. In this sense, a uniformly distributed undersampling pattern in k-space is not a good choice because it does not consider the energy distribution in Fourier space. As a matter of fact, the majority of the energy in an image is concentrated in the low frequency portion of the Fourier spectrum. Therefore, a good design for sampling in k-space should have a density profile with more samplings near the central portion of k-space. Such designs should also construct k-space trajectories that partially simulate the 2-D Gaussian pattern [69] of sampling.

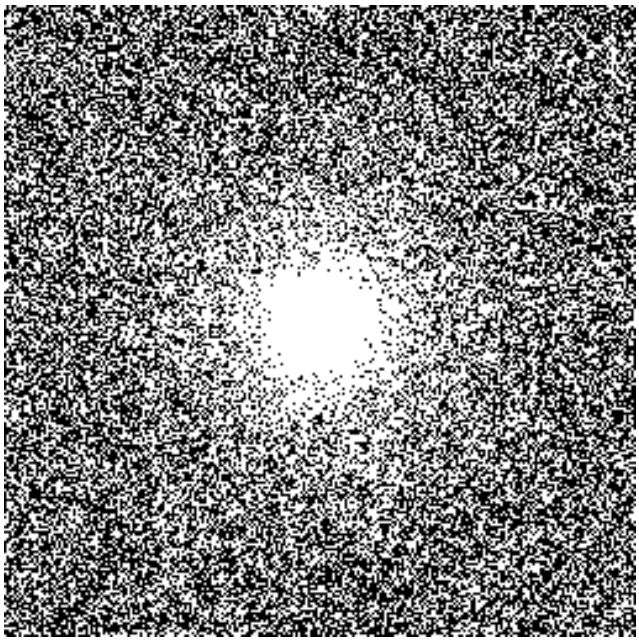

Figure 3.11: 50% undersampled k-space using Gaussian random sampling pattern [10].

On the other hand, unlike MRI, sampling in CT normally follows a well structured manner so a reasonable consideration is whether the randomness in sampling strategy could guarantee recoverability compared to regular sampling. Contrary to what might have been anticipated, taking randomized CT measurements does not generate any performance improvement in contrast to structured sampling patterns [85]. Specifically, random sampling in CT imaging can be done in two obvious ways: random sampling in view angle β and random sampling in fan angle γ. According to Jrgensen and Sidky [85], it is observed that there is essentially no difference in employing random sampling in either view angle or in a fan angle. In other words, in few view CT, randomness does not lead to improved recoverability compared to regular sampling patterns.

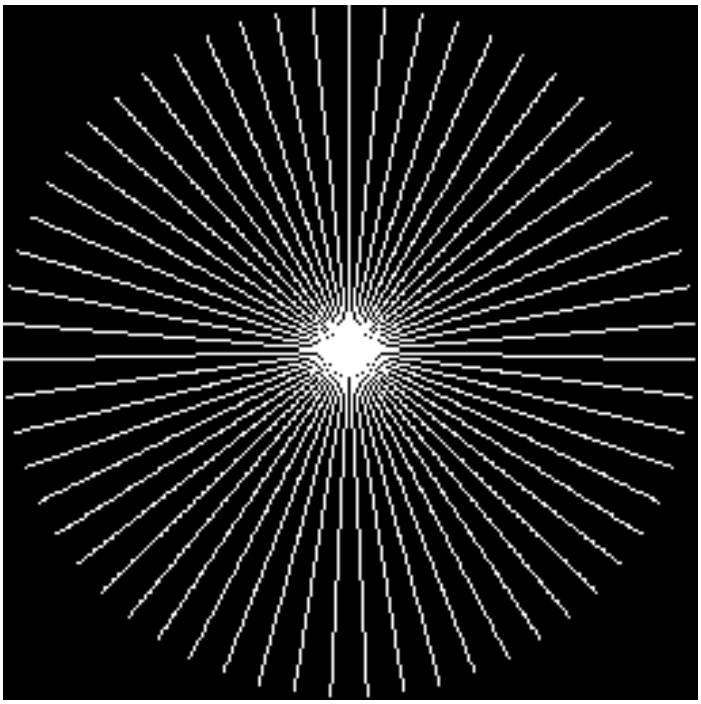

Figure 3.12: Sparse-view CT whose sampling consists of 59 projections that are evenly spaced out thorough the entire circle.

3.2.5 Optimization Algorithms

As discussed in Section 3.2.3, compressed sensing with a random sampling strategy has the potential to recover an original MRI image even when the data are highly undersampled. In particular, Figure 3.10 shows that compressed sensing essentially turns an ill-conditioned problem into a sparse signal denoising problem.

To remove the background noise in the fourth panel in Figure 3.10, optimization strategies are available for L_1-norm minimization. Among them there are soft thresholding algorithms, projection onto convex sets (POCS)-type algorithms, as well as gradient-based algorithms

such as a non-linear conjugate gradient.

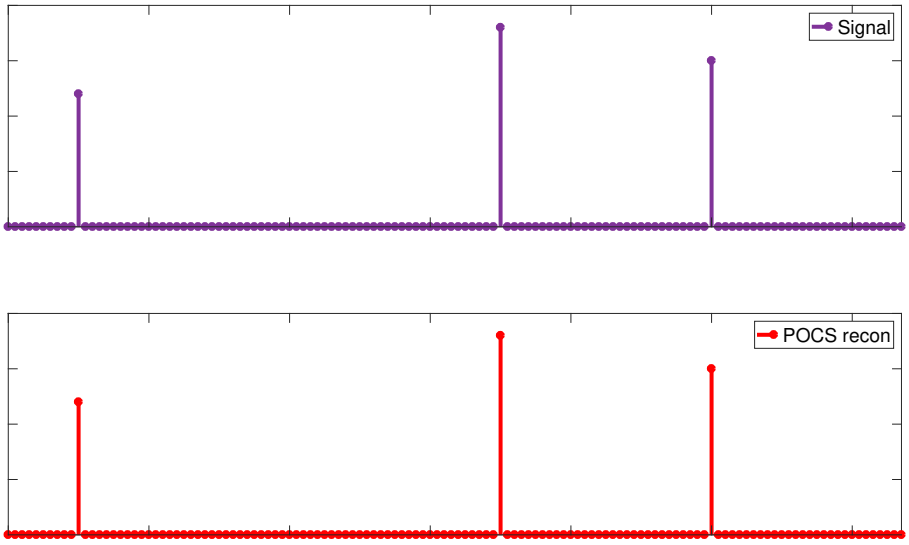

Figure 3.13: Signal reconstruction using POCS optimization. Top: original signal in Figure 3.10 displayed in the top panel; Bottom: signal reconstruction using POCS-type algorithm that removes all background noise in the bottom panel in Figure 3.10 .

Figure 3.13 is an example of using a POCS-type algorithm [86] to recover the signal in Figure 3.10 after inverse fast Fourier transform is applied to the randomly sampled signals. As the figure shows, the POCS iterative method completely removes the noise from the sparse signal.

The nonlinear conjugate gradient method, on the other hand, is a generalized conjugate gradient method for nonlinear optimization. In optimization theory, the nonlinear conjugate gradient method solves for the local extrema of an objective function by using a gradient of the objective function alone. It handles functions that are approximately quadratic near the extrema. In addition, line search algorithms that satisfiy Wolfe conditions [87, 88] are often required to find an optimal stepsize. The nonlinear conjugate gradient will be further discussed in Chapter 4.

3.2.6 Models of Linear Mapping

One of the core components in iterative reconstruction is the linear mapping model A defined in Equation 2.6. The linear projector A maps an image to its transformed domain. As discussed in Chapter 2, the linear mapping in MRIs is a Fourier transform. The Fourier transform for echo planar imaging is Cartesian-based. Other k-space-sampling trajectories, for instance radial or spiral, need further post processing such as regridding and interpolation. This is depicted in Figure 2.9. In general, the forward mapping operation for MRI is Fourier transform, defined in Equation 3.9, and the backward mapping is the inverse Fourier transform defined in Equation 3.10. Note that the inverse Fourier transform is the Hermitian adjoint [62] operation of Fourier transform.

Nonetheless, the linear mapping model of CT imaging is more complex due to the continuous distribution of an X-ray spray. As discussed in Chapter 2, X-ray CT measurements are governed by Beers law, and the projection values p are computed by a Radon transform or projection described in Equation 2.1 and Equation 2.2. Figure 2.2 depicts the continuous case, whereas its digitized version has a few popular approaches for computing the projection p value. The key is to find the best tradeoff between accuracy and computational efficiency [89].

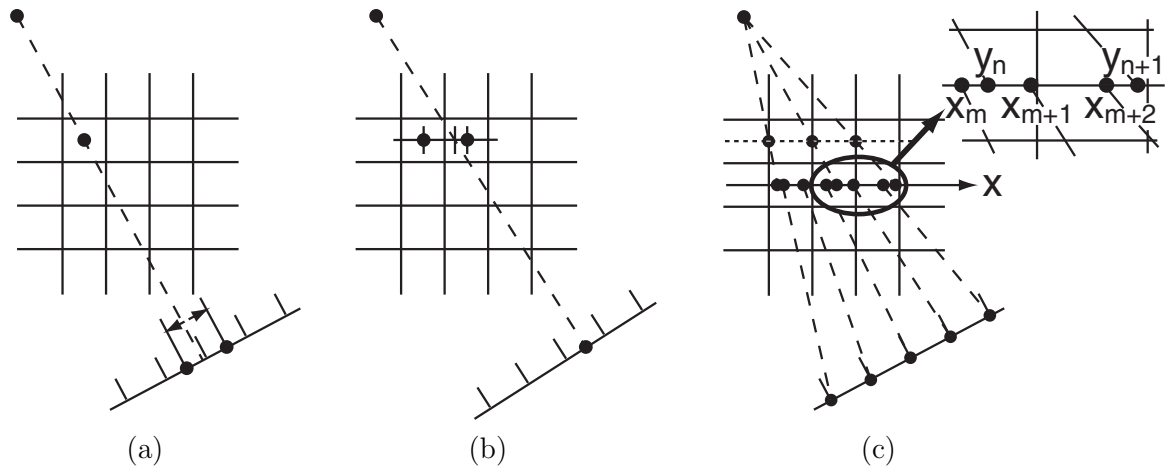

Figure 3.14: Common X-ray projection and backprojection models: (a) Pixel-driven model that works by projecting a X-ray beam from the source through the center of the pixel of interest to the detector. (b) Ray-driven model which works by projecting an X-ray beam from the source through the image to the center of the detector channel of interest. (c) Distance-driven model which works by mapping the boundaries of each pixel and detector cell onto a common axis; the length of the overlap is used as common weighting coefficients for both projections and backprojections [11].

Three common projection models, (from left to right) pixel-driven, ray-driven, and distance-driven, are shown in Figure 3.14 [11]. In general, distance-driven techniques can eliminate artifacts seen in ray-driven backprojections and in pixel-driven projections. This is because it employs an identical physics model by projecting and backprojecting image information from an image voxel or detector channel onto a common axis, thereby avoiding the mismatch between forward and backward operations. This particular feature makes distance-driven methods extremely preferred over pixel-driven or ray-driven in iterative-based methods [90, 11, 89]. Compared to pixel-driven and ray-driven methods, the distance-driven method restricts the error from being amplified, and therefore it minimizes the discrepancy between mapping models.

3.3 Summary

The minimum sampling rate is governed by the Shannon-Nyquist sampling theorem, so undersampled data sets can generate strong aliasing in final images if reconstructed by analytical methods.

Unlike analytical methods, compressed sensing can minimize the aliasing of the undersampled data sets by iteratively solving for the unknown signal. It requires sparse representation of the unknown signal as additional information to perform reconstruction. The sparse representation of a signal is not unique. For example, gradient transform and wavelet transform can both map a signal into a sparse domain.

Mathematically, the compressed sensing problem is formulated as an optimization problem, which can be solved by maximizing the sparsity of the signal. Regularization such as L_1-norm has been proven effective in sparsity maximization. Compressed sensing theory provides a feasible solution to reconstruct undersampled medical image data. In Chapter 4, we will further explain undersampled CT and MRI image reconstruction using compressed sensing theory.

Chapter 4

JOINT CT-MRI IMAGE RECONSTRUCTION

As discussed in Chapter 1, multimodal imaging techniques have brought more comprehensive information into clinical decision processes. Inspired by this idea, using mutual information in the joint CT-MRI system to enhance reconstruction is spontaneous. The rationale is that the multimodal platform samples the same anatomy at the same time so the images must share structural similarities especially at boundaries and edges. This is achieved despite the fact that CT and MRI images are formed under completely different physical principles. In other words, CT images and MRI images are similar in structural features even though they look quite different in terms of pixel intensity and contrast for the same anatomy. As a result, coupling of structural features between CT and MRI can potentially improve reconstruction quality for both of them. From a signal processing perspective, this is equivalent to utilizing more information to perform better signal recovery.

In this chapter we will describe the novel joint reconstruction framework in detail. The proposed method employs a sparse-prior-based projection distance optimization, and updates

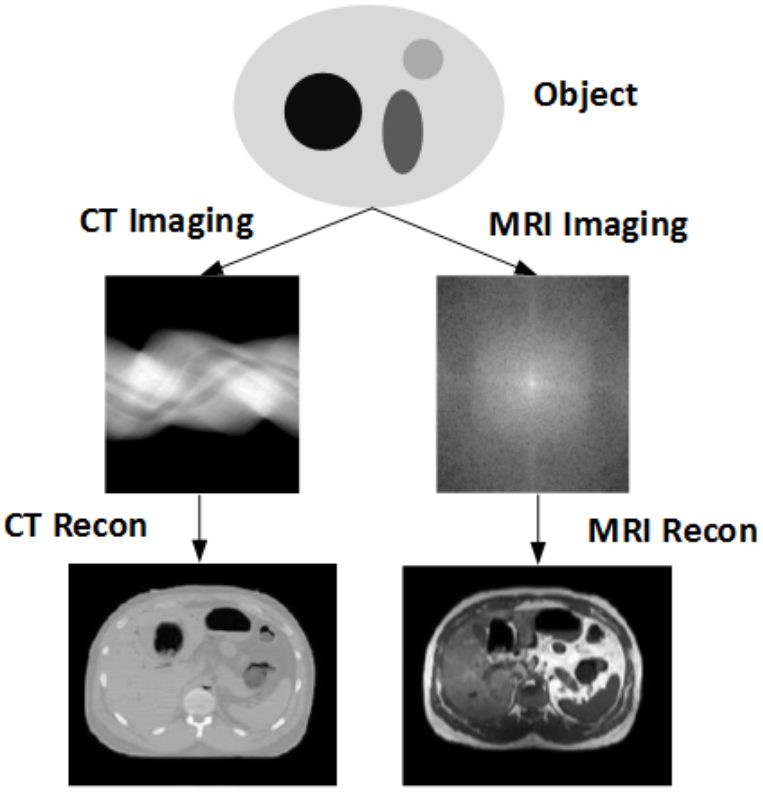

Figure 4.1: Imaging pipeline on a fused CT-MRI system. The CT and MRI signals are independently collected from same anatomy.

images at each iteration. The methodology is very general and can be extended to any imaging problem that shares structural similarities. For comparison purposes, analytical reconstruction and individual compressed sensing-based reconstructions are also implemented. The latter method does not utilize any information from the other modality and thereby ignores similarities and correlated information. Since the omni-tomography has not yet been realized, our data are generated by simulation using clinical CT and MRI images.

4.1 Structural Similarities

Structural similarity is an indicator of shared resemblance between images. Since the CT and MRI images are acquired from the same anatomy in this work, the structural similarities must reside in the cross-platform imaging systems. In particular, the structural similarity between two modalities shows its strongest intensity at edges and boundaries.

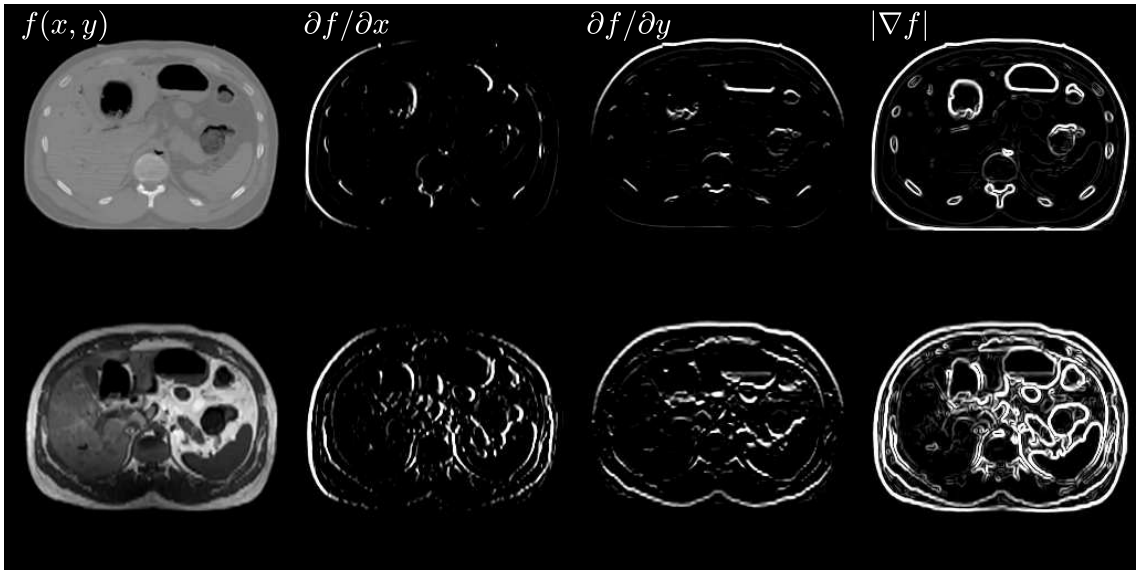

Figure 4.2: Gradient transform of an abdomen image with CT on top row and MRI on bottom row. From left to right: original image, gradient in x direction, gradient in y direction, and gradient norm.

Figure 4.2 shows the gradient transform of an abdomen CT image (top row) and an MRI image (bottom row) using a stencil-based high-order approximation [47]. Similarly, Figure 4.3 presents a pair of head images with their gradient images displayed. It can be observed from both figures that images appear more correlated and similar when displayed in their gradient mode than their natural mode. If the anatomy is the same, the information from

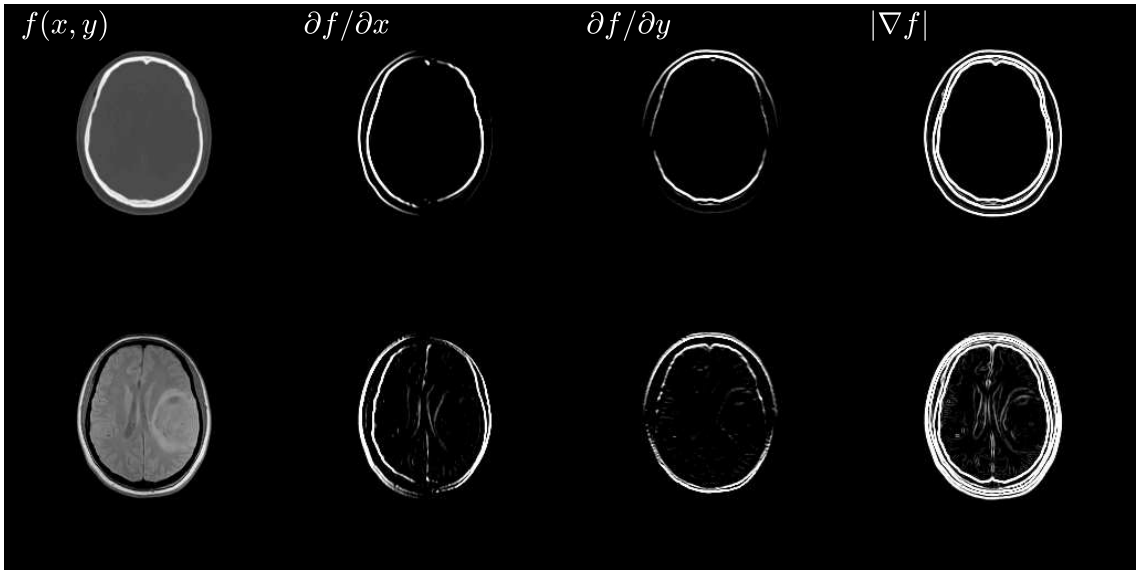

Figure 4.3: Gradient transform of an head image with CT on top row and MRI on bottom row. From left to right: original image, gradient in x direction, gradient in y direction, and gradient norm.

edges and boundaries are similar.

To measure similarity improvements when images are displayed in their gradient, a Structural SImilarity Measurement (SSIM) [91] measurement is employed to perform a quantified analysis. Table 4.1 lists a comparison of SSIM between a CT and an MRI image pair across the original image and their gradients. The structural similarity is increased when comparing image gradients instead of the original images. In addition, head images show stronger

Table 4.1: Structural Similarity Comparison Between Object and Gradient

Similarity	Anatomy	$f(x,y)$	$\partial f/\partial x$	$\partial f/\partial y$	$\|\nabla f\|$
SSIM(CT, MRI)	Abdomen	0.3758	0.7213	0.7065	0.7245
	Head	0.4327	0.8077	0.8106	0.8257

similarities across different modalities than the abdominal images. This suggests that using information from edges and boundaries can potentially improve image recovery more than using the information from original images.

4.2 Multichannel Imaging Reconstruction

In Chapter 2, it is shown that both CT and MRI imaging systems can be described as a linear shift-invariant regression model defined in Equation 2.6. The system matrix $\mathbf{A}$ in Equation (2.6) indicates forward projection in CT imaging and Fourier transform in MRI.

As CT and MRI are fused together, the multimodal imaging system is modeled as an M-channeled imaging system [92, 47] whose system matrix is

$$\mathbf{A} = \begin{bmatrix} \mathbf{A}_{11} & \mathbf{A}_{12} & \dots & \mathbf{A}_{1M} \\ \mathbf{A}_{21} & \mathbf{A}_{22} & \dots & \mathbf{A}_{2M} \\ \vdots & \vdots & \ddots & \vdots \\ \mathbf{A}_{M1} & \mathbf{A}_{M2} & \dots & \mathbf{A}_{MM} \end{bmatrix}. \tag{4.1}$$

The diagonal terms in Equation (4.1) represent the within channel impulse responses, whereas the off-diagonal terms represent the cross-channel interactions. An important fact for the joint system is that CT and MRI imaging are acquired independently within the fused platform. This is also described in Figure 4.1 that CT and MRI sampling procedures do not interfere with each other. As a result, this implies that all the off-diagonal elements are 0, which leads to the simplification where

$$\mathbf{A} = \begin{bmatrix} \mathbf{A}_1 & 0 \\ 0 & \mathbf{A}_2 \end{bmatrix}. \tag{4.2}$$

Similarly, for multichanneled data, signal, and noise, we have

$$\mathbf{y} = \begin{bmatrix} \mathbf{y}_1 \\ \mathbf{y}_2 \end{bmatrix}, \mathbf{x} = \begin{bmatrix} \mathbf{x}_1 \\ \mathbf{x}_2 \end{bmatrix}, \text{and } \sigma = \begin{bmatrix} \sigma_1 \\ \sigma_2 \end{bmatrix}, \tag{4.3}$$

where the subscripts "1" and "2" indicate CT and MRI, respectively. This notation carries on throughout the rest of the paper.

The regression model given by Equation 2.6 is known to be ill-conditioned and encompasses a large variance in noise. According to the compressed sensing theory, solving such a problem requires sparse representation of the unknown signal as an additional regularization term [29, 31, 28]. Here, total variation is employed because it has shown impressive results in many applications. The total variation of an image $\mathbf{x}$ is defined in Equation 3.16. By extending it, the total variation for a multichannel imaging system $TV_M(\mathbf{x})$ is defined as [92, 47]

$$TV_M(\mathbf{x}) = \sqrt{\sum_{m=1}^{M} TV(\mathbf{x}_m)^2}, \tag{4.4}$$

where M denotes the total number of the channels in the multichannel imaging system and m denotes the channel index. As a multichannel imaging system, the multimodal reconstruction framework is formulated as a constrained optimization problem defined as

$$\begin{aligned} \mathbf{x} &= \arg\min_{\mathbf{x}} \Big(TV_M(\mathbf{x}) \Big), \\ s.t. \qquad & \mathbf{y} = \mathbf{A}\mathbf{x}, \end{aligned} \tag{4.5}$$

which can be solved by minimizing a cost function expressed as

$$f(\mathbf{x}) = \frac{1}{2}\eta \|\mathbf{A}\mathbf{x} - \mathbf{y}\|_2^2 + \xi TV_M(\mathbf{x}), \tag{4.6}$$

where $\|\cdot\|_2$ denotes the L_2-norm defined as

$$\|x\|_2 = (x_1^2 + x_2^2 + \cdots + x_n^2)^{\frac{1}{2}}, \tag{4.7}$$

and ξ is a constant parameter. Note Equation (4.6) is a typical Lagrange function consisting of a data fidelity term and a regularization term. In fact, since there are two modalities in our CT-MRI system, the cost function given by Equation (4.6) needs to be adjusted such that

$$f(\mathbf{x}_1, \mathbf{x}_2) = \frac{1}{2}\eta_1\|\mathbf{A}_1\mathbf{x}_1 - \mathbf{y}_1\|_2^2 + \frac{1}{2}\eta_2\|\mathbf{A}_2\mathbf{x}_2 - \mathbf{y}_2\|_2^2 + \xi\sqrt{TV(\mathbf{x}_1)^2 + TV(\mathbf{x}_2)^2}, \tag{4.8}$$

where $\mathbf{x}_1$ is the CT image and $\mathbf{x}_2$ is the MRI image. η_1, η_2, ξ_1, and ξ_1 are tuning parameters reflecting each channel gain.

A common way to minimize $f(\mathbf{x})$ in Equation (4.6) is to adopt gradient-based methods. By applying the chain rule, the partial derivative of the multimodaled TV in Equation (4.6) with respect to (w.r.t.) the mth modality is given by

$$\frac{\partial TV_M(\mathbf{x})}{\partial \mathbf{x}_m} = \frac{TV(\mathbf{x}_m)}{TV_M(\mathbf{x})}\nabla \cdot \left(\frac{\nabla \mathbf{x}_m}{\|\nabla \mathbf{x}_m\|_2}\right). \tag{4.9}$$

Hence, the partial derivative of the cost function given by (4.6) w.r.t. the unknown of one single modality is expressed as

$$\frac{\partial f(\mathbf{x})}{\partial \mathbf{x}_m} = \mathbf{A}_m^*\big(\mathbf{A}_m\mathbf{x}_m - \mathbf{y}_m\big) + \xi\frac{TV(\mathbf{x}_m)}{TV_M(\mathbf{x})}\nabla \cdot \left(\frac{\nabla \mathbf{x}_m}{\|\nabla \mathbf{x}_m\|_2}\right), \tag{4.10}$$

where $\mathbf{A}_m^*$ is the conjugate transpose of $\mathbf{A}$.

4.3 Multimodal Coupling

The purpose of jointly reconstructing multimodal images is to enhance image quality by incorporating additional information such as structural similarities. The design seeks to utilize commonly shared features between CT and MRI images. Although these images have different dynamic ranges and distributions, they share strong similarities and correlation especially at the edges and boundaries, which are shown in Figure 4.2, Figure 4.3, and Table 4.1. Figure 4.4 shows the overlapped image gradients between CT and MRI images. Starting from perfect alignment on the upper left corner, the MRI image rotates such that the inter-vector angle increments by 22.5°. As the inter-vector angle increases, the overlap between the two decreases, and so does the similarity between the CT and MRI images.

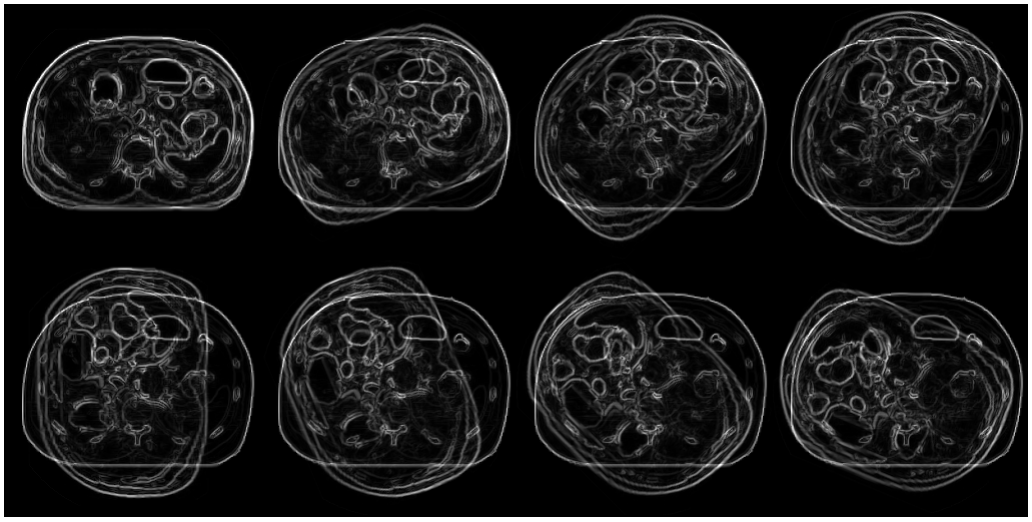

Figure 4.4: Angle between overlaid CT and MRI image gradients varying from 0°to 160°; note that when the angle is 0°, the two images are very well aligned.

To incorporate the structural similarities of CT and MRI images, one needs to measure the divergence between the two images in a feature space. To this end, we introduce a projection distance between the TVs of two images as a quantitative metric. Specifically, given two vectors $\mathbf{u}$ and $\mathbf{v}$, the projection distance $d_{proj}(\mathbf{u}, \mathbf{v})$ is defined as

$$d_{proj}(\mathbf{u},\mathbf{v}) = 1 - \cos(\mathbf{u},\mathbf{v}) = 1 - \frac{\mathbf{u}\cdot\mathbf{v}}{\|\mathbf{u}\|_2\|\mathbf{v}\|_2}, \tag{4.11}$$

where $\cos(\mathbf{u},\mathbf{v})$ is the cosine similarity, and $\mathbf{u}\cdot\mathbf{v}$ is the inner product of $\mathbf{u}$ and $\mathbf{v}$. The projection distance measures the dissimilarity between two non-zero vectors of an inner product space by computing the cosine of the angle between them. Consequently, it becomes larger as the two images become less similar, and it becomes smaller as they become more alike. Figure 4.5 shows how the projection distance changes as a function of the deviation changing between the two vectors. The function curve is approximated by an $8th$ order polynomial function given by

$$p(x) = \sum_{n=0}^{8} (a_n x^n). \tag{4.12}$$

Note that $1 \geqslant d_{proj}(\mathbf{u},\mathbf{v}) \geqslant 0$ and $d_{proj}(\mathbf{u},\mathbf{v}) = d_{proj}(\mathbf{v},\mathbf{u})$. It is also straightforward to prove that $d_{proj}(\mathbf{u},\mathbf{v}) = 0$ when two vectors are identical, and $d_{proj}(\mathbf{u},\mathbf{v}) = 1$ when two vectors are orthogonal.

In order to embed the projection distance into our gradient-based optimization framework, its derivative w.r.t. the TV of the unknown images is necessary. Here we only show the derivation w.r.t. one of the modalities, and the other simply follows the symmetric principle. By definition, the derivative of $d_{proj}(\mathbf{u},\mathbf{v})$ w.r.t. $\mathbf{u}$ is given by

$$\frac{\partial}{\partial\mathbf{u}} d_{proj}(\mathbf{u},\mathbf{v}) = -\frac{\partial}{\partial\mathbf{u}} cos(\mathbf{u},\mathbf{v}),$$

where

$$\frac{\partial}{\partial\mathbf{u}} cos(\mathbf{u},\mathbf{v}) = \lim_{\partial\mathbf{u}\to 0} \frac{cos(\mathbf{u}+\partial\mathbf{u},\mathbf{v}) - cos(\mathbf{u},\mathbf{v})}{\partial\mathbf{u}},$$

and

$$cos(\mathbf{u}+\partial\mathbf{u},\mathbf{v}) = \frac{(\mathbf{u}+\partial\mathbf{u})\cdot\mathbf{v}}{\|\mathbf{u}+\partial\mathbf{u}\|_2\|\mathbf{v}\|_2}.$$

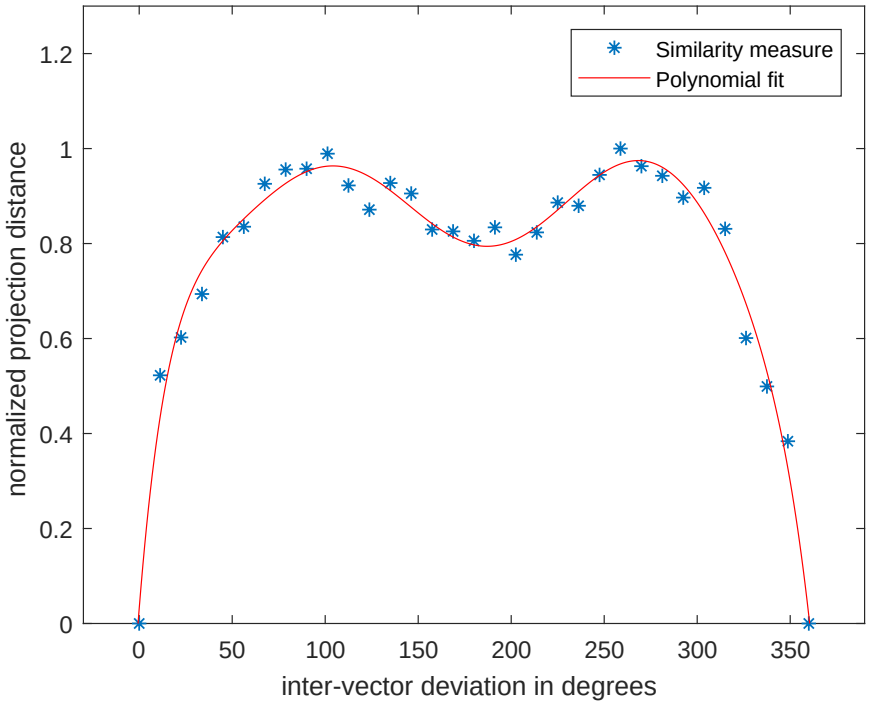

Figure 4.5: Fitting curve defined in Equation (4.12) shows projection distance as a function of the angle between CT and MRI image TVs; note that it reaches its maximum when the two images are orthogonal and its minimum when the two images are perfectly aligned.

Particularly, we have

$$\begin{aligned}\|\mathbf{u}+\partial\mathbf{u}\|_2 &= \sqrt{(\mathbf{u}+\partial\mathbf{u})\cdot(\mathbf{u}+\partial\mathbf{u})} \\ &= \|\mathbf{u}\|_2\sqrt{1+2\frac{\mathbf{u}}{\|\mathbf{u}\|_2^2}\cdot\partial\mathbf{u}+\frac{\|\partial\mathbf{u}\|_2^2}{\|\mathbf{u}\|_2^2}}\ . \\ &\approx \|\mathbf{u}\|_2\left(1+\frac{\mathbf{u}}{\|\mathbf{u}\|_2^2}\cdot\partial\mathbf{u}\right)\end{aligned}$$

It follows that

$$cos(\mathbf{u}+\partial\mathbf{u},\mathbf{v}) \approx \frac{\mathbf{u}\cdot\mathbf{v}+\partial\mathbf{u}\cdot\mathbf{v}}{\|\mathbf{u}\|_2\left(1+\frac{\mathbf{u}}{\|\mathbf{u}\|_2^2}\cdot\partial\mathbf{u}\right)\|\mathbf{v}\|_2}$$

$$
\begin{aligned}
&\approx \frac{\mathbf{u}\cdot\mathbf{v}+\partial\mathbf{u}\cdot\mathbf{v}}{\|\mathbf{u}\|_2\,\|\mathbf{v}\|_2}\left(1-\frac{\mathbf{u}}{\|\mathbf{u}\|_2^2}\cdot\partial\mathbf{u}\right)\\
&=\left(\frac{\mathbf{u}}{\|\mathbf{u}\|_2\,\|\mathbf{v}\|_2}-\frac{\mathbf{u}\cdot\mathbf{v}}{\|\mathbf{u}\|_2\,\|\mathbf{v}\|_2}\frac{\mathbf{u}}{\|\mathbf{u}\|_2^2}\right)\cdot\partial\mathbf{u}\\
&+\frac{\mathbf{u}\cdot\mathbf{v}}{\|\mathbf{u}\|_2\,\|\mathbf{v}\|_2}+O(\partial\mathbf{u}^2)\\
&\approx \cos(\mathbf{u},\mathbf{v})+\left(\frac{\mathbf{v}}{\|\mathbf{u}\|_2\,\|\mathbf{v}\|_2}-\cos(\mathbf{u},\mathbf{v})\frac{\mathbf{u}}{\|\mathbf{u}\|_2^2}\right)\cdot\partial\mathbf{u},
\end{aligned}
$$

and

$$
\frac{\partial}{\partial\mathbf{u}}cos(\mathbf{u},\mathbf{v})=\lim_{\partial\mathbf{u}\to 0}\frac{cos(\mathbf{u}+\partial\mathbf{u},\mathbf{v})-cos(\mathbf{u},\mathbf{v})}{\partial\mathbf{u}}=\frac{\mathbf{v}}{\|\mathbf{u}\|_2\,\|\mathbf{v}\|_2}-\cos(\mathbf{u},\mathbf{v})\frac{\mathbf{u}}{\|\mathbf{u}\|_2^2}.
$$

Hence,

$$
\frac{\partial}{\partial\mathbf{u}}d_{proj}(\mathbf{u},\mathbf{v})=\cos(\mathbf{u},\mathbf{v})\frac{\mathbf{u}}{\|\mathbf{u}\|_2^2}-\frac{\mathbf{v}}{\|\mathbf{u}\|_2\,\|\mathbf{v}\|_2}. \tag{4.13}
$$

Similarly, due to the symmetric form of projection distance, its derivative w.r.t. $\mathbf{v}$ is given by

$$
\frac{\partial}{\partial\mathbf{v}}d_{proj}(\mathbf{u},\mathbf{v})=\cos(\mathbf{u},\mathbf{v})\frac{\mathbf{v}}{\|\mathbf{v}\|_2^2}-\frac{\mathbf{u}}{\|\mathbf{u}\|_2\,\|\mathbf{v}\|_2}. \tag{4.14}
$$

Note that in our optimization framework $\mathbf{u}$ and $\mathbf{v}$ here are TV terms of the CT and the MRI image, therefore, by applying chain rule we have

$$
\frac{\partial}{\partial\mathbf{x}_1}d_{proj}(\mathbf{u},\mathbf{v})=\left(\cos(\mathbf{u},\mathbf{v})\frac{\mathbf{u}}{\|\mathbf{u}\|_2^2}-\frac{\mathbf{v}}{\|\mathbf{u}\|_2\,\|\mathbf{v}\|_2}\right)\nabla\cdot\left(\frac{\nabla\mathbf{x}_1}{\|\nabla\mathbf{x}_1\|_2}\right) \tag{4.15}
$$

for CT imaging, and

$$
\frac{\partial}{\partial\mathbf{x}_2}d_{proj}(\mathbf{u},\mathbf{v})=\left(\cos(\mathbf{u},\mathbf{v})\frac{\mathbf{v}}{\|\mathbf{v}\|_2^2}-\frac{\mathbf{u}}{\|\mathbf{u}\|_2\,\|\mathbf{v}\|_2}\right)\nabla\cdot\left(\frac{\nabla\mathbf{x}_2}{\|\nabla\mathbf{x}_2\|_2}\right) \tag{4.16}
$$

for MRI. In Equation (4.15) and Equation (4.16), $\mathbf{u}=TV(\mathbf{x}_1)$ and $\mathbf{v}=TV(\mathbf{x}_2)$.

4.4 Optimization

To restrict the divergence between CT and MRI images, the projection distance is added to Equation (4.6). The cost function thereby becomes

$$f(\mathbf{x}) = \frac{1}{2}\eta\|\mathbf{A}\mathbf{x} - \mathbf{y}\|_2^2 + \xi TV_M(\mathbf{x}) + \lambda d_{proj}(TV(\mathbf{x})), \tag{4.17}$$

where λ is the tuning factor for the projection distance term. By expressing Equation (4.17) as a cost function of a joint CT-MRI optimization, we get

$$\begin{aligned} f(\mathbf{x}_1, \mathbf{x}_2) &= \frac{1}{2}\eta_1\|\mathbf{A}_1\mathbf{x}_1 - \mathbf{y}_1\|_2^2 + \frac{1}{2}\eta_2\|\mathbf{A}_2\mathbf{x}_2 - \mathbf{y}_2\|_2^2 \\ &+ \xi\sqrt{TV(\mathbf{x}_1)^2 + TV(\mathbf{x}_2)^2} \\ &+ \lambda d_{proj}\big(TV(\mathbf{x}_1), TV(\mathbf{x}_2)\big), \end{aligned} \tag{4.18}$$

where $d_{proj}\big(TV(\mathbf{x}_1), TV(\mathbf{x}_2)\big)$ is the projection distance of TVs of the CT and the MRI images, and it is defined in Equation (4.11).

To solve $\mathbf{x}_1$ and $\mathbf{x}_2$ in Equation (4.18), we generalize the conjugate gradient method to a nonlinear optimization problem. The nonlinear conjugate gradient (NCG) method [93, 94, 95, 96, 47] only requires the gradient of the cost function to seek a local minimum of a quadratic function in the neighborhood of the critical points. By taking the derivatives on both sides of Equation (4.18) and letting $\mathbf{u} = TV(\mathbf{x}_1)$ and $\mathbf{v} = TV(\mathbf{x}_2)$, the gradient of

$f(\mathbf{x}_1, \mathbf{x}_2)$ in Equation (4.18) w.r.t. $\mathbf{x}_1$ is

$$\begin{aligned}\frac{\partial f(\mathbf{x}_1, \mathbf{x}_2)}{\partial \mathbf{x}_1} &= \eta \mathbf{A}_1^*\big(\mathbf{A}_1\mathbf{x}_1 - \mathbf{y}_1\big) \\ &+ \xi \frac{\mathbf{u}}{TV_M(\mathbf{x})} \nabla \cdot \left(\frac{\nabla \mathbf{x}_1}{\|\nabla \mathbf{x}_1\|_2} \right) \\ &+ \lambda \left(\cos(\mathbf{u}, \mathbf{v}) \frac{\mathbf{u}}{\|\mathbf{u}\|_2^2} - \frac{\mathbf{u}}{\|\mathbf{u}\|_2 \, \|\mathbf{v}\|_2} \right) \nabla \cdot \left(\frac{\nabla \mathbf{x}_1}{\|\nabla \mathbf{x}_1\|_2} \right),\end{aligned} \tag{4.19}$$

and the counterpart w.r.t. $\mathbf{x}_2$ is

$$\begin{aligned}\frac{\partial f(\mathbf{x}_1, \mathbf{x}_2)}{\partial \mathbf{x}_2} &= \eta \mathbf{A}_2^*\big(\mathbf{A}_2\mathbf{x}_2 - \mathbf{y}_2\big) \\ &+ \xi \frac{\mathbf{v}}{TV_M(\mathbf{x})} \nabla \cdot \left(\frac{\nabla \mathbf{x}_2}{\|\nabla \mathbf{x}_2\|_2} \right) \\ &+ \lambda \left(\cos(\mathbf{u}, \mathbf{v}) \frac{\mathbf{v}}{\|\mathbf{v}\|_2^2} - \frac{\mathbf{v}}{\|\mathbf{u}\|_2 \, \|\mathbf{v}\|_2} \right) \nabla \cdot \left(\frac{\nabla \mathbf{x}_2}{\|\nabla \mathbf{x}_2\|_2} \right),\end{aligned} \tag{4.20}$$

where

$$\cos(\mathbf{u}, \mathbf{v}) = \frac{\mathbf{u} \cdot \mathbf{v}}{\|\mathbf{u}\|_2 \, \|\mathbf{v}\|_2}. \tag{4.21}$$

Note that the derivative of projection distance is derived in Equation 4.15 and Equation 4.16 in Section 4.3.

In practical implementation, in order to make L_1-norm differentiable throughout its entire support, an infinitesimal term ϵ, e.g. 1×10^{-15}, is added such that

$$\nabla \cdot \left(\frac{\nabla \mathbf{x}_m}{\|\nabla \mathbf{x}_m\|_2} \right) \rightarrow \nabla \cdot \left(\frac{\nabla \mathbf{x}_m}{\|\nabla \mathbf{x}_m + \epsilon\|_2} \right). \tag{4.22}$$

The joint CT-MRI system essentially extends the NCG optimization problem to a multivariate level. To solve it, the updates of Algorithm 1 are calculated at each iteration. Here, the superscript n denotes the nth iteration; $\mathbf{d}^{(n)}$ denotes conjugate gradient; $\alpha^{(n)}$ denotes

step size found by the line search algorithm satisfying the Wolfe condition [87, 88]; $\beta^{(n)}$ is computed by the Fletcher-Reeves method [97]; and $\cdot$ depicts the dot product. The entire iterative algorithm is summarized in Algorithm 1. Note that in Algorithm 1, $\beta_1^{(n)}$ and $\beta_2^{(n)}$ are the same since the NCG method accounts for the union of $\mathbf{x}_1$ and $\mathbf{x}_2$ expressed as [$\mathbf{x}_1$, $\mathbf{x}_2$].

Algorithm 1 Compressed Sensing-based Joint Reconstruction.

Initialization:
$\mathbf{x}_1^{(0)} = 0; \mathbf{x}_2^{(0)} = 0;$
$\mathbf{d}_1^{(0)} = -\nabla_{\mathbf{x}_1} f(\mathbf{x}_1^{(0)}, \mathbf{x}_2^{(0)});$
$\mathbf{d}_2^{(0)} = -\nabla_{\mathbf{x}_2} f(\mathbf{x}_1^{(0)}, \mathbf{x}_2^{(0)});$
$k = 0;$
while *true* **do**
  Line search:
  $\alpha^{(n)} = \arg\min_\alpha f(\mathbf{x}_1^{(n)} + \alpha \mathbf{d}_1^{(n)}, \mathbf{x}_2^{(n)} + \alpha \mathbf{d}_2^{(n)}).$
  Update results
  $\mathbf{x}_1^{(n+1)} = \mathbf{x}_1^{(n)} + \alpha^{(n)} \mathbf{d}_1^{(n)};$
  $\mathbf{x}_2^{(n+1)} = \mathbf{x}_2^{(n)} + \alpha^{(n)} \mathbf{d}_2^{(n)};$
  Update steepest decent direction
  $\mathbf{g}_1^{(n+1)} = -\nabla_{\mathbf{x}_1} f(\mathbf{x}_1^{(n+1)}, \mathbf{x}_2^{(n+1)});$
  $\mathbf{g}_2^{(n+1)} = -\nabla_{\mathbf{x}_2} f(\mathbf{x}_1^{(n+1)}, \mathbf{x}_2^{(n+1)});$
  Update Fletcher-Reeves value
  $\mathbf{g}^{(n)} = [\mathbf{g}_1^{(n)}, \mathbf{g}_2^{(n)}];$
  $\beta_1^{(n)} = \frac{\mathbf{g}^{(n+1)} \cdot \mathbf{g}^{(n+1)}}{\mathbf{g}^{(n)} \cdot \mathbf{g}^{(n)}};$
  $\beta_2^{(n)} = \frac{\mathbf{g}^{(n+1)} \cdot \mathbf{g}^{(n+1)}}{\mathbf{g}^{(n)} \cdot \mathbf{g}^{(n)}};$
  Update conjugate gradient
  $\mathbf{d}_1^{(n+1)} = \mathbf{g}_1^{(n+1)} + \beta_1^{(n)} \mathbf{d}_1^{(n)};$
  $\mathbf{d}_2^{(n+1)} = \mathbf{g}_2^{(n+1)} + \beta_2^{(n)} \mathbf{d}_2^{(n)};$
  $k = k + 1;$
  if $k > K$ or $|d\mathbf{x}_1| < \epsilon_1$ or $|d\mathbf{x}_2| < \epsilon_2$ **then**
    break;
  end if
end while

4.5 Wavelet Sparse Prior

As previously mentioned in Chapter 3, wavelet transform is also a sparse transform besides gradient transform. Similar to Equation 4.18, an optimization framework built upon wavelet prior can be written as [48].

$$\begin{aligned} f(\mathbf{w}_1, \mathbf{w}_2) = &\frac{1}{2}\eta_1 \|\mathbf{A}_1\mathbf{W}^T\mathbf{w}_1 - \mathbf{y}_1\|_2^2 + \frac{1}{2}\eta_2 \|\mathbf{A}_2\mathbf{W}^T\mathbf{w}_2 - \mathbf{y}_2\|_2^2 \\ &+ \xi\Big(\|\mathbf{w}_1\|_1 + \|\mathbf{w}_2\|_1\Big) + \lambda d_{proj}\big(\mathbf{w}_1, \mathbf{w}_2\big), \end{aligned} \tag{4.23}$$

where $\mathbf{w}_1$ and $\mathbf{w}_2$ are wavelet coefficients of $\mathbf{x}_1$ and $\mathbf{x}_2$, respectively.

Similarly, the gradient of (4.23) with respect to CT image is given by

$$\begin{aligned} \frac{\partial f(\mathbf{w}_1, \mathbf{w}_2)}{\partial \mathbf{w}_1} =&\eta_1 \mathbf{W}\mathbf{A}_1^T\left(\mathbf{A}_1\mathbf{W}^T\mathbf{w}_1 - \mathbf{y}_1\right) + \xi\frac{d\|\mathbf{w}_1\|_1}{d\mathbf{w}_1} \\ &+ \lambda\Big(\cos(\mathbf{w}_1, \mathbf{w}_2)\frac{\mathbf{w}_1}{\|\mathbf{w}_1\|_2^2} - \frac{\mathbf{w}_2}{\|\mathbf{w}_1\|_2\,\|\mathbf{w}_2\|_2}\lambda\Big), \end{aligned} \tag{4.24}$$

and with respect to MRI image is given by

$$\begin{aligned} \frac{\partial f(\mathbf{w}_1, \mathbf{w}_2)}{\partial \mathbf{w}_2} =&\eta_2 \mathbf{W}\mathbf{A}_2^T\left(\mathbf{A}_2\mathbf{W}^T\mathbf{w}_2 - \mathbf{y}_2\right) + \xi\frac{d\|\mathbf{w}_2\|_1}{d\mathbf{w}_2} \\ &+ \lambda\Big(\cos(\mathbf{w}_2, \mathbf{w}_1)\frac{\mathbf{w}_2}{\|\mathbf{w}_2\|_2^2} - \frac{\mathbf{w}_1}{\|\mathbf{w}_2\|_2\,\|\mathbf{w}_1\|_2}\Big). \end{aligned} \tag{4.25}$$

The $\mathbf{w}_1$ and $\mathbf{w}_2$ can also be solved with Algorithm 1. The final image $\mathbf{x}_1$ and $\mathbf{x}_2$ are obtained by applying inverse 2-D wavelet transform to $\mathbf{w}_1$ and $\mathbf{w}_2$, respectively.

It needs to be pointed out that wavelet-based sparse prior is extremely difficult to handle compared to total variation. It often generates ripples and unevenness in image backgrounds [98, 47]. However, the choice of sparse prior is highly dependent on the application. For some applications such as ultrasound and functional magnetic resonance imaging (fMRI),

the wavelet-based priors show impressive results [99]. In this particular joint CT-MRI reconstruction, wavelet-based method shows slightly lower performance (such as lower similarity measurement) compared to total variation based-joint reconstruction [47, 48].

4.6 Summary

The essence of performing joint reconstruction is to create a framework that couples the mutual similarities between CT and MRI images. This coupling has to be embedded into the framework with a feasible numerical method to solve the optimization problem.

The multichannel imaging model, assuming inter-channel independence, reasonably fits the CT-MRI joint reconstruction model into a regularized optimization framework. The additional regularization terms include total variation and projection distance. Wavelet-based priors are difficult to handle and sometimes can generates artifacts, but they show impressive results in some applications.

The nonlinear conjugate gradient algorithm provides a numerical solution that simultaneously updates two images. The gradient of each term in the optimization framework is either analytically calculated or numerically approximated. Chapter 5 will focus on the results and analysis of the methods in this chapter.

Chapter 5

RESULTS AND DISCUSSION

The joint reconstruction framework is tested on two anatomical regions: abdomen and head. These anatomical regions consist of a pair of MRI images and CT images. The images tested in this work are both clinical images. They are reconstructed from actual raw data and pre-registered to mimic CT-MRI image pair. In additional, the sinogram and k-space data are further generated using these images by simulation. Both abdomen and head images are very common in daily clinical imaging protocols for both CT imaging and MRI. Nonetheless, the abdomen and head images here are very different in terms of their structural features and patterns. The abdominal images are composed of more complex and different tissues than the head images. The head image is rather simple because it consists of only gray matter, white matter and cerebrospinal fluid (CSF). Therefore, the CT head image used in this study is nearly piecewise constant and a fairly plain signal.

The image size is both 256×256, and the intensity is normalized to [0 1]. Thus, the default display window [100] in this work is [0, 1], if not explicitly pointed out otherwise. The undersampled CT sinogram is created by simulating a forward projection from a limited number of directions out of a full rotation ranging from 0° to 360°. Similarly, the undersampled MRI

k-space data are collected by applying an undersampling mask to the fully sampled k-space data, which are generated by applying the Fourier transform to the original image. The detailed mathematics governing the implementation of CT and MRI sampling strategies is introduced in Section 3.2.3.

The experiment is conducted by comparing the the ground truth with joint reconstruction, independent reconstruction, and the analytical method. Specifically, the three tested methods are listed as following scenarios:

1. Analytical reconstructions;
2. Reconstruction based on Equation (4.8);
3. Reconstruction based on Equation (4.18).

The comparison among the three reconstruction strategies are also compared in Table 5.1. Both joint and independent reconstructions are compressed sensing-based iterative methods. The analytical methods are FBP for CT images and Fourier transform for MRI images. It needs to be pointed out that the difference between joint and independent reconstruction is that the independent reconstruction does not incorporate the multimodal information defined by projection-distance prior.

5.1 Implementation and CUDA Acceleration

The algorithm is implemented on a PC with Microsoft Windows 10 Pro powered by a Xeon CPU. The PC has 32 gigabytes of memory such that all programs are coded in x64 modes. The computer is also equipped with an nVidia M5000M Graphic Processing Unit (GPU) with an 8-gigabyte on-chip memory driven by Compute Unified Device Architecture (CUDA)

Table 5.1: Comparison of Different Reconstruction Strategies

Algo. Descrip. \ Recon. Strategy	Analytical Recon.	Ind. Recon.	Joint Recon.
Algorithm	CT: FBP MRI: IFT	NCG	NCG
Iterative	No	Yes	Yes
TV	N/A	Yes	Yes
PD	N/A	No	Yes

8.0. The software is developed in MATLAB, C/C++, and CUDA, combined by the MEX interface.

The forward projection and back-projection for the CT imaging is programmed in CUDA-based C code to further accelerate the computation. The CT projection follows an equi-angular fanbeam geometry with no iso-center offset. The number of the detectors is 1024, which is a typical value emulating major vendors in current market. The simulated X-rays sample the object based on a group of pre-set angles. These angles are equally distributed on the entire circle with a separation $d\beta$ of

$$d\beta = \frac{2\pi}{N_\beta}, \tag{5.1}$$

where N_β is the number of the projections per revolution.

The projection model employs distance-driven model [90] for both forward projection and back-projection. As discussed in Chapter 4.2, the distance-driven method provides a perfect match between forward and backprojections. As for the MRI, the 2-D Fourier operator and its inverse are performed with built-in MATLAB functions which employs Fast Fourier

transform algorithms [101]. The Fourier transform is not carried out by GPU code, but it is sufficiently fast.

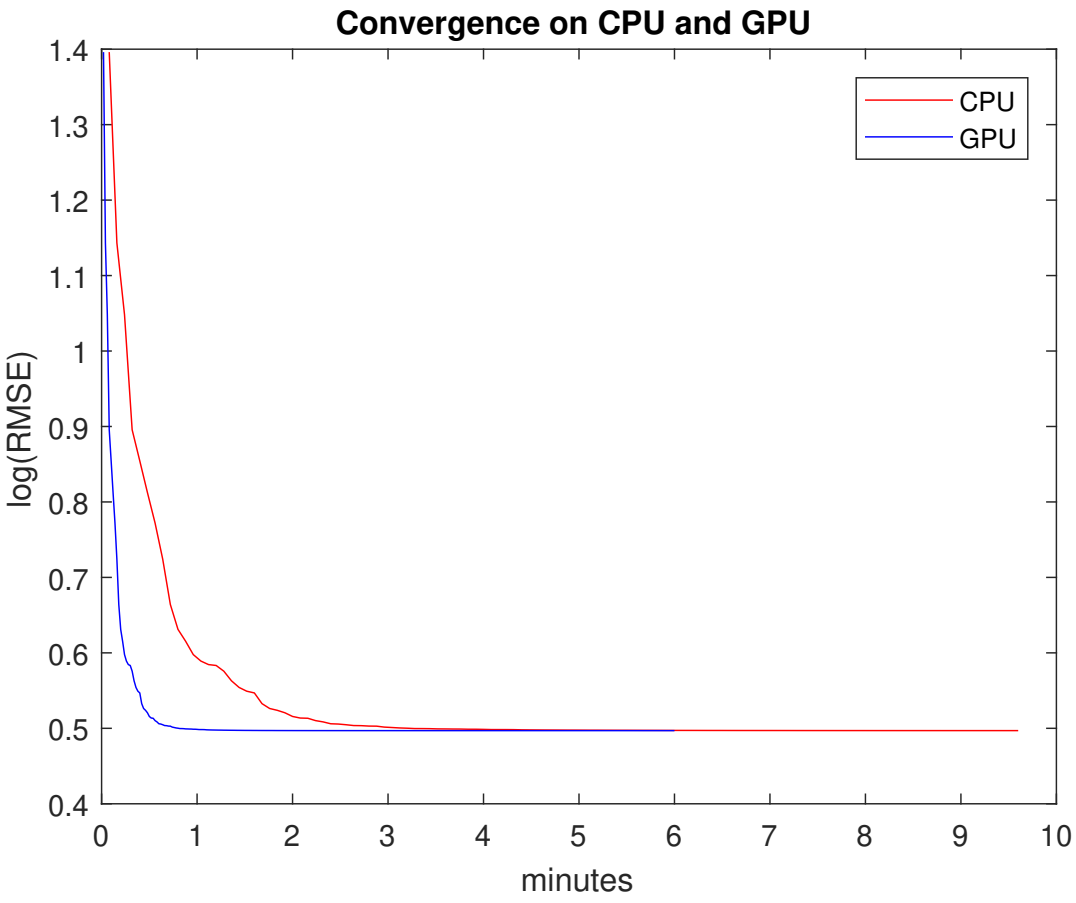

Figure 5.1: Convergence curves with CPU implementation and accelerated GPU implementation. Both follow the strategy described in Algorithm 1.

Figure 5.1 shows the convergence of reconstruction implemented in GPU and CPU, both of which follow Algorithm 1. GPU implementation significantly deceases the time of convergence as the plot shows. The NCG algorithm approaches its minimal at approximately 250 iterations, and the cost function decreases with a very steady behavior afterwards. The forward and backprojection of CT imaging are computationally expensive, so they are accelerated with CUDA implementation with massive parallelism. Consequently, each iteration

takes roughly 2 seconds to update both CT and MRI images. To get final reconstruction results, it takes approximately 5 minutes.

The extent of involving GPU coding in this project is beyond the scope of this research work. However, in the modern medical imaging field, GPU coding is an extremely powerful tool to significantly enhance computational power. In this project, only CT projection models and image gradient calculations are executed using the GPU. Potentially, more parallelism can further reduce computational times.

5.2 Abdomen Images

The results of reconstructed images are displayed in Figure 5.2 and Figure 5.3 in the following order: top left depicts the original image as the ground truth; top right depicts the compressed sensing-based joint reconstruction with projection-distance regularization; bottom left depicts the compressed sensing-based reconstruction independently on single modality without projection-distance regularization; and bottom right depicts the analytical reconstruction of the undersampled sinogram with 51 projections using a native fanbeam geometry algorithm [25] for CT, and inverse Fourier transform with a 40% k-space sampling rate for MRI. Note that the sampling rate is here empirically chosen such that the image quality (by visual inspection) is maintained with minimal amount of data. The analytical reconstruction exhibits strong artifacts due to severe undersampling. Streaks and distortion are quite obvious in both CT and MRI images. In contrast, the joint reconstruction shows a similar image quality as the independent reconstruction. Both of the reconstructed images are very similar to the truth. The choice of tuning parameters ξ and λ is empirical, and is beyond the scope of this work. The general principle is to assign heavier weight on data fidelity term than either L_1-norm prior or the distance-projection prior, and then each parameter is

normalized. The intuition is to trust the collected data with highest confidence, and to give piecewise constant phantom a little more weight on L_1-norm prior. The weights of CT and MRI data fidelity terms are determined approximately by the ratio of average energy stored in k-space to that in sinogram. For this particular project, $\eta_1 = 0.485$, $\eta_2 = 0.485$, $\xi = 0.005$ and $\lambda = 0.025$.

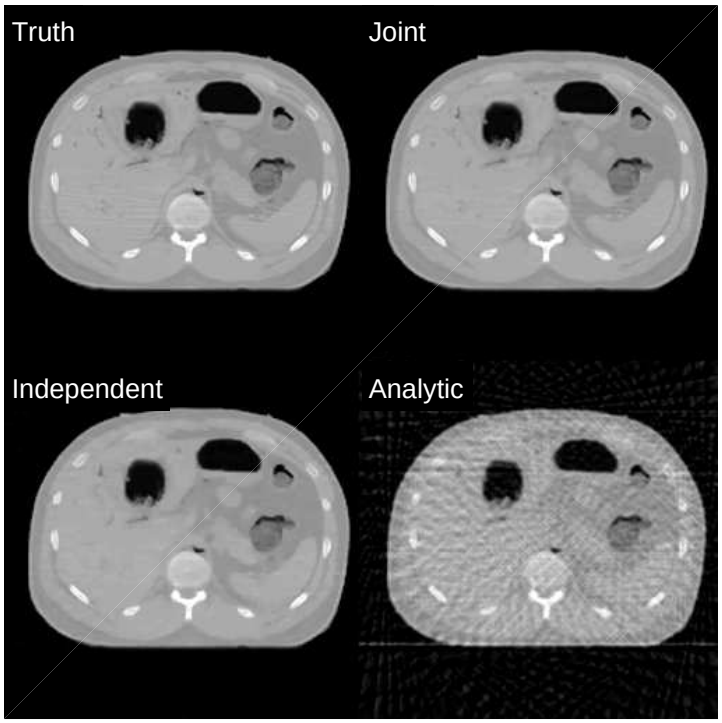

Figure 5.2: Comparison of CT reconstructions: top left depicts the ground truth; top right depicts a joint reconstruction; bottom left depicts an independent reconstruction; and bottom right depicts an analytical reconstruction. The display window is [0 1].

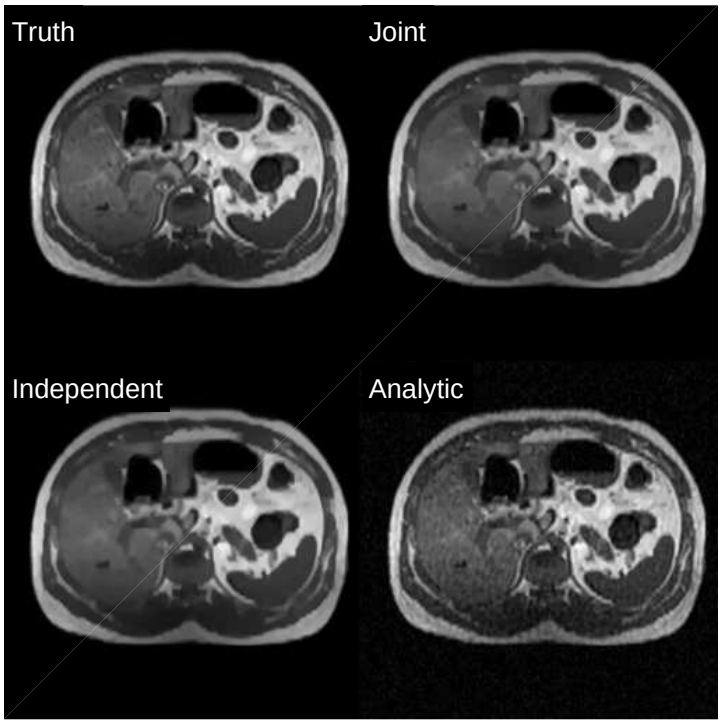

Figure 5.3: Comparison of MRI reconstructions: top left depicts the ground truth; top right depicts the joint reconstruction; bottom left depicts the independent reconstruction; and bottom right depicts an analytical reconstruction. The display window is [0 1].

A detailed analysis is conducted by observing zoomed-in region of interests (ROIs). The ROIs are labeled in red as depicted in Figure 5.4. Figure 5.4 also defines background regions where noise, labeled in blue, is calculated. This will be further explained in the paragraph that addresses the statistics of ROIs.

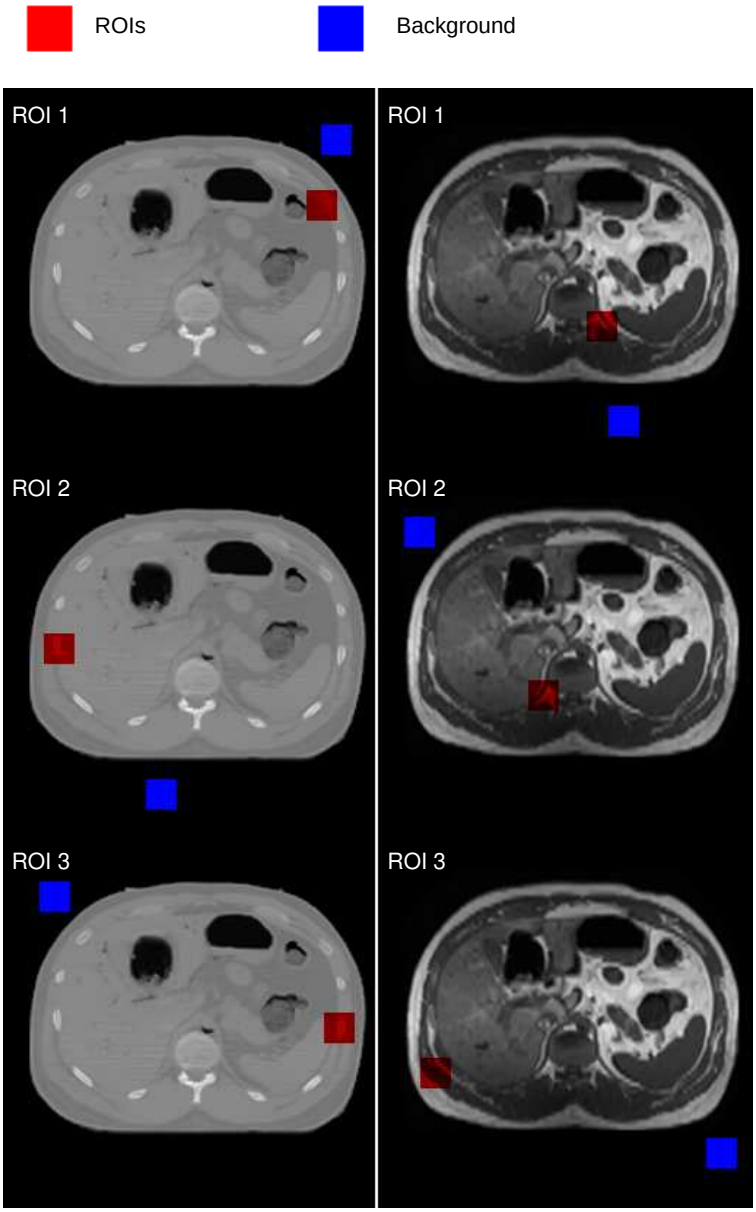

Figure 5.4: Three ROIs are chosen from both CT and MRI images. ROIs are highlighted in red, whereas regions of background are also chosen, but labeled in blue. The display window is [0 1].

Figure 5.5 and Figure 5.6 display ROIs for CT and MRI abdominal images, respectively. CT ROIs focus on bony structures which absorb a large amount of X-ray photons, and therefore show much higher intensity. Similarly, MRI ROIs are chosen with tissues containing a high

density of protons, such as lipids, as they show stronger intensity in images. Evaluation of these images focuses on the texture, artifacts, resolution and noise. By visual inspection, it is observed that the joint reconstruction (top right panel) provides the strongest intensity and focus, especially at boundaries and edges. It also achieves the best resolution among the tested reconstruction methods. In addition, the joint reconstruction also exhibits the best smoothness in background tissue, especially in MRI ROIs.

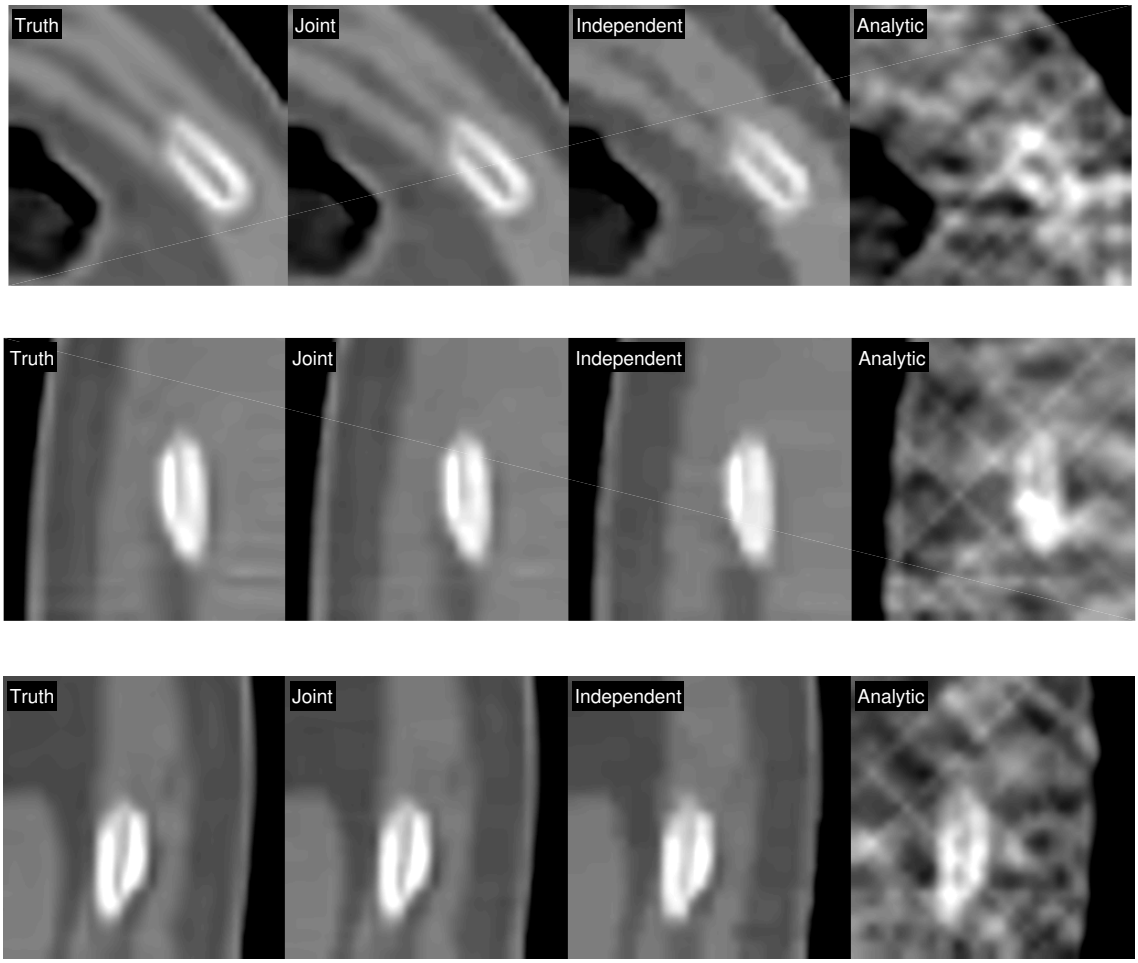

Figure 5.5: ROI comparison for CT images with all three ROIs being defined in Fig. 5.4 shown in red; All ROIs are zoomed in with zoom factor of 8×. Display window is [0 1].

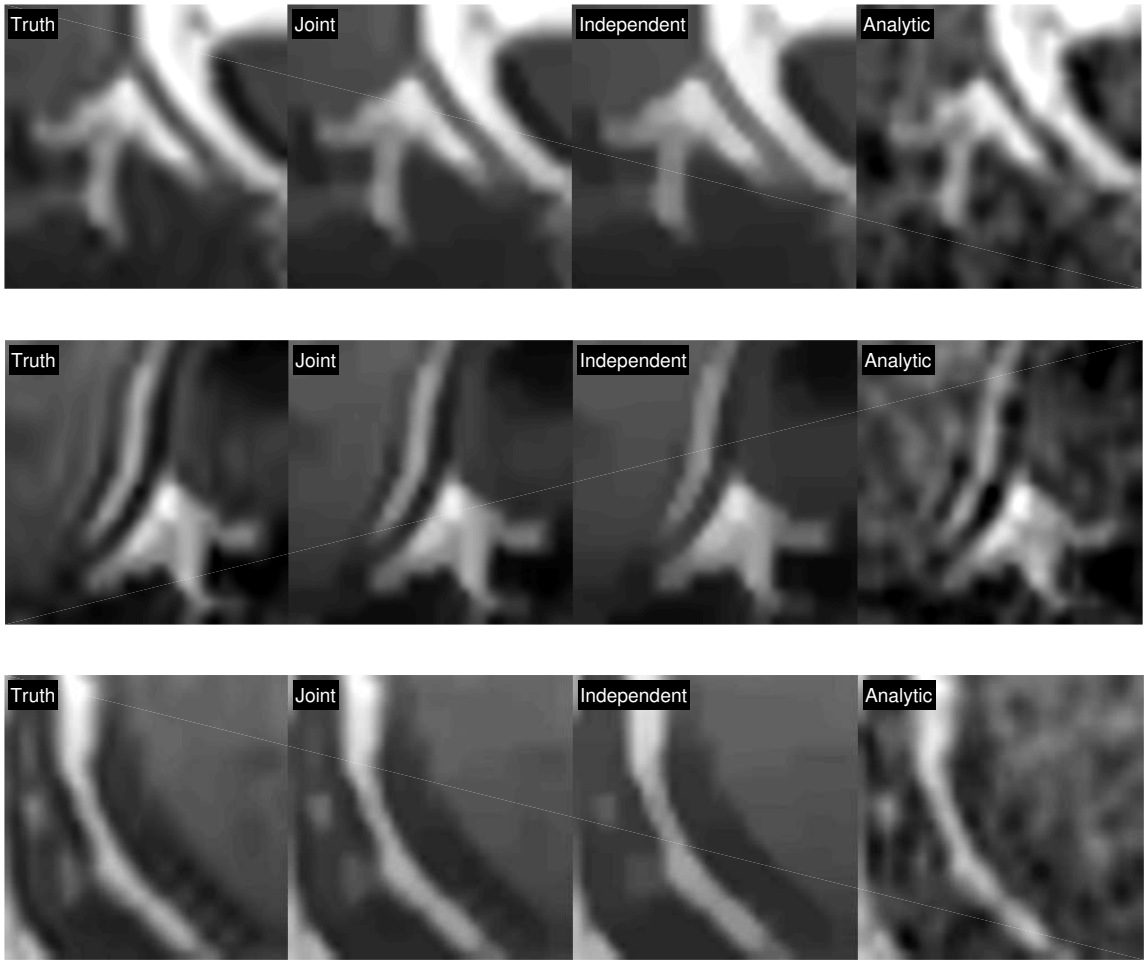

Figure 5.6: ROI comparison for MRI images with all three ROIs being defined in Fig. 5.4 shown in red; All ROIs are zoomed in with zoom factor of 8×. Display window is [0 1].

Image differences are also examined. Figure 5.7 and Figure 5.8 show the image differences for different reconstructions compared to the truth. In particular, image difference gives a much clearer distinction between joint and independent reconstruction, both of which are iterative methods. Under the proper window level, joint reconstruction shows much less difference than independent reconstruction when both are compared to the truth.

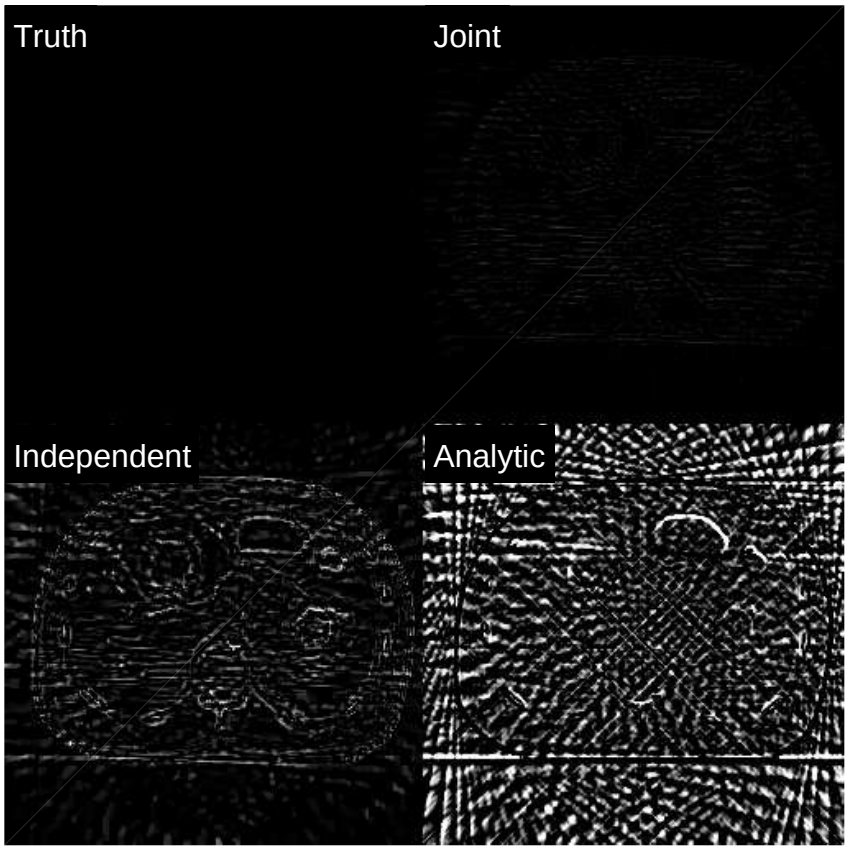

Figure 5.7: Image difference for CT abdomen phantom with respect to ground truth: truth on the top left; joint reconstruction on the top right; independent reconstruction on the bottom left; analytical reconstruction on the bottom right. The display window is [0 0.08].

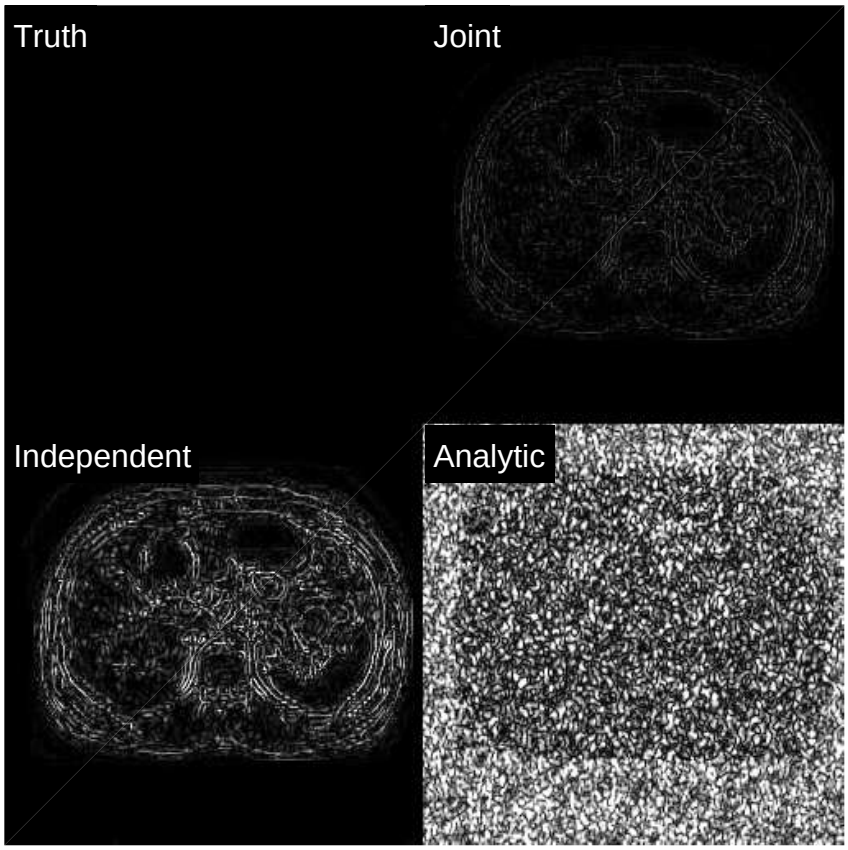

Figure 5.8: Image difference for MRI abdomen phantom with respect to ground truth: truth on the top left; joint reconstruction on the top right; independent reconstruction on the bottom left; analytical reconstruction on the bottom right. The display windows is [0 0.08].

Quantitative analysis using statistics are performed for each ROI. All ROIs highlighted in red are considered regions of signal. The background regions, highlighted in blue in Figure 5.4, are chosen to evaluate noise. All regions of signal intentionally contain high intensity objects, and all backgroud regions are located where no anatomical regions are being imaged. The signal-to-noise ratio (SNR) is calculated for each reconstruction for comparison. For digital images, the SNR is defined as [102]

$$SNR = 20 \log_{10} \left(\frac{\mu_{signal}}{\sigma_{background}} \right) \tag{5.2}$$

with unit of decibel (dB). In Equation 5.2, μ_{signal} is the mean value of the signal region, and $\sigma_{background}$ is the standard deviation of the noise of the background region. In general, SNR is a very important measurement used in signal and image processing, but it is also extensively used in evaluation for medical image quality [103, 104, 105]. As Figure (5.4) shows, the signal region is represented in red while the noise region is represented in blue. Maximal values, minimal values, and mean values are computed for each signal region, and noise is computed as the standard deviation of each background region. The results of the CT and MRI ROIs are listed in Table 5.2 and Table 5.3, respectively.

The statistical results confirm the previous visual inspection: joint reconstruction recovers the truth with the highest correlation and confidence. In particular, it approximates the true signal better in high intensity locations and generates less noise in the background. The independent reconstruction results are near the quality achieved by the joint reconstruction method, but it misses some of the details of the images. In addition, the analytical reconstruction method sometimes gives a stronger signal intensity than the joint reconstruction method, but its background noise is extremely large, and this eventually leads to a very poor SNR. Figure 5.9 displays values of SNR according to Equation (5.2) for different reconstructions. The calculation is based on normalized image pixel values. SNRs of both CT and MRI images follow a descending order from truth to analytical as the graph shows.

In addition to statistical comparisons, a line profile is another way to investigate the reconstruction quality. The line profiles are drawn in the same ROIs as defined in Figure 5.4, and they are across areas that contain high frequency components such as boundaries and edges. Figure 5.10 and Figure 5.11 display how each reconstruction performs compared to the ground truth. The results are consistent with those from visual inspection and statistical analysis. Joint reconstruction, among the three, gives the best reconstruction quality, independent reconstruction offers suboptimal quality, and analytical reconstruction holds a

Table 5.2: Statistics of Abdomen CT ROIs

ROI	Stats	Truth	Joint	Ind.	Ana.
ROI 1	Max	0.666	0.664	0.652	0.679
	Min	0.519	0.522	0.514	0.425
	Mean	0.590	0.590	0.588	0.563
	Noise	0.0010	0.0015	0.0023	0.0609
	SNR (dB)	55	52	48	19
ROI 2	Max	0.803	0.788	0.776	0.778
	Min	0.529	0.523	0.524	0.479
	Mean	0.656	0.627	0.623	0.589
	Noise	0.0011	0.0016	0.00528	0.0318
	SNR(dB)	56	52	41	25
ROI 3	Max	0.825	0.822	0.809	0.761
	Min	0.470	0.469	0.486	0.447
	Mean	0.632	0.632	0.630	0.625
	Noise	0.0011	0.0014	0.0051	0.0306
	SNR(dB)	55	53	42	26
Ave.	Max	0.7647	0.7580	0.7457	0.7393
	Min	0.5060	0.5047	0.5080	0.4503
	Mean	0.6260	0.6163	0.6137	0.5923
	Noise	0.0011	0.0015	0.0042	0.0411
	SNR(dB)	55	52	44	24

Table 5.3: Statistics of Abdomen MRI ROIs

ROI	Stats	Truth	Joint	Ind.	Ana.
ROI 1	Max	0.739	0.716	0.709	0.783
	Min	0.098	0.122	0.123	0.022
	Mean	0.321	0.320	0.318	0.322
	Noise	0.0010	0.0015	0.0023	0.0609
	SNR(dB)	50	47	43	14
ROI 2	Max	0.687	0.650	0.637	0.718
	Min	0.078	0.107	0.109	0.047
	Mean	0.248	0.248	0.246	0.251
	Noise	0.0011	0.0016	0.00528	0.0318
	SNR(dB)	47	44	33	18
ROI 3	Max	0.622	0.577	0.567	0.618
	Min	0.120	0.156	0.157	0.088
	Mean	0.289	0.288	0.286	0.291
	Noise	0.0011	0.0014	0.0051	0.0306
	SNR (dB)	48	46	35	20
Ave.	Max	0.6827	0.6477	0.6377	0.7063
	Min	0.0987	0.1283	0.1297	0.0523
	Mean	0.2860	0.2853	0.2833	0.2880
	Noise	0.0011	0.0015	0.0042	0.0411
	SNR(dB)	49	46	38	18

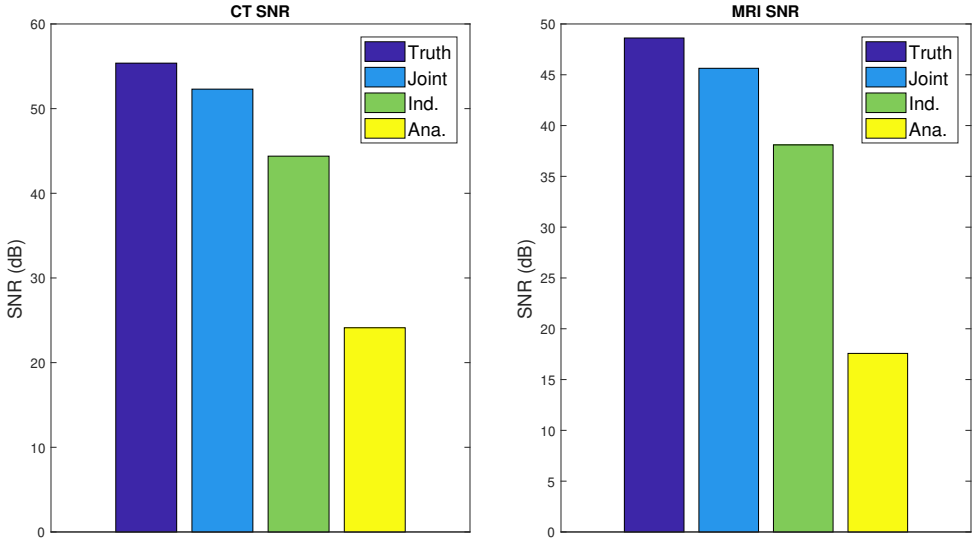

Figure 5.9: Averaged SNR comparison for CT and MRI reconstruction using the joint, individual and analytical methods.

far more inferior result to the aforementioned two.

Similarity metrics between the ground truth and its reconstructed versions are computed as the third mean for verification. The metrics here include the root-mean-square error (RMSE), the structural similarity (SSIM) [91], and the correlation coefficients. The results are displayed in Table 5.4 for CT imaging and in Table 5.5 for MRI. All calculations are based on normalized images as aforementioned. For both CT and MRI, joint reconstruction exhibits the highest similarity and correlation with the ground truth. The independent reconstruction follows the joint reconstruction. The analytical method is ranked as the lowest among all the tested methods in this work.

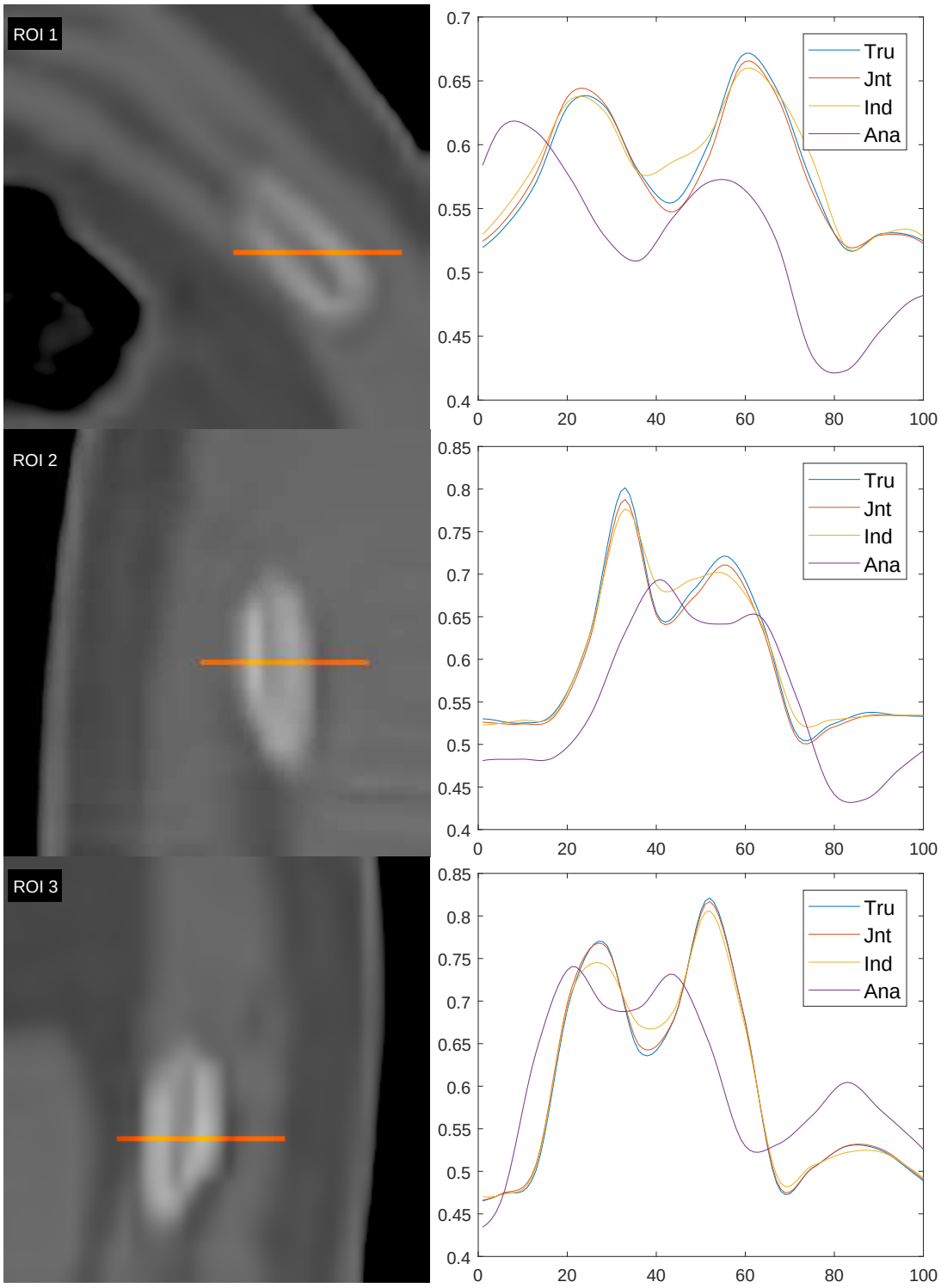

Figure 5.10: CT reconstruction comparison in line ROIs. Left column shows the line ROIs highlighted in orange. The right column shows the corresponding ROI profiles associated with different reconstructions. The display window on left column is [0 1].

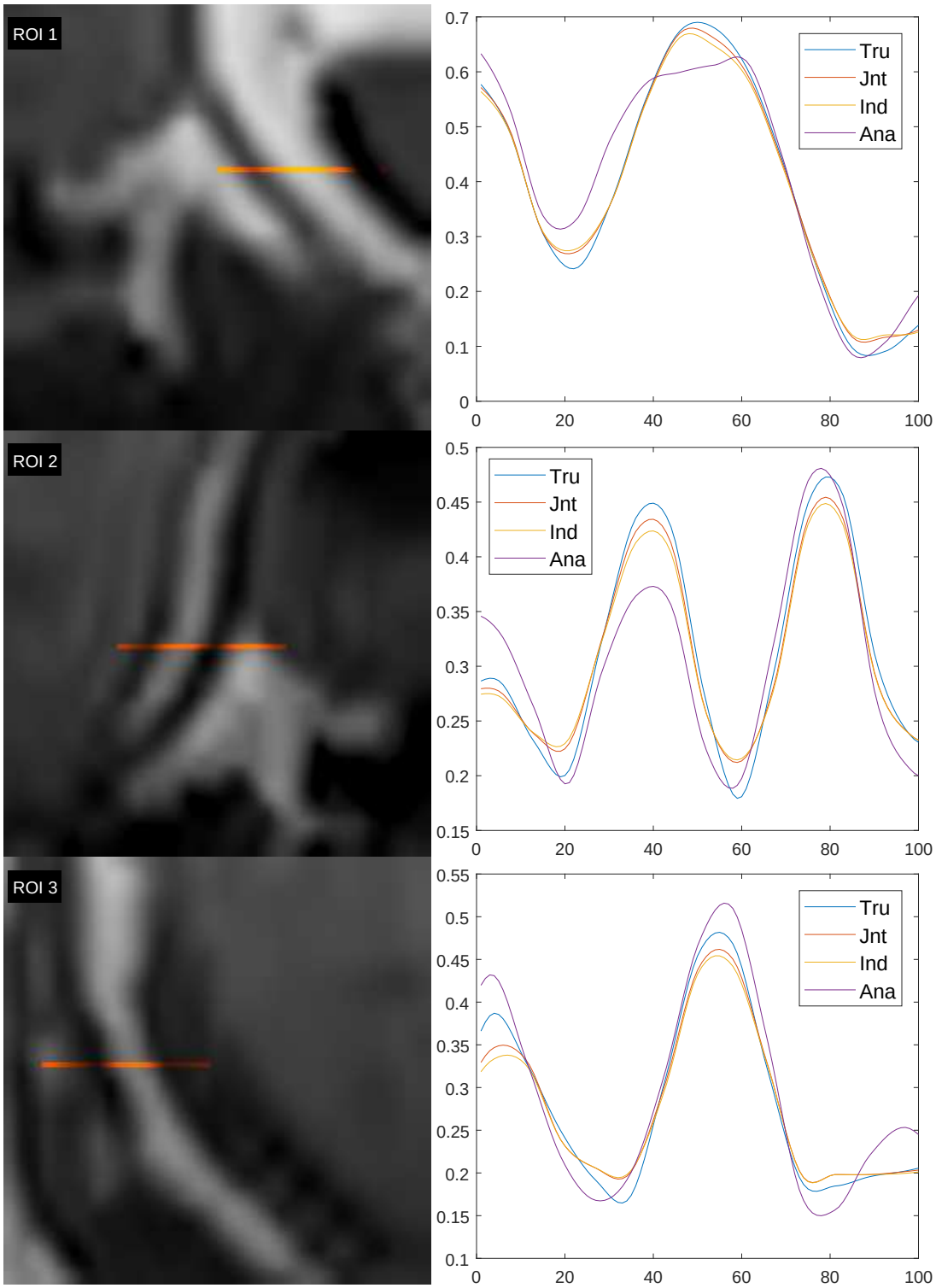

Figure 5.11: MRI reconstruction comparison in line ROIs. Left column shows the line ROIs highlighted in orange. The right column shows the corresponding ROI profiles associated with different reconstructions. The display window on left column is [0 1].

Table 5.4: Similarity Measurement for Abdomen CT Reconstruction

Strategy	RMSE	SSIM	Correlation
Analytical	13.5862	0.4135	0.9786
Independent	1.7551	0.9690	0.9996
Joint	0.7578	1.0000	0.9999
Truth	0.0000	1.0000	1.0000

Table 5.5: Similarity Measurement for Abdomen MRI Reconstruction

Strategy	RMSE	SSIM	Correlation
Analytical	11.2517	0.4717	0.9860
Independent	2.3990	0.9755	0.9991
Joint	2.0061	0.9869	0.9993
Truth	0.0000	1.0000	1.0000

5.3 Head Images

In addition to abdominal images, the head images are also tested with the same procedures. The results are displayed in Figure 5.12 and Figure 5.13 in the following order: top left depicts the original image as ground truth; top right depicts the joint reconstruction with projection distance regularization; bottom left depicts the independent reconstruction; and bottom right depicts the analytical reconstruction of the undersampled sinogram with 25 projections for CT, and an inverse Fourier transform with 30% k-space sampling rate for MRI. The analytical reconstruction shows the strongest artifacts and the joint reconstruction shows the best image quality. Both of the reconstructed images are very similar to the truth. The principle of choosing the tuning parameters here are the same as the abdominal

experiment, which gives $\eta_1 = 0.4825$, $\eta_2 = 0.4825$, $\xi = 0.01$ and $\lambda = 0.025$.

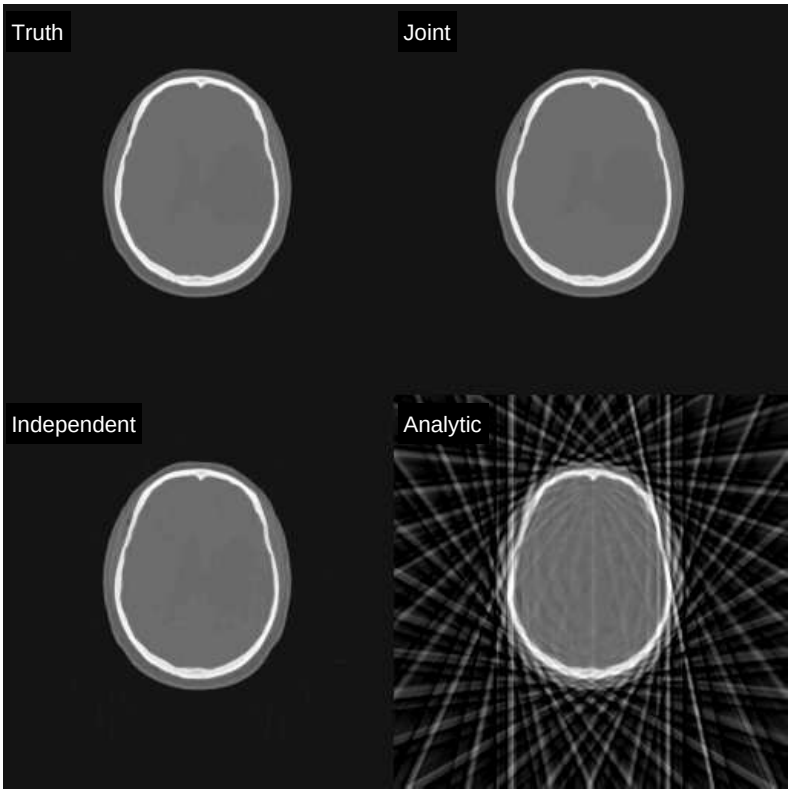

Figure 5.12: Comparison of CT reconstructions: top left depicts the ground truth; top right depicts the joint reconstruction; bottom left depicts the independent reconstruction; and bottom right depicts the analytical reconstruction. The display window is [0 1].

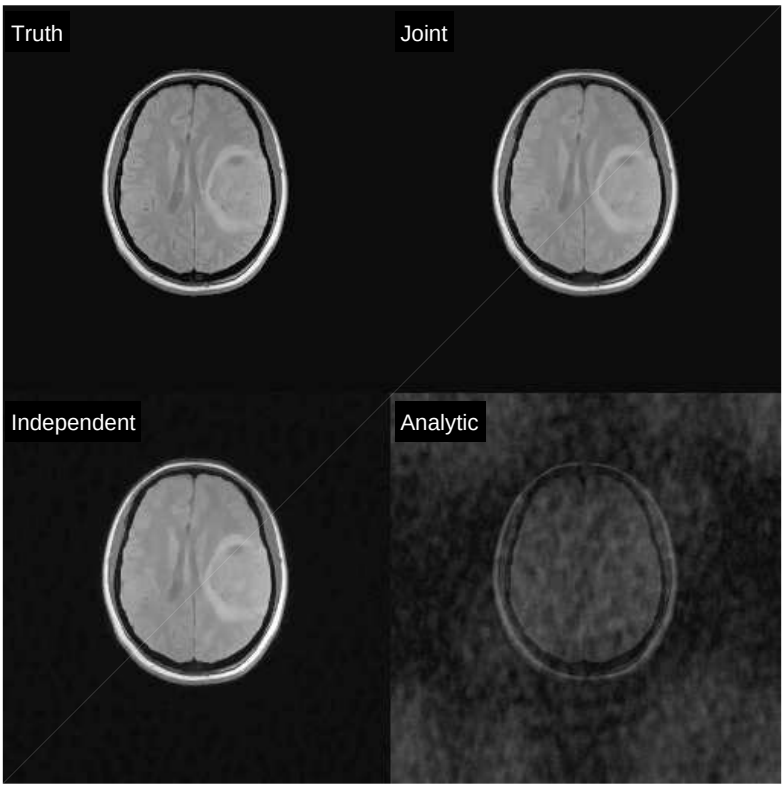

Figure 5.13: Comparison of MRI reconstructions: top left depicts the ground truth; top right depicts the joint reconstruction; bottom left depicts the independent reconstruction; and bottom right depicts an analytical reconstruction. The display window is [0 1].

Figure 5.17 and Figure 5.18 display ROIs for head images. Both CT and MRI ROIs of head images still focus on edges and boundaries. The joint reconstruction shows slight advantages over the independent reconstruction in CT head images. This is due to the fact that the head images in this work are extremely piecewise constant. Alternatively, joint reconstruction shows distinct improvements compared to independent reconstruction from MRI data due to the more complex structures found in gray and white matter.

Similarly, image difference is calculated and is displayed in Figure 5.14 and Figure 5.15. Joint reconstruction, as figures shows, has the minimal difference with ground truth for both CT and MRI head images.

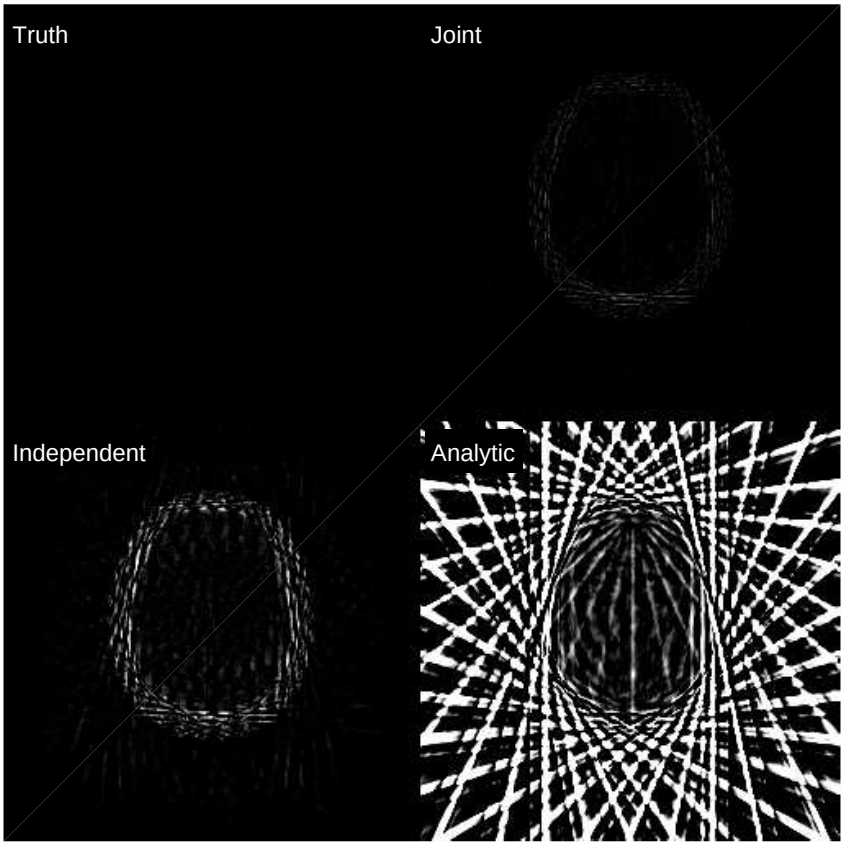

Figure 5.14: Image difference for CT head phantom with respect to ground truth: truth on the top left; joint reconstruction on the top right; independent reconstruction on the bottom left; analytical reconstruction on the bottom right. The display window is [0 0.08].

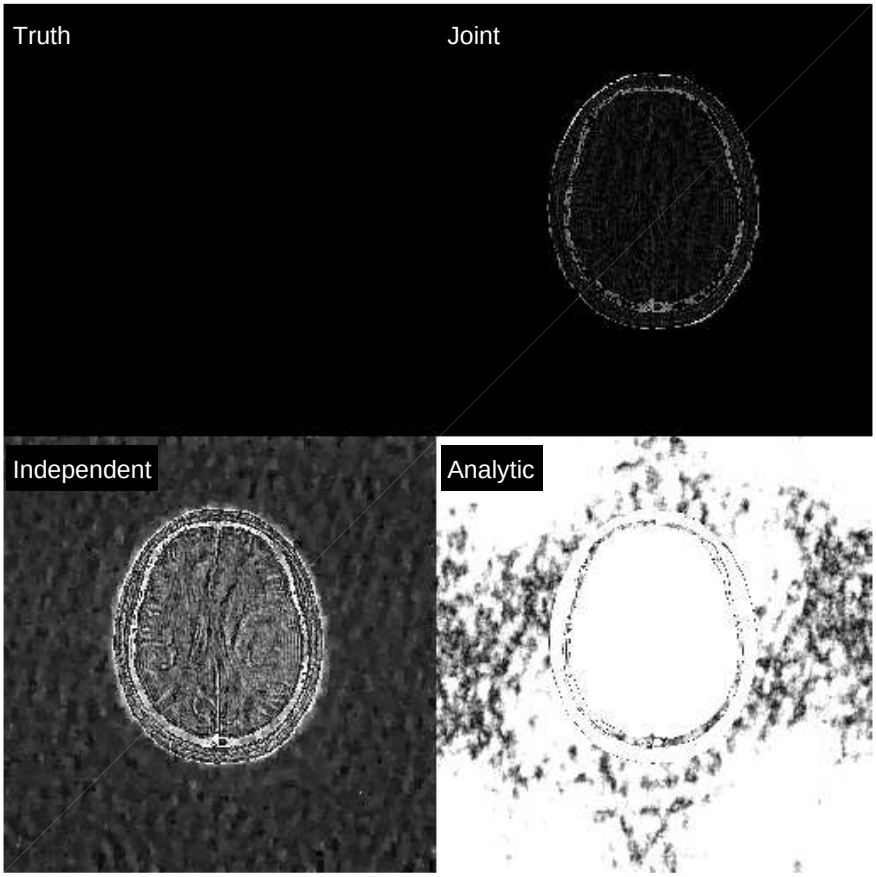

Figure 5.15: Image difference for MRI head phantom with respect to ground truth: truth on the top left; joint reconstruction on the top right; independent reconstruction on the bottom left; analytical reconstruction on the bottom right. The display window is [0 0.08].

Two ROIs are defined as shown in Figure 5.16. Signal and noise region are color-coded in red and blue, respectively. Maximal values, minimal values, and mean values are computed for each signal region, and noise is computed for each background region. The results are listed in Table 5.6 and Table 5.7, respectively.

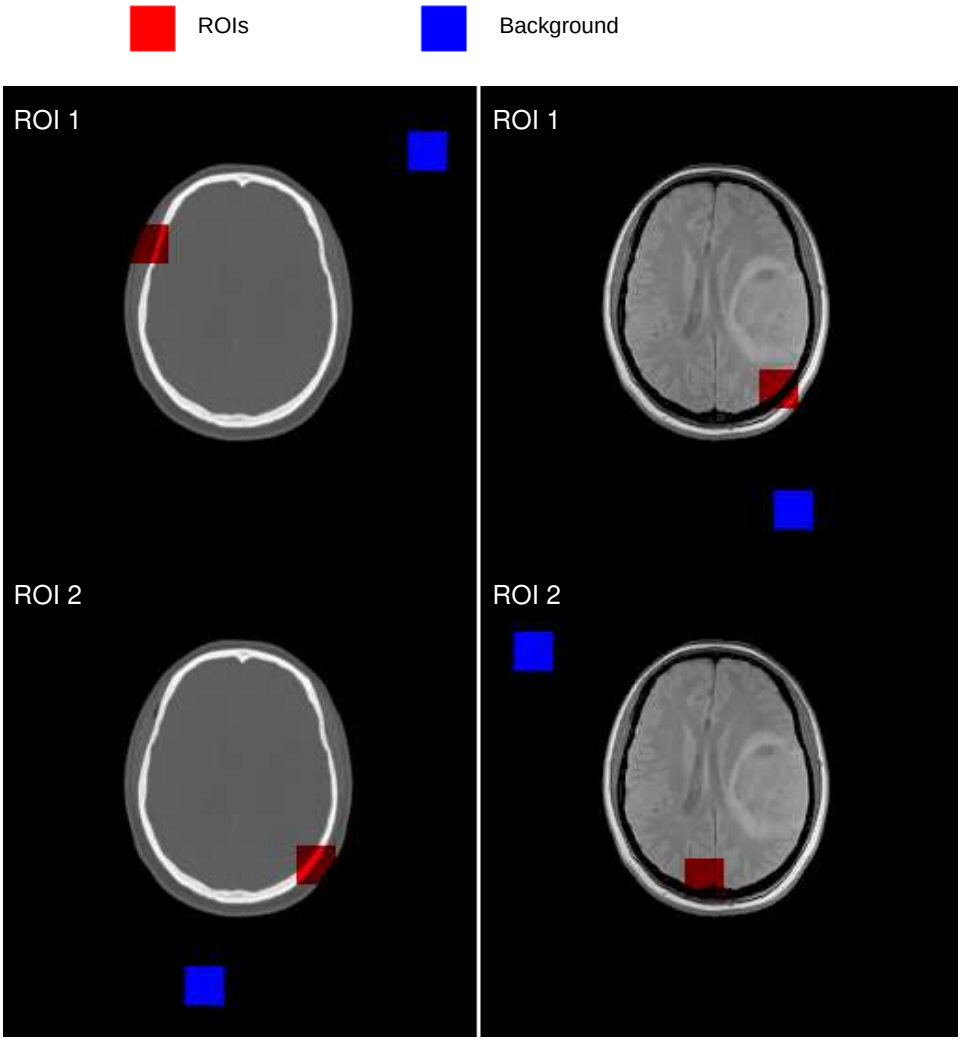

Figure 5.16: Two ROIs are chosen from both CT and MRI head images. ROIs are highlighted in red, whereas regions of background are also chosen, and are labeled in blue.

ROIs magnified with 8× zoom-in are displayed in Figure 5.17 and Figure 5.18. Iterative methods in general show much higher quality than analytical methods. In particular, the joint reconstruction displays outstanding reconstruction quality in MRI head images which has more complex features compared to its CT counterpart.

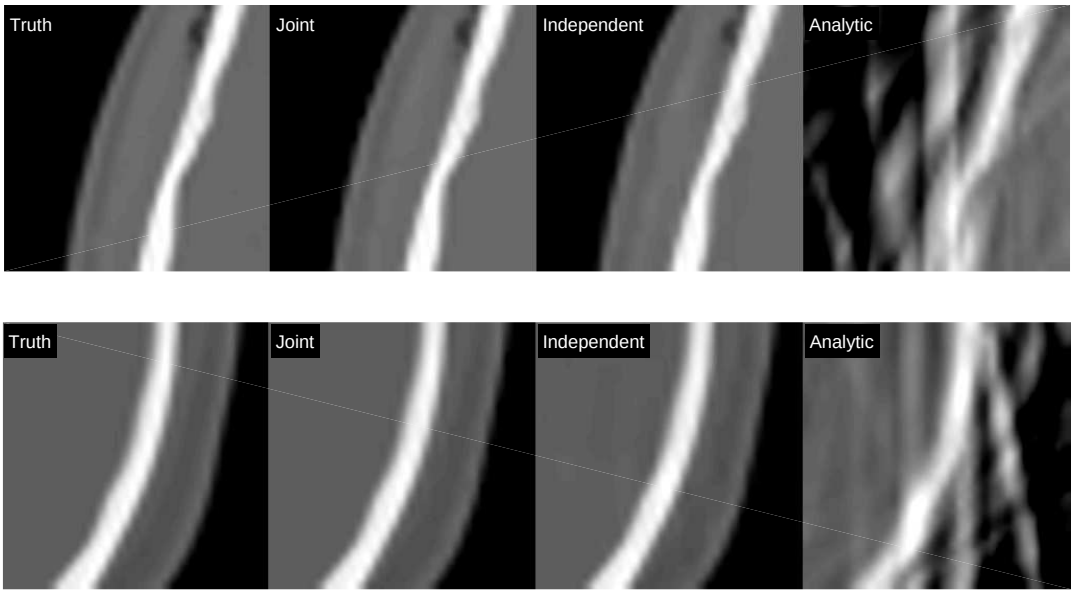

Figure 5.17: ROI comparison for CT head images with all two ROIs being defined in Fig. 5.16 in red; All ROIs are zoomed in with zoom factor of 8×. Display window is [0 1].

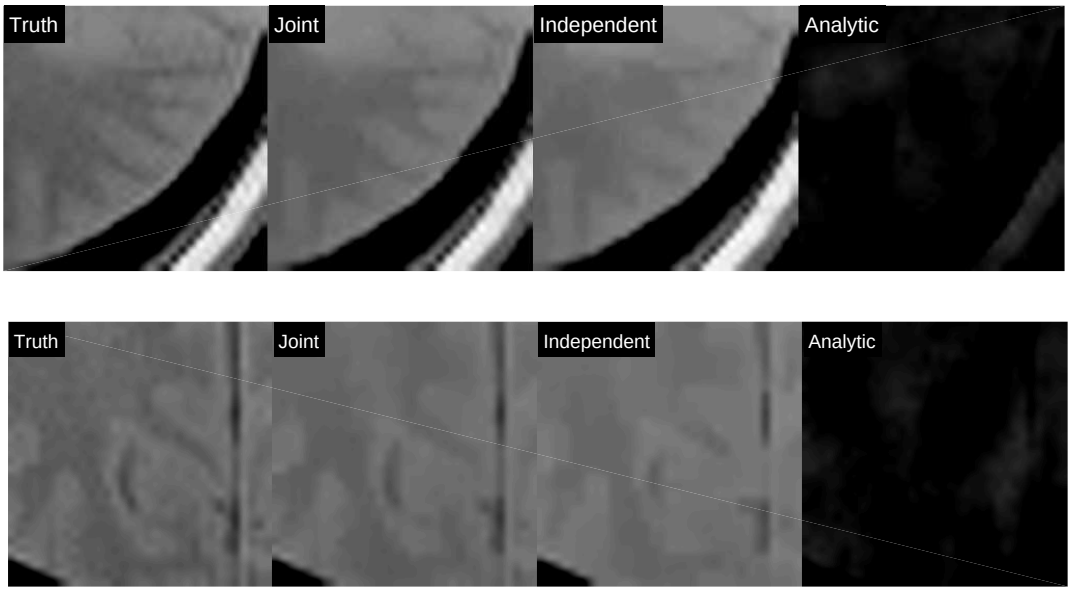

Figure 5.18: ROI comparison for MRI images with all three ROIs being defined in Fig. 5.16 in red; All ROIs are zoomed in with zoom factor of 8×. Display window is [0 1].

Table 5.6 and Table 5.7 show that joint reconstruction gives the best image quality by offering an outstanding SNR. It should be noted that the MRI head image gives better

Table 5.6: Statistics of Head CT ROIs

ROI	Stats	Truth	Joint	Ind.	Ana.
ROI 1	Max	0.9523	0.9143	0.8568	0.9272
	Min	0.4813	0.5023	0.5101	0.1111
	Mean	0.6417	0.6415	0.6327	0.6548
	Noise	0.0010	0.0015	0.0016	0.1309
	SNR(dB)	56	56	52	14
ROI 2	Max	0.9896	0.9864	0.9500	0.9876
	Min	0.4823	0.5122	0.5113	0.1146
	Mean	0.6564	0.6562	0.6434	0.6581
	Noise	0.0009	0.0012	0.0013	0.1328
	SNR (dB)	57	55	54	14
Ave.	Max	0.9709	0.9504	0.9034	0.9574
	Min	0.4818	0.5072	0.5107	0.1129
	Mean	0.6491	0.6488	0.6381	0.6564
	Noise	0.0010	0.0014	0.0014	0.1318
	SNR(dB)	57	54	53	14

Table 5.7: Statistics of Head MRI ROIs

ROI	Stats	Truth	Joint	Ind.	Ana.
ROI 1	Max	0.9978	0.9601	0.9698	0.3696
	Min	0.0023	0.0058	0.0095	0.0050
	Mean	0.5760	0.5670	0.5511	0.2730
	Noise	0.0029	0.0054	0.0095	0.0439
	SNR(dB)	46	40	35	16
ROI 2	Max	0.6740	0.6623	0.6472	0.4074
	Min	0.0162	0.0537	0.0461	0.0856
	Mean	0.4109	0.4020	0.3929	0.1028
	Noise	0.0030	0.0052	0.0093	0.0435
	SNR(dB)	43	38	33	7
Ave.	Max	0.8359	0.8112	0.8085	0.3885
	Min	0.0092	0.0297	0.0278	0.0453
	Mean	0.4934	0.4845	0.4720	0.1979
	Noise	0.0029	0.0053	0.0094	0.0237
	SNR(dB)	44	39	34	12

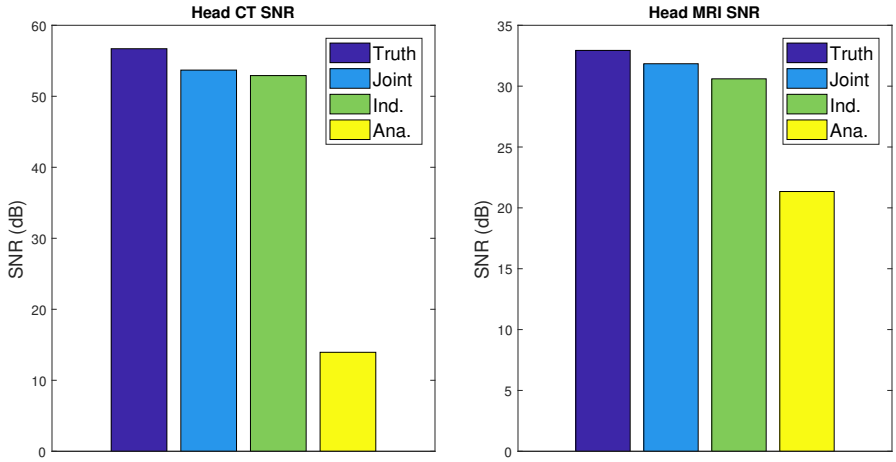

Figure 5.19: Averaged SNR comparison for CT and MRI head images using the joint, individual, and analytical reconstructions.

SNR compared to its CT counterpart. This is again due to the fact that the MRI head image has more subtle and complex image patterns than the CT head image here. Figure 5.19 displays values of SNR according to Equation 5.2 for different reconstructions. The calculation is based on normalized image pixel values. SNRs of both CT and MRI images follow a descending order from truth to analytical as the graph shows.

Figure 5.20 and Figure 5.21 display profiles of chosen line ROIs. The results consistently confirm that joint reconstruction, among the three, gives the best reconstruction quality of reconstruction.

Metrics of similarity and correlation between ground truth and different reconstruction strategies are displayed in Table 5.8 and in Table 5.9. For both the CT and MRI head images, the joint reconstruction exhibits the highest similarity and correlation with the ground truth.

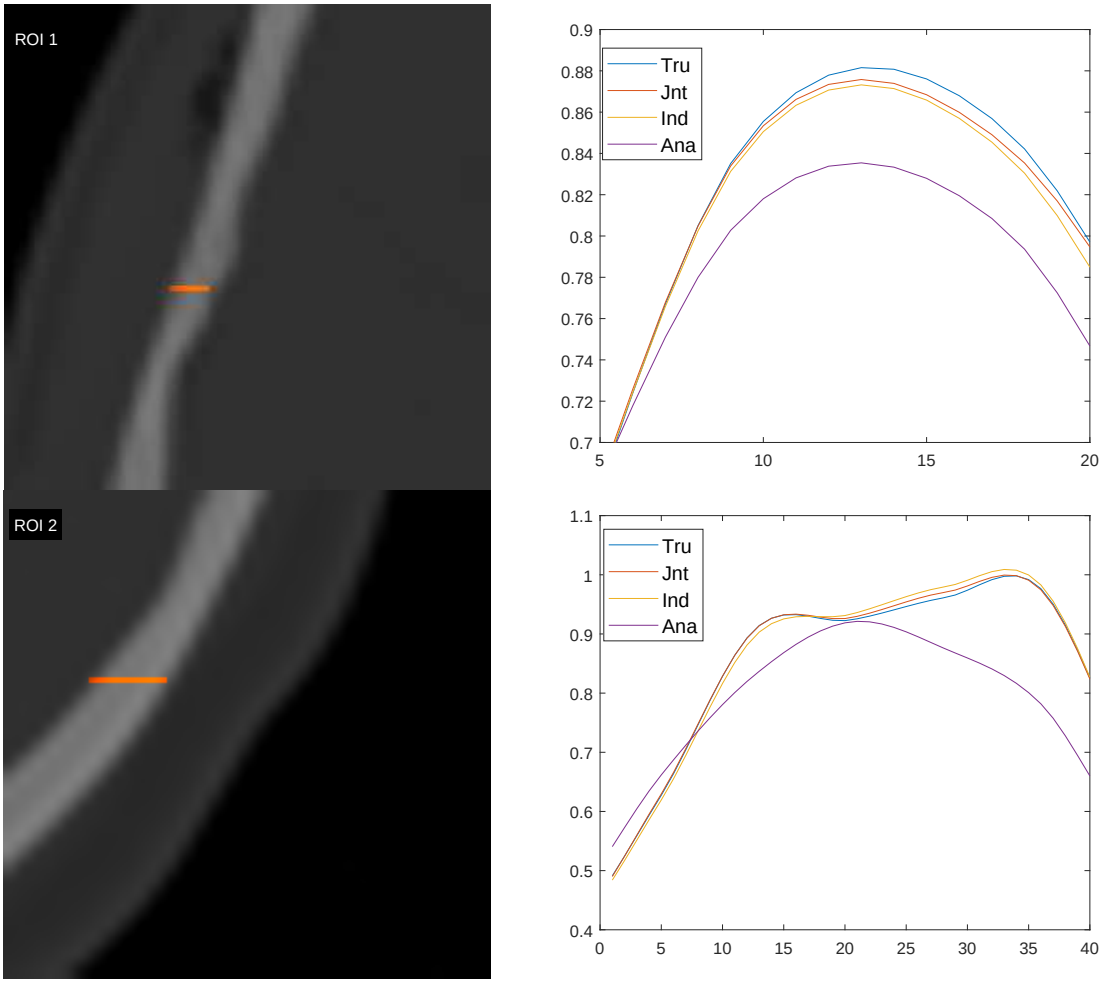

Figure 5.20: CT reconstruction comparison in line ROIs. Left column shows the line ROIs highlighted in orange. The right column shows the corresponding ROI profiles associated with different reconstructions. The display window on left column is [0 1].

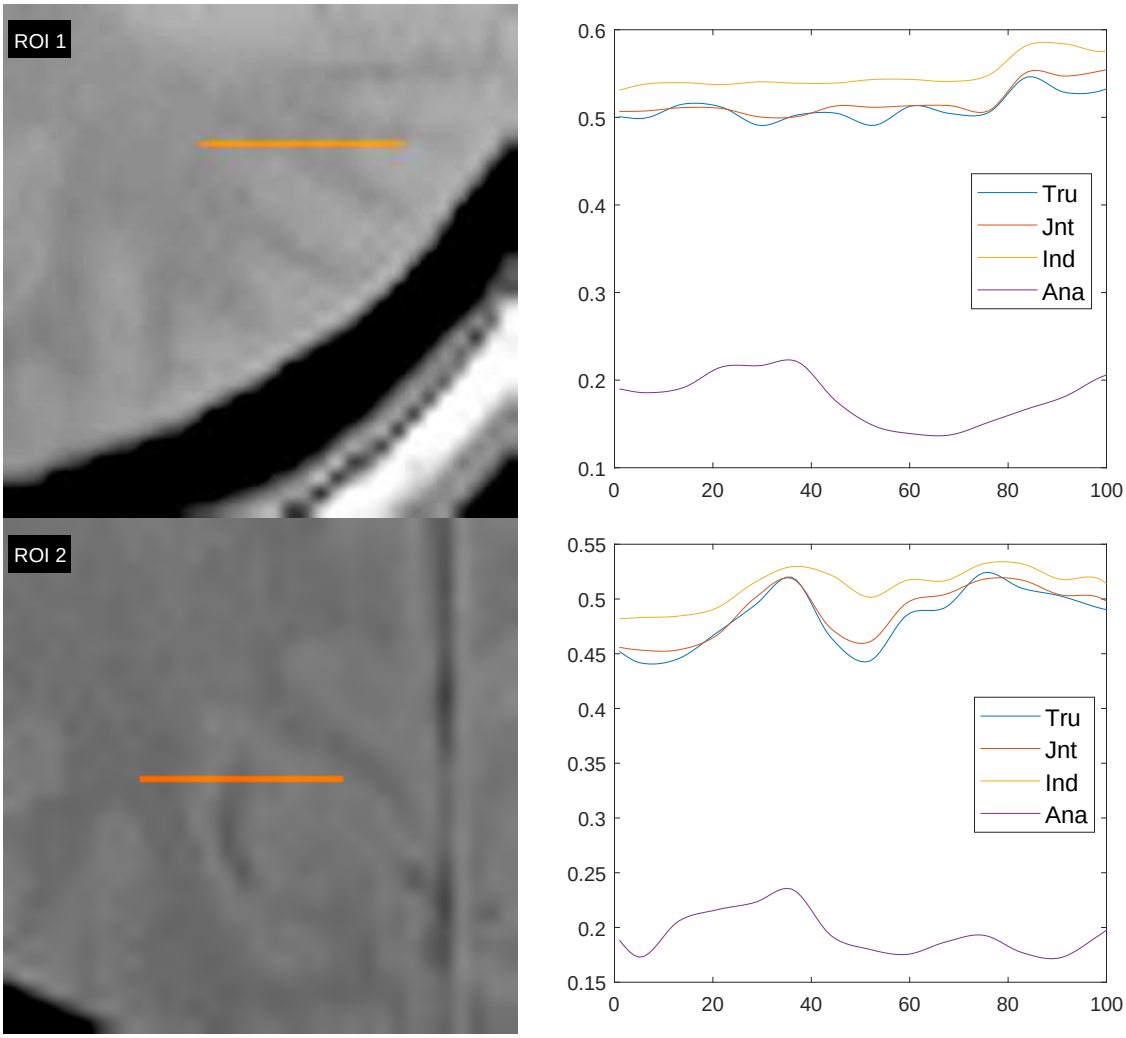

Figure 5.21: MRI reconstruction comparison in line ROIs. Left column shows the line ROIs highlighted in orange. The right column shows the corresponding ROI profiles associated with different reconstructions. The display window on left column is [0 1].

Table 5.8: Similarity Measurement for Head CT Reconstruction

Strategy	RMSE	SSIM	Correlation
Analytical	33.3465	0.1790	0.8231
Independent	1.1347	0.9775	0.9996
Joint	0.6636	0.9991	0.9999
Truth	0.0000	1.0000	1.0000

Table 5.9: Similarity Measurement for Head MRI Reconstruction

Strategy	RMSE	SSIM	Correlation
Analytical	44.7891	0.1078	0.6164
Independent	6.2426	0.9523	0.9977
Joint	2.7671	0.9785	0.9984
Truth	0.0000	1.0000	1.0000

5.4 Summary

Numerical simulations reveal that the joint reconstruction provides a significant improvement in image quality compared to analytical and independent reconstructions, especially for anatomy with complex structures such as the abdominal region. When a selected anatomy shows relatively simple structures, for example CT head images with significant piecewise constant features, independent reconstruction performs nearly as well as joint reconstruction.

Simple anatomies require much less amount of sampling to achieve the similar reconstruction quality as anatomies with complex structures. For instance, CT reconstruction requires only 25 projections for head images compared to the 51 for abdominal images to achieve similar image quality. For MRI, head images require 30% of the sampling rate compared to 40% for

abdomen images.

The compressed sensing-based multichannel imaging model are computationally heavy, but are friendly for parallelism, and can be easily scaled up to the scenarios where more imaging modalities are in the system.

Chapter 6

CONCLUSIONS AND FUTURE DIRECTIONS

In this research project, a novel joint image reconstruction framework is proposed that performs simultaneous CT-MRI image reconstruction. The proposed method resorts to a compressed sensing technique to reconstruct highly undersampled CT and MRI images on the planned omni-tomography scanning system. In addition, multimodal information such as structural similarities is explored to enhance reconstruction quality. Numerical results show that significant improvements are obtained for joint reconstruction compared to analytical methods or independent methods. The joint reconstruction framework here gives an example of how to achieve multimodal reconstruction with highly undersampled data. The coupling of multimodal information is instrumental and needs to be handled properly to balance the image quality. Total variation is included so that artifacts are suppressed. Projection distance here governs the divergence between different modalities so that structural similarity is preserved. When anatomies are more piecewise constant, they require much less sampling than complex anatomies to achieve a similar reconstruction quality. In conclusion, the joint

reconstruction framework proposed in this work produces outstanding image reconstruction quality when using the iterative-based methods that incorporates multimodal structural similarities.

The future work of joint reconstruction will focus on exploring whether and how learning-based methods can further improve image quality. The reviving neural network concepts lead to large scale deep learning developments. Among them, the generative adversarial networks (GANs) [106] show great potential for multimodal imaging problems. GANs are deep neuralnets-based architectures consisting of two parties which are competeing against each other. The two parties are the generative side and the discriminative side with the former tasked with generating products as deceptively as possible and the latter tasked with detecting the deception to the most feasible extent. The competition eventually leads to an equilibrium where the outcome is ultimately optimized to fully meet the expectation of the discriminative side. This technique is known to be capable of mimicing pictures which look at least superficially authentic to humans [107]. In many cases, GANs are employed simply as a black box which performs some unknown transfer function often too complicated to formulate with mathematics. This can be potentially beneficial for multimodal image reconstruction with highly undersampled data such as the joint CT-MRI framework presented in this work. Presumably, CT images can be easily converted to the corresponding MRI images and *vice versa* with pre-trained GANs. Under this scenario, the sampling rate can be further reduced because the prior knowledge is abundant enough that perhaps only one image modality is sufficient as others can be easily "guessed." Figure 6.1 shows highly trained GANs that convert a head CT image to its corresponding MRI equivalent.

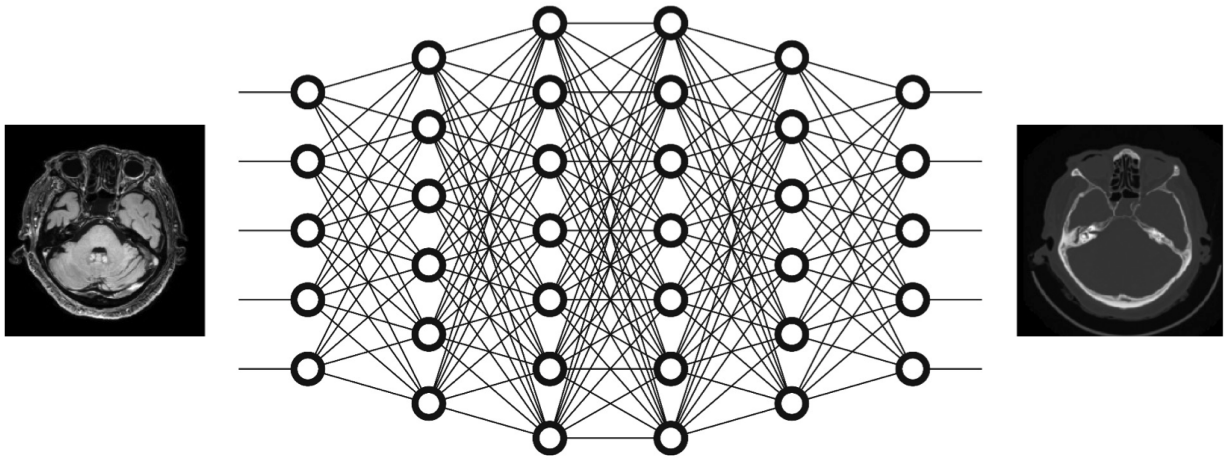

Figure 6.1: Model of generative adversarial networks that is highly trained in converting head CT image to its corresponding MRI equivalent.

BIBLIOGRAPHY

[1] G. Wang, J. Zhang, H. Gao, V. Weir, H. Yu, W. Cong, X. Xu, H. Shen, J. Bennett, M. Furth, Y. Wang, and M. Vannier, "Towards omni-tomography—grand fusion of multiple modalities for simultaneous interior tomography," *PLoS ONE*, vol. 7, 2012.

[2] G. Wang, M. Kalra, V. Murugan, Y. Xi, L. Gjesteby, M. Getzin, Q. Yang, W. Cong, and M. Vannier, "Simultaneous ct-mri - next chapter of multimodality imaging," *Medical Physics*, vol. 42, pp. 5879 – 5889, 2015.

[3] G. H. U. Kingdom, "Product: Pet/ct," 2013. [Online]. Available: http://www3.gehealthcare.co.uk

[4] S. Nagamachi, R. Nishii, H. Wakamatsu, Y. Mizutani, S. Kiyohara, S. Fujita, S. Futami, T. Sakae, E. Furukoji, S. Tamura, H. Arita, K. Chijiiwa, and K. Kawai, "The usefulness of 18f-fdg pet/mri fusion image in diagnosing pancreatic tumor: comparison with ^{18}f-fdg pet/ct," *Annals of Nuclear Medicine*, vol. 27, pp. 554–563, 2013.

[5] "Omni-tomography: An all-in-one modality?" 2013. [Online]. Available: http://www.diagnosticimaging.com/ct/omni-tomography-all-one-modality

[6] "Ultra-low dose ct kub," 2014. [Online]. Available: http://www.hawaiidrs.com/2014/01/16/ultra-low-dose-ct-kub/

[7] T. Koehler, B. Brendel, and K. M. Brown, "A new method for metal artifact reduction in ct," *2nd International Conference on Image Formation in X-Ray CT*, pp. 29–32, 2012.

[8] K. Grant and R. Raupach, "White paper: Safire: Sinogram affirmed iterative reconstruction," CT Unit, Siemens Healthcare, USA, Tech. Rep., 2012.

[9] "Arbeitsgruppe phantome," Institute of Medical Physics , Friedrich-Alexander-University Erlangen-Nrnberg, Germany. [Online]. Available: http://www.imp.uni-erlangen.de/phantoms/

[10] M. Lustig, D. Donoho, and J. M. Pauly, "Sparse mri: The applications of compressed sensing for rapid mr imaging," *Magnetic Resonance in Medicine*, vol. 58, pp. 1182–1195, 2008.

[11] B. D. Man and S. Basu, "Distance-driven projection and backprojection," *Physics in Medicine and Biology*, vol. 49, pp. 2463–2476, 2004.

[12] M. Beister, D. Kolditz, and W. A. Kalender, "Iterative reconstruction methods in x-ray ct," *Physica Medica*, vol. 28, pp. 94–108, 2012.

[13] "Radiation dose in x-ray and ct exams," 2018. [Online]. Available: https://www.radiologyinfo.org/en/pdf/safety-xray.pdf

[14] "How long does a mri scan take?" Advanced Imaging of Community Medical Center, Missoula, Montana, United States, 2016. [Online]. Available: http://www.advancedimagingofmt.com/index.php?page=mri-faq

[15] A. V. Oppenheim, A. S. Willsky, and S. Hamid, *Signals and Systems*. Pearson; 2 edition, 1996.

[16] J. Siewerdsen, "Multimodality imaging: Physics and technology considerations in diagnostic and image guided procedures," *Medical Physics*, vol. 35, p. 2862, 2008.

[17] M. Vannier, "Multi-modality imaging: Current state of the art," *Medical Physics*, vol. 37, p. 3371, 2010.

[18] L. Marti-Bonmati, R. Sopena, P. Bartumeus, and P. Sopena, "Multimodality imaging techniques," *Contrast Media Mol. Imaging*, vol. 5, pp. 180–189, 2010.

[19] R. K.Tekade and X. Sun, "The warburg effect and glucose-derived cancer theranostics," *Drug Discovery Today*, vol. 22, pp. 1637–1653, 2017.

[20] E. C. Ehman, G. B. Johnson, J. E. Villanueva-Meyer, S. Cha, A. P. Leynes, P. E. Z. Larson, and T. A. Hope, "Pet/mri: Where might it replace pet/ct?" *Journal of Magnetic Resonance Imaging*, vol. 46, pp. 1247–1262, 2017.

[21] R. Matthews and M. Choi, "Clinical utility of positron emission tomography magnetic resonance imaging (pet-mri) in gastrointestinal cancers," *Diagnostics*, vol. 6, p. 35, 2016.

[22] P. Mergo, T. Helmberger, P. Buetow, R. Helmberger, and P. Ros, "Pancreatic neoplasms: Mr imaging and pathologic correlation," *Radiographics*, vol. 17, pp. 281–301, 1997.

[23] H. Yu and G. Wang, "Compressed sensing based interior tomography," *Phys. Med. Biol.*, vol. 54, pp. 2791–2805, 2009.

[24] H. Yu, G. Wang, J. Hsieh, D. W. Entrikin, S. Ellis, B. Liu, and J. J. Carr, "Compressed sensing based interior tomography: Preliminary clinical application," *Journal of Computer Assisted Tomography*, vol. 35, pp. 762–764, 2011.

[25] A. C. Kak and M. Slaney, *Principles of Computerized Tomographic Imaging*. Society for Industrial and Applied Mathematics, 2001.

[26] D. G. Nishimura, *Principles of Magnetic Resonance Imaging*. Stanford University, 2010.

[27] M. Lustig, D. Donoho, and J. M. Pauly, "Sparse mri: The application of compressed sensing for rapid mr imaging," *Magnetic Resonance in Medicine*, vol. 58, pp. 1182–1195, 2007.

[28] M. Lustig, D. Donoho, J. Santos, and J. Pauly, "Compressed sensing mri," *Signal Processing Magazine, IEEE*, vol. 25, pp. 72–82, 2008.

[29] E. J. Candes, J. Romberg, and T. Tao, "Stable signal recovery from incomplete and inaccurate measurements," *Comm. Pure Appl. Math.*, vol. 59, pp. 1207–1223, 2005.

[30] ——, "Robust uncertainty principles: Exact signal reconstruction from highly incomplete frequency information," *IEEE Trans. on Information Theory*, vol. 52, pp. 1289–1306, 2006.

[31] D. Donoho, "Compressed sensing," *IEEE Transactions on Information Theory*, vol. 52, pp. 5406–5425, 2006.

[32] E. Haber and D. Oldenburg, "Joint inversion: a structural approach," *Inverse Problems*, vol. 13, pp. 63–77, 1997.

[33] D. S. Rigie and P. J. L. Rivire, "Joint reconstruction of multi-channel, spectral ct data via constrained total nuclear variation minimization," *Physics in Medicine and Biology*, vol. 60, pp. 1741–1762, 2015.

[34] M. J. Ehrhardt, K. Thielemans, L. Pizarro, D. Atkinson, S. Ourselin, B. F. Hutton, and S. R. Arridge1, "Positron emission tomography: Current challenges and opportunities for technological advances in clinical and preclinical imaging systems," *Inverse Problems*, vol. 13, pp. 15 001–15 023, 2015.

[35] J. J. Vaquero and P. Kinahan, "Joint reconstruction of pet-mri by exploiting structural similarit," *Annual Review of Biomedical Engineering*, vol. 17, pp. 385–414, 2015.

[36] X. Cui, H. Yu, G. Wang, and L. Mili, "Total variation minimization-based multimodality medical image reconstruction," *Proc. SPIE 9212, Developments in X-Ray Tomography IX*, vol. 9212, p. 11, 2014.

[37] Y. Xi, J. Zhao, J. R. Bennett, M. R. Stacy, A. J. Sinusas, and G. Wang, "Simultaneous ct-mri reconstruction for constrained imaging geometries using structural coupling and compressive sensing," *IEEE Transactions on Biomedical Engineering*, vol. 63, pp. 1301–1309, 2015.

[38] L. Gjesteby, Y. Xi, M. K. Kalra, Q. Yang, and G. Wang, "Hybrid imaging system for simultaneous spiral mr and x-ray (mrx) scans," *IEEE Access*, vol. 5, pp. 1050–1061, 2016.

[39] L. A. Gallardo and M. A. Meju, "Structure-coupled multiphysics imaging in geophysical sciences," *Reviews of Geophysics*, vol. 49, pp. 1–19, 2011.

[40] E. Haber and M. H. Gazit, "Model fusion and joint inversion," *Surveys in Geophysics*, vol. 34, pp. 675–695, 2013.

[41] A. Aghasi1, I. Mendoza-Sanchez3, E. L. Miller, C. A. Ramsburg, and L. M. Abriola, "A geometric approach to joint inversion with applications to contaminant source zone characterization," *Inverse problems*, vol. 29, p. 115014, 2013.

[42] J. Tang and A. Rahmim, "Bayesian pet image reconstruction incorporating anato-functional joint entropy," *Physics in Medicine and Biology*, vol. 23, p. 70637075, 2010.

[43] S. Somayajula, C. Panagiotou, A. Rangarajan, Q. Li, S. R. Arridge, and R. M. Leahy, "Pet image reconstruction using information theoretic anatomical priors," *IEEE TRANSACTIONS ON MEDICAL IMAGING*, vol. 30, pp. 537–549, 2010.

[44] Y. Xi, J. Zhao, J. R. Bennett, M. R. Stacy, A. J. Sinusas, and G. Wang, "Simultaneous ct-mri reconstruction for constrained imaging geometries using structural coupling and compressive sensing," *IEEE Transaction Biomedical Engineering*, vol. 63, p. 13011309, 2016.

[45] B. Wang and L. Li, "Recent development of dual-dictionary learning approach in medical image analysis and reconstruction," *Computational and Mathematical Methods in Medicine*, p. 9, 2015.

[46] L. Li, B. Wanga, and G. Wang, "Edge-oriented dual-dictionary guided enrichment (edge) for mri-ct image reconstruction," *Journal of X-ray Science and Technology*, vol. 24, p. 161175, 2016.

[47] X. Cui, L. Mili, and H. Yu, "Sparse-prior-based projection distance optimization method for joint ct-mri reconstruction," *IEEE Access*, vol. 5, pp. 20 099–20 110, 2017.

[48] X. Cui, L. Mili, G. Wang, and H. Yu, "Wavelet-based joint ct-mri reconstruction," *Journal of X-Ray Science and Technology*, vol. 26, pp. 379–393, 2018.

[49] Y. C. Eldar, A. O. H. III, L. Deng, J. Fessler, J. Kovacevic, H. V. Poor, and S. Young, "Schallenges and open problems in signal processing: Panel discussion summary from icassp 2017," *IEEE Signal Processing Magazine*, vol. 34, pp. 8–23, 2017.

[50] D. G. Nishimura, *Principles of Magnetic Resonance Imaging*. Stanford University, 2010.

[51] FDA, "Computed tomography (ct)," 2018. [Online]. Available: https://www.fda.gov/Radiation-EmittingProducts/RadiationEmittingProductsandProcedures/MedicalImaging/MedicalX-Rays/ucm115317.htm

[52] A. Beer, "Determination of the absorption of red light in colored liquids," *Annalen der Physik und Chemie*, vol. 86, pp. 78–88, 1852.

[53] J. Radon, "On the determination of functions from their integral values along certain manifolds," *IEEE Transactions on Medical Imaging*, vol. 5, pp. 170–176, 1986.

[54] J. Hadamard, "Sur les problmes aux drives partielles et leur signification physique," *Princeton University Bulletin*, pp. 49–52, 1902.

[55] ——, "Lectures on cauchy's problem in linear partial differential equations," *Yale Univ. Press*, 1923.

[56] C. Pucci, "Sui problemi di cauchy non "ben posti"," *Atti Acc. Naz. Lincei Rend. Cl. Sci. Fis. Mat. Natur*, vol. 18, pp. 473–477, 1955.

[57] F. John, "Continuous dependence on data for solutions of partial differential equations with a prescribed bound," *Comm. Pure Appl. Math*, vol. 13, pp. 551–585, 1960.

[58] N. Dunford and J. Schwartz, *Linear operators, Parts I and II*. Wiley-Interscience, 1958.

[59] P. Halmos, *A Hilbert Space Problem Book*. Springer-Verlag, 1982.

[60] A. N. Tikhonov and V. Y. Arsenin, *Solution of Ill-posed Problems*. Winston and Sons, 1977.

[61] A. Tikhonov, A. Goncharsky, V. Stepanov, and A. Yagola, *Numerical Methods for the Solution of Ill-Posed Problems*. Springer Netherlands, 1995.

[62] D. A. B. Miller, *Quantum Mechanics for Scientists and Engineers*. Cambridge University Press, 2008.

[63] G. H. Hardy, J. E. Littlewood, and G. Plya, *Inequalities*. Cambridge University Press, 1952.

[64] X. Cui, "An investigation of raw data corrections for radial fat-water magnetic resonance imaging," Master's thesis, Vanderbilt University, Nashville, Tennessee, United States, 2011.

[65] R. A. Brooks and G. D. Chiro, "Principles of computer assisted tomography (cat) in radiographic and radioisotopic imaging," *Physics in Medicine and Biology*, vol. 21, pp. 689–732, 1976.

[66] F. Natterer, *The mathematics of computerized tomography*. Stuttgart: B.G. Teubner, 1986.

[67] G. T. Herman, *Fundamentals of computerized tomography : image reconstruction from projections (2nd ed.)*. Springer, 2009.

[68] Y. Censor and S. Zenios, *Parallel optimization: theory, algorithms, and applications*. Oxford University Press, 1997.

[69] C. R. Grimmett and D. R. Stirzaker, *Probability and Random Processes*. Oxford University Press, 2001.

[70] J. Fessler, "Penalized weighted least-squares image reconstruction for positron emission tomography," *IEEE Transactions on Medical Imaging*, vol. 13, pp. 290–300, 1994.

[71] N. C, B. P, and L. J, "Iterative reconstruction in cardiac ct," *J Cardiovasc Comput Tomogr*, vol. 9, pp. 255–263, 2015.

[72] M. M. M.Sc., P. M. M.Sc., A. Krauss, O. Kölbl, and B. Dobler, "Iterative metal artifact reduction improves dose calculation accuracy," *Strahlentherapie und Onkologie*, vol. 192, pp. 403–413, 2016.

[73] S. Singh, M. K. Kalra, M. D. Gilman, J. Hsieh, H. H. Pien, S. R. Digumarthy, and J.-A. O. Shepard, "Adaptive statistical iterative reconstruction technique for radiation dose reduction in chest ct: a pilot study," *Radiology*, vol. 259, pp. 565–573, 2011.

[74] "Health effects of ionising radiation," *Annals of the ICRP*, vol. 24, pp. 7–10, 1994.

[75] U. S. N. R. Commission, "Backgrounder on biological effects of radiation," 2017. [Online]. Available: https://www.nrc.gov/reading-rm/doc-collections/fact-sheets/bio-effects-radiation.html

[76] "What are the radiation risks from ct?" 2017. [Online]. Available: https://www.fda.gov/radiation-emittingproducts/radiationemittingproductsandprocedures/medicalimaging/medicalx-rays/ucm115329.htm

[77] M. J. Muckley, "Acceleration methods for mri," PhD dissertation, the University of Michigan, 2016.

[78] C. E. Shannon, "Communication in the presence of noise," in *Proceedings of the Institute of Radio Engineers*, ser. 37, vol. 1, 1949, pp. 10–21.

[79] S. Foucart and H. Rauhut, *A Mathematical Introduction to Compressive Sensing*. Springer, 2013.

[80] S. Mallat, *A Wavelet Tour of Signal Processing: The Sparse Way*. Academic Press; 3rd edition, 2008.

[81] A. Ben-Israel and T. N. Greville, *Generalized Inverses: Theory and Applications*. Springer, 2003.

[82] C. Ramirez, V. Kreinovich, and M. Argaez, "Why L_1 is a good approximation to L_0: A geometric explanation," *Journal of Uncertain Systems*, vol. 7, pp. 203–207, 2013.

[83] B. K. Natarajan, "Sparse approximate solutions to linear systems," *SIAM Journal on Computing*, vol. 24, pp. 227–234, 1995.

[84] D. Donoho, "Thresholds for the recovery of sparse solutions via l1 minimization," *IEEE. Info. Sci. and Sys., 40th Annu. Conf.*, pp. 202–206, 2006.

[85] J. S. Jrgensen and E. Y. Sidky, "How little data is enough? phase-diagram analysis of sparsity-regularized x-ray computed tomography," *Philos Trans A Math Phys Eng Sci.*, vol. 373, pp. 1–25, 2015.

[86] S. Boyd and L. Vandenberghe, *Convex Optimization*. Cambridge University Press, 2004.

[87] P. Wolfe, "Convergence conditions for ascent methods," *SIAM Review*, vol. 11, pp. 226–235, 1969.

[88] ——, "Convergence conditions for ascent methods," *SIAM Review*, vol. 13, pp. 185–188, 1969.

[89] B. D. Man1 and J. A. Fessler, *Statistical Iterative Reconstruction for X-Ray Computed Tomography*. Medical Physics, 2009.

[90] B. D. Man and S. Basu, "Distance-driven projection and backprojection," *Nuclear Science Symposium Conference Record, 2002 IEEE*, vol. 3, pp. 1477–1480, 2002.

[91] W. Zhou, A. C. Bovik, H. R. Sheikh, and E. P. Simoncelli, "Image quality assessment: From error visibility to structural similarity," *IEEE Transactions on Image Processing*, vol. 13, pp. 600–612, 2004.

[92] X. Bresson and T. F. Chan, "Fast dual minimization of the vectoral total variation norm and applications to color imaging processing," *Inverse Problem and Imaging*, vol. 2, pp. 455–484, 2008.

[93] W. H. Press, S. A. Teukolsky, W. T. Vetterling, and B. P. Flannery, *Numerical Recipes in C - The Art of Scientific Computing*, 2nd ed. Cambridge University Press, 1992.

[94] J. Nocedal and S. J. Wright, *Numerical Optimization*. Springer-Verlag, 2000.

[95] M. R. Hestenes and E. Stiefel, "Methods of conjugate gradients for solving linear systems," *J. Research Nat. Bur. Standards*, vol. 49, pp. 409–436, 1953.

[96] Y. H. Dai and Y. Yuan, ""a nonlinear conjugate gradient method with a strong global convergence property," *SIAM J. Optim*, vol. 10, pp. 149–254, 1999.

[97] R. Fletcher and C. M. Reeves, "Function minimization by conjugate gradients," *Comput. J*, vol. 7, pp. 149–254, 1964.

[98] G. Herman and R. Davidi, "Image reconstruction from a small number of projections," *Inverse Problems*, vol. 24, pp. 45 011–45 028, 2008.

[99] A. Pizurica, A. M. Wink, E. Vansteenkiste, W. Philips, and B. T. Roerdink, "A review of wavelet denoising in mri and ultrasound brain imaging," *Current Medical Imaging Reviews*, vol. 2, pp. 1–14, 2006.

[100] "Displaying images," Department of Radiology, Upstate Medical University, Syracuse, New York 13210. [Online]. Available: http://www.upstate.edu/radiology/education/rsna/intro/display.php

[101] J. Stein, *Digital Signal Processing: A Computer Science Perspective*. John Wiley and Sons, Inc, 2001.

[102] R. C. Gonzalez and R. E. Woods, *Digital Image Processing*. Pearson; 3rd edition, 2007.

[103] P. Bhosale, "Comparing cnr, snr, and image quality of ct images reconstructed with soft kernel, standard kernel, and standard kernel plus asir 30techniques," *International Journal of Radiology*, vol. 2, 2015.

[104] W.-J. Moon, "Measurement of signal-to-noise ratio in mr imaging with sensitivity encoding," *Radiology*, vol. 243, pp. 908–909, 2007.

[105] O. Dietrich, J. Raya, S. Reeder, M. Reiser, and S. Schoenberg, "Measurement of signal-to-noise ratios in mr images: influence of multichannel coils, parallel imaging, and reconstruction filters," *Journal of Magnetic Resonance Imaging*, vol. 26, pp. 375–385, 2007.

[106] I. J. Goodfellow, J. Pouget-Abadie, M. Mirza, B. Xu, D. Warde-Farley, S. Ozair, A. Courville, and Y. Bengio, "Generative adversarial networks," in *NIPS'14 Proceedings of the 27th International Conference on Neural Information Processing Systems*, vol. 2. Montreal, Canada: MIT Press Cambridge, MA, USA, 2014, pp. 2672–2680.

[107] T. Saliman, I. Goodfellow, W. Zaremba, V. Cheung, A. Radford, and X. Chen, "Improved techniques for training gans," in *NIPS'16 Proceedings of the 30th International Conference on Neural Information Processing Systems*. Barcelona, Spain: Curran Associates Inc., USA, 2016, pp. 2234–2242.

[108] A. Laghi, L. L. Geyer, U. J. Schoepf, F. G. Meinel, J. Nance, John W., C. N. De Cecco, G. Bastarrika, J. A. Leipsic, N. S. Paul, M. Rengo, and A. Laghi, "State of the art: Iterative ct reconstruction techniques," *Radiology*, vol. 276, pp. 338–356, 2015.

[109] M. Uecker, S. Zhang, D. Voit, A. Karaus, K. D. Merboldt, and J. Frahm, "Real-time mri at a resolution of 20 ms," *NMR Biomed.*, vol. 23, pp. 986–994, 2010.

[110] S. Schaetz, D. Voit, J. Frahm, and M. Uecker, "Accelerated computing in magnetic resonance imaging: Real-time imaging using nonlinear inverse reconstruction," *Computational and Mathematical Methods in Medicine*, pp. 1–11, 2017.

[111] P. Joseph, "An improved algorithm for reprojecting rays through pixel images," *IEEE Transactions on Medical Imaging*, p. 192196, 1983.

[112] B. Fornberg, "Generation of finite difference formulas on arbitrarily spaced grids," *Mathematics of Computation*, vol. 51, no. 184, pp. 699–706, 1988.

[113] T. Farncombe and K. Iniewski, *Medical Imaging: Technology and Applications (Devices, Circuits, and Systems)*. CRC Press; 1st edition, 2013.

[114] M. A. Bernstein, K. F. King, and X. J. Zhou, *Handbook of MRI Pulse Sequences*. Academic Press; 1 edition, 2004.

[115] G. H. Chen, J. Tang, and S. Leng, "Prior image constrained compressed sensing (piccs): a method to accurately reconstruct dynamic ct images from highly undersampled projection data sets," *Medical Physics*, vol. 35, pp. 660–663, 2008.

[116] C.-W. Chang and M.-A. Mycek, "Total variation versus wavelet-based methods for image denoising in fluorescence lifetime imaging microscopy," *Journal of Biophotonics*, vol. 5, pp. 449–457, 2012.

[117] E. Y. Sidky and X. C. Pan, "Image reconstruction in circular conebeam computed tomography by constrained, total variation minimization," *Physics in Medicine and Biology*, vol. 53, pp. 4777–4807, 2008.

[118] S. R. Deans, *The Radon Transform and Some of Its Applications.* New York: John Wiley and Sons., 1983.

[119] Bertero, *Inverse Problems in Scattering and Imaging.* CRC Press; 1st edition, 1992.

[120] I. Loris, G. Nolet, I. Daubechies1, and F. A. Dahlen, "Tomographic inversion using l1-norm regularization of wavelet coefficients," *Geophysical Journal International*, vol. 170, pp. 359–370, 2007.

[121] H. Kudo, T. Suzuki, and E. A. Rashed, "Image reconstruction for sparse-view ct and interior ct-introduction to compressed sensing and differentiated backprojection," *Quant Imaging Med. Surg.*, vol. 3, pp. 147–161, 2013.

[122] D. B. Twieg, "The k-trajectory formulation of the nmr imaging process with applications in analysis and synthesis of imaging methods," *Medical Physics*, vol. 10, pp. 610–621, 1983.

[123] J. A. Fessler, "On nufft-based gridding for non-cartesian mri," *J Magn Reson.*, vol. 2, pp. 191–195, 2007.

[124] S. Geethanath, R. Reddy, A. Konar, S. Imam, R. Sundaresan, R. R. D, and R. Venkatesan, "Compressed sensing mri: a review," *Crit Rev Biomed Eng.*, vol. 41, pp. 183–204, 2013.

[125] L. Shepp and B. F. Logan, "The fourier reconstruction of a head section," *IEEE Transactions on Nuclear Science*, vol. 21, pp. 21–43, 1974.

[126] A. K. Jain, *Fundamentals of Digital Image Processing*. Prentice Hall, 1989.

[127] L. G. Zeng, *Medical Image Reconstruction: A Conceptual Tutorial*. Springer, 2010.

[128] J. Song, Q. H. Liu, G. A. Johnson, and C. T. Badea, "Sparseness prior based iterative image reconstruction for retrospectively gated cardiac micro-ct," *Med Phys.*, vol. 34, pp. 4476–4483, 2007.

[129] J. Huang, Y. Zhang, J. Ma, D. Zeng, Z. Bian, S. Niu, Q. Feng, Z. Liang, and W. Chen, "Iterative image reconstruction for sparse-view ct using normal-dose image induced total variation prior," *PLoS ONE*, vol. 8, 2013.

[130] E. Polak and G. Ribiere, "Note sur la convergence de directions conjugue," *Rev. Francaise Informat Recherche Operationelle*, vol. 16, pp. 35–43, 1969.

[131] E. Polak, "The conjugate gradient method in extreme problems," *USSR Comp. Math. Math. Phys.*, vol. 9, pp. 94–112, 1969.